

THE RAREFIED GAS ELECTRO JET (RGEJ) MICRO-THRUSTER FOR  
PROPULSION OF SMALL SATELLITES

By

ARIEL BLANCO

A DISSERTATION PRESENTED TO THE GRADUATE SCHOOL  
OF THE UNIVERSITY OF FLORIDA IN PARTIAL FULFILLMENT  
OF THE REQUIREMENTS FOR THE DEGREE OF  
DOCTOR OF PHILOSOPHY

UNIVERSITY OF FLORIDA

2017

© 2017 Ariel Blanco

To my family, friends, and mentors

## ACKNOWLEDGMENTS

I thank my parents and maternal grandmother for their continuous support and encouragement, for teaching me to persevere and value the pursuit of knowledge. I am extremely thankful to my friends and lab colleagues who have helped me so much, not only academically but also by giving me moral support and solidarity. Finally, yet importantly, it is a genuine pleasure to express my deep sense of thanks and gratitude to all my mentors, especially my advisor, Dr. Subrata Roy. Without his guidance, mentoring, and support, this study would not have been completed.

# TABLE OF CONTENTS

	<u>page</u>
ACKNOWLEDGMENTS.....	4
LIST OF TABLES.....	8
LIST OF FIGURES.....	10
ABSTRACT.....	12
CHAPTER	
1 INTRODUCTION .....	14
The Rarefied Gas Electro Jet (RGEJ) Design and Motivation .....	18
Performance Parameters.....	25
2 MICROPROPULSION TECHNOLOGIES.....	29
Introduction to Micro-propulsion Devices.....	29
Chemical Propulsion Devices for Small Satellites.....	29
Cold Gas Thrusters .....	30
Mono Propellant Thrusters .....	31
Bipropellant Thrusters .....	33
Electric Propulsion Devices for Small Satellites.....	34
Electrothermal Thrusters .....	34
Free molecule micro-resistojet (FMMR).....	35
Low-power DC arcjets.....	37
Microcavity discharge thrusters.....	38
Micro-plasma thruster (MPT) .....	39
Electrostatic Thrusters.....	40
Miniature ion engines.....	41
Miniature hall thrusters.....	43
Colloidal and field emission electric propulsion (FEEP) thrusters .....	46
Electromagnetic Thrusters.....	49
Conclusion of Micro-propulsion Technologies Survey .....	50
3 GAS DISCHARGE PHYSICS .....	52
Electrical Breakdown of Gases .....	53
Dark Discharge.....	54
Glow Discharge .....	56
Arc Discharge.....	57
Qualitative Characteristics of DC Glow Discharge.....	57
Paschen's law .....	62

	Sputtering .....	64
4	GOVERNING EQUATIONS .....	66
	Hydrodynamic Plasma Model .....	66
	Boltzmann Equation .....	66
	Distribution Function Moments Equation .....	68
	Continuity Equation .....	70
	Momentum Equation .....	72
	Energy Equation .....	74
	Drift-Diffusion Approximation .....	76
	Maxwell's Equations .....	81
	Transport Properties .....	84
	Boundary Conditions .....	87
	Open surface boundary .....	88
	Anode boundary .....	89
	Cathode boundary .....	90
	Dielectric wall .....	90
	Plasma Electrostatic Force and Electrothermal Heating Source .....	91
	Rarefied Gas Equations .....	92
	Heat Transfer Governing Equations .....	97
	Thermal Radiation Heat Transfer .....	97
	View Factor Formulas .....	98
	Conduction Heat Transfer .....	100
	Conduction Heat Transfer Boundary Conditions .....	101
5	NUMERICAL MODEL .....	102
	The Ionized Gas Module .....	103
	The Rarefied Gas Module .....	107
	Galerkin Weak Statement .....	108
	Finite Element Basis Function .....	110
	Bilinear Basis .....	112
	Newton-Raphson Scheme .....	115
	Decoupled Heat Transfer Codes .....	117
	Conduction Numerical Code .....	117
	Thermal Radiation Heat Transfer Numerical Code .....	117
6	BENCHMARKING AND VALIDATION .....	119
	Ionized Gas Module (IGM) .....	119
	Verification and Grid Convergence Study of the IGM .....	119
	Validation of the IGM .....	122
	Rarefied Gas Module (RGM) .....	125
	Verification of the RGM using plane Poiseuille flow .....	125
	Benchmarking/Validation of the RGM .....	129

7	CASES STUDIED .....	132
	Geometry and Grid .....	132
	Cold gas thruster and constant thermal heating source thrusters' results and comparison .....	134
	RGEJ thruster performance .....	145
	RGEJ thruster discharge characteristics .....	156
	Thermal analysis .....	159
8	SUMMARY .....	162
	Summary of the Results .....	162
	The Numerical Model .....	165
	Future Directions to Continue Improving RGEJ .....	166
	LIST OF REFERENCES .....	167
	BIOGRAPHICAL SKETCH .....	176

## LIST OF TABLES

<u>Table</u>	<u>page</u>
1-1 Mass classification of Satellites. ....	17
2-1 Cold gas propellant performance.....	31
2-2 Micro-ion engine performance.....	43
2-3 Small and micro-Hall thruster performances.....	46
2-4 ST-7 colloid thruster cluster performance characteristics. ....	47
2-5 FEEP Performance Characteristics. ....	48
2-6 Micro-PPT Performances. ....	50
3-1 Breakdown voltage constants A and B. ....	63
3-2 Limit of $(pd)$ and minimum breakdown voltage values for argon.....	63
4-1 Relevant Reactions. ....	86
6-1 Coefficients for the grid refinement study. ....	121
6-2 Comparison between experiment and numerical model with $(\gamma_{sec}=0.01)$ for $(300\text{ V} < V_{Pk-Pk} < 800\text{ V})$ .....	124
6-3 Microchannel Properties of Fluid for Subsonic Gas Flows. ....	130
6-4 Grid dependence test of the centerline u-velocity (m/s) at different x-locations. ....	130
6-5 Grid dependence test done using MIG of the centerline u-velocity (m/s) at different x-locations. ....	130
6-6 Comparison of centerline pressure ratios at different x-locations. ....	131
7-1 Values of total thermal heating source $(\dot{Q})$ , mass flow rate $(\dot{m})$ , thrust $(F_{Thrust})$ , shear force $(F_{\tau_{Wall}})$ , specific impulse $(I_{sp})$ , specific impulse increase $(I_{sp}\text{ Inc.})$ compared to the <i>base case</i> , exit plane Mach number $(M_{Exit})$ at the centerline, and exit Knudsen number $(Kn_{Exit})$ at the centerline are displayed...	136
7-2 Values of: voltage (V), mass flow rate $(\dot{m})$ , thrust $(F_{Thrust})$ , shear force $(F_{\tau_{Wall}})$ , specific impulse $(I_{sp})$ , specific impulse percent increase $(I_{sp}\text{ Inc.})$ , current $(I)$ ,	

total thermal heating source ( $\dot{Q}$ ), total electrical power ( $P_W$ ), and fraction of the total electrical power converted into thermal heating source ( $\dot{Q}/P_W$ ). ..... 145

## LIST OF FIGURES

<u>Figure</u>	<u>page</u>
2-1 Cold gas thruster from Moog, model 58x125A.....	30
2-2 JPL Hydrazine milli-Newton Thrusters (HmNT), a monopropellant technology ...	32
2-3 MIT micro-bipropellant engine concept.....	34
2-4 FMMR thruster design.....	35
2-5 FMMR thruster.....	37
2-6 VAT thruster .....	38
2-7 Electro-thermal thrusters .....	39
2-8 Schematic of the micro-plasma thruster (MPT) .....	40
2-9 Ion thrusters.....	42
2-10 Hall thrusters .....	45
2-11 Colloid thruster .....	47
2-12 FEED-5 thruster by Centrosazio/Alta.....	48
2-13 PPT thruster .....	49
3-1 Voltage-Current Characteristics of a DC gas discharge.....	54
3-2 Qualitative characteristics of DC glow discharge and electric potential distribution at low pressures (0.1 – 10 Torr) and room temperature .....	58
3-3 Paschen curves for argon at different values of $\gamma_{sec}$ .....	64
4-1 Gas flow regimes depending on Kn.....	94
4-2 View Factors.....	98
5-1 Schematic of the new MIG code with rarefied gas and ionized gas modules ...	103
5-2 Generic rectangular parallelepiped element $\Omega_{ej}$ .....	112
6-1 Order of accuracy for Scharfetter-Gummel flux discretization scheme for Case 1 and Case 2.....	121
6-2 Comparison between numerical model and experiment.....	124

6-3	Plane Poiseuille flow in a (L=10, H=1) channel with a (Re = 100) using a (21x11) nodes mesh.....	128
7-1	Geometry and design of the RGEJ thruster using several stack slots similarly to the FMMR thruster.....	132
7-2	Domain region of the RGEJ numerically simulated .....	133
7-3	Regions of applied $q'''$ .....	134
7-4	Graphical representation of different parameters .....	137
7-5	Comparisons between “ <i>base case and case Q2-600</i> ”, and “ <i>base case and case Q4-600</i> ”.....	140
7-6	Comparison of <i>base case</i> , <i>case Q2-600</i> , and <i>case Q4-600</i> .....	141
7-7	Parameters of the RGEJ thruster for the given voltage regime .....	146
7-8	Left plots show a comparison of the rarefied gas results between the <i>base case</i> (on the bottom half) and <i>case 750V</i> (on the top half) .....	147
7-9	Shear stress at the wall for all cases in Table 7-2. ....	150
7-10	Comparison of plasma discharge results for <i>case 450V</i> and <i>case 750V</i> (on the left), and comparison of plasma-discharge centerline results for all cases (on the right) .....	151
7-11	Comparison of plasma discharge results for <i>case 450V</i> and <i>case 750V</i> (on the left), and comparison of plasma-discharge centerline results for all cases (on the right) .....	152
7-12	<i>Case 750V</i> .....	155
7-13	Parameters of the RGEJ thruster for the given voltage regime .....	157
7-14	Conduction heat loss analysis for <i>Case 750V</i> assuming 1 cm of width, with the temperature distribution given along the wall as $T=f(x)$ . ....	159
7-15	Radiation heat loss analysis for <i>Case 750V</i> assuming 1 cm of width, with the temperature distribution of given along the wall as $T=f(x)$ . ....	160

Abstract of Dissertation Presented to the Graduate School  
of the University of Florida in Partial Fulfillment of the  
Requirements for the Degree of Doctor of Philosophy

THE RAREFIED GAS ELECTRO JET (RGEJ) MICRO-THRUSTER FOR  
PROPULSION OF SMALL SATELLITES

By

Ariel Blanco

December 2017

Chair: Subrata Roy  
Major: Aerospace Engineering

Small satellites have multiple applications such as commercial, military, and space science missions. Further development of micro-propulsion concepts is needed. In this dissertation, a micro-thrusters for small satellites called the rarefied gas electro jet (RGEJ) is investigated numerically. The RGEJ design aims to increase the efficiency of the energy exchange from the electrical source to the propellant, avoiding the high thermal dissipation problem associated with other technologies.

In order to simulate the RGEJ, an existing and previously described in literature, in-house modular Multi-scale Ionized Gas (MIG) flow solver platform is used. The rarefied gas is modeled using density-based compressible flow equations with rarefied boundary conditions and the ionized gas is modeled using local mean energy approximation (LMEA).

Benchmarking and validation of the rarefied gas and ionized gas modules are performed, respectively. Several thruster cases are studied with different discharge voltages to investigate the discharge characteristics and the thruster's performance

parameters such as mass flow rate, thrust, power consumption, and specific impulse. Finally, a thermal analysis is performed to investigate the thermal losses.

For the highest voltage tested (750 V), operating with argon propellant at plenum pressures of 1 Torr, the RGEJ thruster requires a total electrical power of 406 mW to heat the flow. Under these operation conditions, the RGEJ produces a thrust of 1.843 mN and a specific impulse ( $I_{sp}$ ) of 60.7 s with a thrust effectiveness of 1240 ( $\mu\text{N/W}$ ). This  $I_{sp}$  is a 37.6% improvement over the  $I_{sp}$  of a cold gas thruster operating with the same geometry, propellant, and plenum pressure. The heat loss due to conduction and radiation is expected to be less than 7.5% of the total electrical power. The  $I_{sp}$  of the RGEJ thruster was found to be 35% higher than the competing technology called the free molecule micro-resistojet (FMMR). Base on the thermal analysis, the RGEJ is predicted to have significantly fewer heat losses than FMMR.

To the author's knowledge, a numerical simulation of a thruster design using plasma-aided technology to replace the energy transfer mechanism of the FMMR thruster and decrease its inherent heat losses has never been attempted before.

## CHAPTER 1 INTRODUCTION

An artificial, or man-made, satellite is a machine that orbits the Earth or another body in space. Their purpose varies greatly; some take pictures and map terrestrial data to help scientist accurately predict the weather patterns tracking hurricanes, deforestation, global warming, etc., while others look outward and take pictures and collect data from extraterrestrial objects like stars, black holes, dark matter, and search for planets in faraway galaxies for a better understanding of our universe. Other satellites focus primarily on communications and the Global Positioning System (GPS), which is composed of a group of more than 20 satellites that allow the determination of the exact location of a GPS receiver. Satellites orbit the Earth at different heights, speeds, and paths.

Orbits can be categorized in terms of their centric, altitude, inclination, eccentricity, and synchronicity classifications. A geocentric orbit is an orbit around Earth. Low Earth Orbits (LEO's), Medium Earth Orbits (MEO's), and High Earth Orbits (HEO's) are geocentric orbits with an altitude range of 160 to 2000 km, 2000 to 35786 km, and >35786 km, respectively. The eccentricity of an orbit determines whether it is a closed (periodic) orbit or an open (escape) orbit. Circular orbits, with an eccentricity of zero, and elliptical orbits, with an eccentricity greater than zero and less than one, are closed orbits. Parabolic and hyperbolic orbits are open, while radial orbits can be either. A synchronous orbit has a period that is a rational multiple of the average rotational period of the body being orbited and this orbit is in the same direction as the rotation of the body being orbited. An example of a synchronous orbit is a Geosynchronous Orbit (GEO) with 1:1 ratio of the satellite period to the average rotational period of the body

being orbited. A circular Geosynchronous Orbit (GEO) is a geocentric orbit with an altitude of 35786 km and its period equals one sidereal day (23 hours, 56 minutes, 4.091 seconds). The orbital velocity necessary to achieve GEO is approximately 3070 m/s. If a GEO has an inclination of zero degrees with respect to the equatorial plane, then it is a geostationary orbit.

The two most common types of orbits are geostationary and polar. These denominations refer to the inclination of an orbit with respect to the equatorial plane. In a geostationary orbit, a satellite travels from west to east over the equator in the same direction and rate as the Earth's spin and it stays above the same location. In a polar orbit, the satellite travels in a north-south direction from pole to pole and it can scan the entire globe one strip at a time as the Earth spins. Once artificial satellites are launched and placed in their desired nominal orbit, they require some form of attitude control and orbit station-keeping to change or adjust their orientation and to compensate for the effects of drag from the thin atmosphere.

A thruster can adjust the orientation of a satellite or compensate for the drag effects by generating an acceleration in the desired direction. This acceleration is generated by expelling the propellant mass at a high velocity, imparting momentum to the spacecraft.

Several choices of propellant/energy source (such as chemical, electric, and nuclear) are available for powering propulsion devices. These categories can be further subdivided. For example, chemical propulsion includes cold gas, monopropellant, and bipropellant thrusters. Cold gas thrusters produce thrust using an inert gas and their thermal source is the thermal energy stored in the heat capacity of the gas.

Monopropellant and bipropellant thrusters depend on a chemical reaction. For monopropellant thrusters, the energy needed to propel the satellite is stored within the chemical bonds of the propellant molecules and a catalytic reaction is used to release the energy. Bipropellant engines use two types of propellants: a fuel and an oxidizer. Electric propulsion can be subdivided into three categories: electrothermal thrusters (e.g. resistojets) that heat the propellant using electrical energy, electrostatic thrusters (e.g. Ion and Hall thrusters) that accelerate the propellant using the Coulomb force, and electromagnetic thrusters (e.g. Pulse Plasma and Magnetoplasmadynamic thrusters) that accelerate the propellant using the Lorentz force. Nuclear powered devices use nuclear energy to generate electricity and thermal energy using a reactor, or kinetic energy by means of a nuclear pulse. However, nuclear-powered devices are avoided for LEO missions and may be suitable for future interstellar missions.

Most satellites have chemical thrusters (usually hydrazine) for station-keeping [1]. Some have used electric propulsion for north-south station-keeping and orbit raising, while interplanetary missions typically use chemical thrusters with the exception of a few missions where electric propulsion (primarily ion and hall effect thrusters) has been used with great success [2]. The purpose of a propulsion system is to change the momentum of a spacecraft; the amount of change in momentum is called the impulse. The velocity change caused by an impulse to the vehicle is termed the Delta-V ( $\Delta-V$ ). The amount of impulse that can be obtained from a fixed amount of reaction mass (propellant mass) is determined by the specific impulse ( $I_{sp}$ ). The  $I_{sp}$  is a key design parameter in space propulsion. It is defined as the change in momentum per unit of propellant weight spent. The higher the  $I_{sp}$ , the lesser the mass of the propellant

required to achieve a certain velocity increment. The  $I_{sp}$  is the metric of comparison between different propulsion technologies and depends strongly on the exit velocity of the propellant for each different propulsion device.

The cost of a satellite is proportional to its mass as shown in the following table by Barnhart et al. [3].

Table 1-1. Mass classification of Satellites [3].

<b>Satellite Category</b>	<b>Wet Mass (Fully-Fuel) (kg)</b>	<b>Cost (USD)</b>
Large	>1000	0.1 - 2 B
Medium	500-1000	50 - 100 M
Mini	100-500	10 - 50 M
Micro	10-100	2 - 10 M
Nano	1-10	0.2 - 2 M
Pico	0.1-1	20 - 200 K
Femto	<0.1	0.1 - 20 K

Cost and weight reductions can be achieved by partitioning the function of a single large satellite into a cluster of small ones, each with a mass less than 100 kg; this concept is called formation flying. Formation flying can be used for multiple application such as to make 3-D views of hurricanes by having multiple satellites orbiting on the same path, separated by a specific time interval with different viewing angles [4]. Small satellites have several advantages such as substantial reduction in the overall life cycle cost by making satellites less costly to construct and reduced launch costs.

Furthermore, the utilization of many smaller satellites to construct a constellation allows for a graceful degradation of the system capability as individual satellites are lost.

In recent years, major satellite manufacturers have presented development programs for small multi-mission satellites designed to operate on a Low Earth orbit to reduce the mission cost [5]. The size and power consumption of optical and radar instruments scale with orbital altitude for a given instrument performance [5]. Therefore, a low operational altitude using small and cheap commercial satellites greatly reduces the mission cost.

Unless a suitable station-keeping program is adopted, the large atmospheric drag forces present at LEO's altitudes can result in a severe perturbation of the orbital geometry and rapid decay of the orbit [5]. For example, the 6 kg Dove-1 spacecraft was released in a 250 km orbit and reentered the atmosphere after 6 days [6].

A practical micro-propulsion system is the main element for the development of a successful small spacecraft, which must perform a variety of mission options such as attitude control, station maintenance, altitude raising, plane changes, and deorbiting [4]. Since the field of micro-propulsion is still in its infancy, further development of micro-propulsion concepts is needed.

### **The Rarefied Gas Electro Jet (RGEJ) Design and Motivation**

As explained by Micci et al. [4], the following issues are of great importance for micro-propulsion systems: material compatibility between the propellant and the surface, contamination problems from propellant ablation and vaporization, valve leakage, passage clogging that could result in a single-point failure, system reliability and durability issues, manufacturing complexity, and integration complexity. Thrusters for small satellites must produce minimum impulse bits,  $\mathcal{O}(\mu\text{N}\cdot\text{s})$ , determined by attitude control requirements [4]. An impulse bit is the single-firing impulse imparted to a satellite

by a thruster and reflects the level of precision of the propulsion system. Small impulse bits produce larger time intervals between thruster firings, which reduce propellant consumption and allow for longer-duration quiescent spacecraft operation, enabling unperturbed scientific measurements [4]. In contrast, the thrust requirements for slew maneuvers extend into the  $\mathcal{O}(\text{mN})$  range, very large when compared to the impulse bits requirements for attitude control [4]. Propulsion systems for small satellites must overcome these issues while being lightweight, compact, low power, efficient, and inexpensive.

Cold gas thrusters have some desirable advantages, such as low complexity, small impulse bit ( $\sim 0.1 \text{ mN}\cdot\text{s}$ ) and no spacecraft contamination problems when a benign propellant is used (e.g.,  $\text{N}_2$ ) [4]. However, valve leakage for light propellants and low specific impulse for heavier propellants limit cold gas thruster's application as primary propulsion systems unless the  $(\Delta-V)$  requirements are less than  $\sim 100 \text{ m/s}$  [4]. Leakage in cold gas thrusters is the result of contaminants on the thruster valve seat, low propellant viscosity, and high-pressure propellant storage [4]. The  $I_{\text{sp}}$  of these thrusters is typically low unless very light gases are used such as hydrogen or helium, which produce experimentally measurable specific impulses of 272 and 165 s, respectively [4]. Hydrogen and helium are commonly avoided due to storage problems. Nitrogen is the most frequently used cold gas thruster propellant with an  $I_{\text{sp}}$  of 73 s due to reasonable storage density, performance, and lack of contamination concerns; while argon produces an  $I_{\text{sp}}$  of 52 s [4].

In order to increase the performance of cold gas thrusters, while keeping their advantageous characteristics, other designs such as the free molecule micro-resistojet

(FMMR) have been proposed [4]. FMMR consists of a thin-film heating element at constant temperature and a long ( $\sim 1$  cm), narrow ( $1-100 \mu\text{m}$ ) slot instead of a small nozzle to avoid catastrophically plugging the throat with contaminants [4]. FMMR operates with low stagnation pressures (50 to 500 Pa) and low exit Knudsen number ( $Kn \sim 1$ ) [4]. Due to the low pressures operating conditions of the FMMR, direct interaction with the heating element heats the propellant molecules increasing their kinetic energy before exiting the expansion slots. Gas heating occurs primarily by conduction, as intermolecular collisions are negligible [7]. FMMR operating on water propellant with a heating element temperature of 600 K, and propellant storage pressure of  $\mathcal{O}(\sim 100 \text{ Pa})$  can produce an  $I_{sp}$  of 68 s [4]. If argon propellant is used instead, the  $I_{sp}$  is 45 s [4]. These  $I_{sp}$  values may not look as an improvement, but other micro-propulsion technologies require heavy storage tanks to store the propellant. A nitrogen propellant stored at 20 MPa and 300 K in a spherical titanium tank with a safety factor of 2.0 requires a tank to propellant mass ratio ( $M_t/M_p$ ) of 1.0, decreasing the effective specific impulse ( $I_{sp, \text{eff}}$ ) of a typical cold gas thruster to half the value of the intrinsic specific impulse ( $I_{sp}$ ) [4]. As described by Micci et al. [4], the  $I_{sp, \text{eff}}$  is the effective specific impulse after taking into account the extra mass associated with the minimum operating pressure of the thruster, the propellant loss due to valve leakage, and the storage tanks. Due to the unusually low plenum pressures (50 - 500 Pa) used in the FMMR, some propellants can be stored as a solid or a liquid (e.g.,  $\text{H}_2\text{O}$ ). For example, the vapor-pressure of ice is  $\sim 50 \text{ Pa}$  at 245 K and if a higher plenum pressure is needed to produce higher thrust, waste heat from the spacecraft could be used to increase the vapor pressure in the storage tank [4]. Since the FMMR can operate at the

vapor pressure of ice, the propellant could be vaporized on demand to generate thrust. The low-pressure requirement allows the use of very light storage tanks and decreases valve leakage, which depends strongly on the pressure difference between the tank and the ambient and the molecular mass of the propellant [4]. Therefore, the  $I_{sp, eff}$  of FMMR is nearly equal to its  $I_{sp}$ .

Unfortunately, FMMR suffers from significant thermal energy losses due to thermal dissipation inherent in the working principle [8]. An estimate of the heat loss per heating element by Micci and Ketsdever [4] predicts 20 mW due to radiation and 150 mW due to conduction through the pedestal at 300 K. FMMR operating with 40 expansion slots ( $100 \mu\text{m} \times 1 \text{cm}$ ) requires 6000 to 8000 mW to heat the propellant gas to obtain the expected performance [4]. In outer space, the estimated heat loss of this device would be 6800 mW, which is about the same amount needed to heat the propellant. The total power required to operate FMMR would be 12800 to 14800 mW. In contrast, the proposed rarefied gas electro jet (RGEJ [9]) micro-thruster aims to improve cold gas thruster technology by increasing the  $I_{sp}$  while retaining the advantageous characteristics of both cold gas thrusters and FMMR without the excessive heat loss associated with the FMMR design.

A different technology called the micro-plasma thruster (MPT [10]), developed to improve the performance of cold gas thrusters, consists of a cylindrical geometry comprising a constant area flow section combined with a diverging exit nozzle with dimensions of the  $\mathcal{O}(\sim 100 \mu\text{m})$  [11]. The MPT operates in the abnormal glow regime [11]. A direct-current micro-discharge is used to add thermal energy to the gas in order to increase the performance of cold gas thrusters. The MPT operates in the slip flow

regime with ( $Kn \sim 0.01$ ) at the inlet and ( $Kn \sim 0.08$ ) at the exit plane and requires a minimum operating pressure of 100 Torr, two orders of magnitude higher than the RGEJ [11]. Although the  $Kn$  numbers in the MPT between the inlet and the exit plane are comparable to RGEJ, the expansion and heating of the flow in the MPT occurs predominantly in the diverging nozzle (350  $\mu\text{m}$  long). This explains why there is only a 2-3% thrust difference between cases with no-slip and slip boundary conditions in the MPT, since most of the device (the constant area section, 500  $\mu\text{m}$  long) experiences low  $Kn$  numbers ( $0.01 < Kn < 0.03$ ) [11]. Since the device has such small volume ( $V$ ) to surface ( $S$ ) ratio ( $V/S = 39.2 \mu\text{m}$ ) the thermal losses due to conduction to the walls are expected to be significant. For comparison, the RGEJ has a ( $V/S = 1.5 \text{ mm}$ ) and operates in the slip flow regime with ( $Kn \sim 0.01$ ) at the inlet and ( $Kn \sim 0.1$ ) at the exit plane, with more than 50% of the device experiencing ( $Kn > 0.05$ ). Using no-slip boundary conditions would produce a drastically different solution for the RGEJ. The MPT's  $I_{sp}$  is 74 s for the 750 V case, an improvement over cold gas thrusters with the same geometry and operating conditions by a factor of ( $\sim 1.5$ ) [11]. However, the MPT's thrust effectiveness of 50  $\mu\text{N/W}$  is very low due to thermal losses through the isothermal walls at 300 K [10], [11]. The thrust effectiveness is defined in this study as the difference between the thrust with and without plasma-aided technology divided by the total electrical power consumed.

Other designs improving the  $I_{sp}$  of cold gas thrusters using plasma-aided technologies are the radio-frequency electrothermal thruster (RFET [12]), and the microwave electrothermal thruster (MET [13]). The RFET consist of a cylindrical geometry, 18 mm in length and 4.2 mm in diameter, composed of alumina with copper

electrodes operating at a frequency of 13.56 MHz and an electric potential difference of 240 V. For an argon gas plenum pressure of 1.5 (Torr), the power consumption is 10 W, causing an ionization degree of 0.44% and a maximum electron number density of  $2 \times 10^{18} \text{ (m}^{-3}\text{)}$  [12]. The predicted mass flow rate and thrust are 100 SCCM and 2.619 mN [14]. The MET has a cylindrical dielectric chamber, 10 mm long and 1.5 mm in diameter, with a metal rod antenna on the axis to produce microwave signals at 4 GHz that generate the plasma and heat the gas. The heated argon gas in the chamber at high pressure (10-50 kPa) is expanded through a de Laval nozzle. An experiment performed with 31 kPa plenum pressure produced a 60 SCCM mass flow rate and a 1.4 (mN) thrust. Both of these thrusters operate with higher power consumption than the target power budget of RGEJ ( $< 5 \text{ W}$ ), but they produce higher specific impulse ( $I_{sp} > 80 \text{ s}$ ) than the RGEJ and the MPT. These designs help illustrate the many different examples of plasma-aided technology thrusters currently under investigation.

The RGEJ design aims to increase the efficiency of the energy exchange from the electrical source to the propellant, avoiding the high thermal dissipation problem associated with FMMR, which prevented FMMR's applications, by heating the gas directly instead of using heater chips, while keeping the advantageous characteristics of FMMR. The RGEJ concept involves localized embedding of electrodes with a DC or an RF applied potential difference, along the dielectric surface of its walls to produce a glow discharge plasma [8]. The charged particles in the plasma are accelerated by the electric field, heating the propellant. Since the deposition of energy is localized via the electrodes, the energy budget should reduce, increasing the thruster efficiency. The presence of charged particles implies that both electric and magnetic fields can be used

to produce thrust. In this study, magnetic fields were not applied and the thruster operates similarly to an electrothermal thruster, using a DC discharge to heat the gas. RGEJ operates in the slip flow regime, which decreases viscous losses and heat transfer to the wall. The low minimum required operating pressure (1 Torr), a hundredth of the MPT's operating pressure (100 Torr), is selected by design to match the vapor pressure at nominal storage temperatures of many liquid or solid propellants (e.g. H<sub>2</sub>O). The goal is to develop eventually a phase-change thruster concept to avoid heavy storage tank and valve leakage problems, vaporizing the propellant on demand to generate thrust similarly to FMMR [4]. RGEJ is predicted to have higher specific impulse than cold gas thrusters as well as significant advantages in size, weight, and power (SWaP) over other micro-propulsion devices despite its design simplicity, not requiring any neutralizers, heating elements, or a heavy fuel storage tank if a liquid or solid propellant is used [8].

In this dissertation, a finite element and a finite difference based numerical analysis of the rarefied gas and the ionized gas in the FMEJ micro-thruster is implemented to calculate the performance parameters of the device. The cases presented, display a non-optimized design with a rectangular channel geometry and adiabatic conditions at the wall with low plenum pressure (1 Torr) operating at different DC voltages to study the effect of power deposition from the plasma to the gas. The main difference between RGEJ and FMMR consist of the power deposition method. No heating element is required in RGEJ. Instead, the gas is heated by the volumetric thermal heating source, increasing the efficiency of the energy transfer. There are many differences between the RGEJ and the MPT. The MPT has higher plenum pressure

(100 Torr) which requires a complex argon-chemistry model, assumes isothermal walls, has a cylindrical geometry with an exit expansion nozzle, and a smaller volume/surface ratio, which increases particle loss to the walls as well as thermal losses. The RGEJ has lower plenum pressure (1 Torr) to develop eventually a phase-change thruster concept, similar to FMMR, which has the added advantage of combining microelectromechanical systems (MEMS) fabrication techniques with a simple, lightweight design due to the low plenum pressures, which causes a smaller pressure difference between the thruster inlet and the ambient than the MPT. RGEJ is designed with insulated walls, and has a rectangular slot geometry to prevent catastrophic plugging of the throat, and does not have an expansion nozzle since for many micro-propulsion devices the Reynolds number ( $Re$ ) is so low ( $\sim 100$ ) that the viscous losses counteract any improvement in  $I_{sp}$ . It is important to emphasize that simulating the thruster with adiabatic conditions requires a more robust iterative procedure between the loosely coupled modules of the code than if isothermal walls are used. Although argon was used as the propellant for the RGEJ for simplicity of the numerical simulation, other propellants (e.g.  $H_2O$  or  $NH_3$ ) may be preferable since they can be stored in solid or liquid form to reduce storage tank weight and valve leakage.

### **Performance Parameters**

In order to evaluate the performance of the micro-thrusters, several parameters must be calculated and compared. The mass flow rate ( $\dot{m}$ ) is a measurement of how much mass per time flows through the thruster. This parameter can be used to calculate the total propellant mass necessary for a certain amount of operating time of the thruster. The thrust ( $F_{Thrust}$ ) is the propulsive force of a propulsion system, and in space, it dictates the achievable acceleration of a space vehicle given the mass of that vehicle.

As previously mentioned, the amount of spacecraft momentum change caused by a propulsion system operation is called the impulse. The minimum finite change of momentum that can be delivered by a thruster (the minimum impulse) is defined as the minimum impulse bit ( $I_{bit}$ ). The velocity change caused by an impulse to the vehicle is termed the Delta-V ( $\Delta-V$ ), which is a measurement of the effort required for making an orbital maneuver. These values depend on the valve speed and the mass of the spacecraft in question, respectively. The minimum impulse bit determines the ability of a thruster to do minute momentum adjustments for attitude and orbit control, while the Delta-V produced by a propulsion system determines its range of application for a given satellite.

The specific impulse ( $I_{sp}$ ) is defined as the change in momentum per unit of propellant weight (using Earth's frame of reference) spent and it is a measure of the efficiency of a propulsive system in terms of how much mass is needed to produce a certain amount of thrust. The total efficiency ( $\eta_T$ ) of an electrically powered thruster is defined as the jet power divided by the total-electrical power into the thruster. It indicates how efficiently the power is converted to kinetic energy of the propellant in an electric propulsion system. The thrust effectiveness ( $\zeta_{Thrust}$ ) is the ratio of thrust vs. total electrical power into the thruster. The following equations are used to calculate these parameters at the exit plane of the thruster [11], [2]

$$I_{bit} = F_{Thrust} \Delta t, \quad (1-1)$$

$$\Delta v = \int_{t_0}^{t_1} \left( \frac{F_{\text{Thrust}}}{m} \right) dt. \quad (1-2)$$

$$\dot{m} = (\rho u A)_{\text{exit}}, \quad (1-3)$$

$$F_{\text{Thrust}} = (\dot{m}u + pA)_{\text{exit}}, \quad (1-4)$$

$$I_{sp} = \frac{F_{\text{Thrust}}}{\dot{m}g_0}, \quad (1-5)$$

$$\eta_T = \frac{P_{\text{jet}}}{P_{\text{in}}} = \frac{F_{\text{Thrust}}^2}{2\dot{m}P_{\text{in}}}, \quad (1-6)$$

$$\zeta_{F_{\text{Thrust}}} = \frac{F_{\text{Thrust}}}{P_{\text{in}}}, \quad (1-7)$$

where the variables  $\rho$ ,  $u$ , and  $p$  are the density, velocity component in the x-direction, and pressure of the gas at the exit plane of the thruster, while  $P$  indicates the power.  $H$  and  $W$  are the height and width of the thruster, respectively, use to calculate the area ( $A$ ), where  $W$  is assumed to be 1.0 cm. The gravitational constant  $g_0$  is 9.81 m/s<sup>2</sup>.

The dissertation has the following structure:

[Chapter 2](#) provides a review of micro-propulsion devices. Several micro-propulsion technologies are described and their performance characteristics are provided to compare their advantages and disadvantages for different applications.

[Chapter 3](#) provides a background on gas discharge physics. The voltage-current characteristics of a DC discharge are examined, the glow discharge mode is explained, and a methodology to estimate sputtering is described.

[Chapter 4](#) explains the governing equations used in each numerical module and the thermal analysis.

[Chapter 5](#) explains the numerical models in each module and the thermal analysis.

[Chapter 6](#) shows the validation/benchmarking of the numerical modules.

[Chapter 7](#) shows and explains the results obtained by the numerical simulations and estimates the heat loss through conduction and radiation from the thrusters to justify the assumption of adiabatic walls.

[Chapter 8](#) gives a summary of the results and contributions to the field of science; additionally, it proposes future directions to continue improving the RGEJ.

## CHAPTER 2 MICROPROPULSION TECHNOLOGIES

### **Introduction to Micro-propulsion Devices**

Some of the competing micro-propulsion technologies were mentioned in the previous chapter along with their strength and weaknesses. In order to understand the different designs of micro-propulsion systems and their limitations, a survey of existing technologies is presented in this chapter. This survey is not intended to be comprehensive; instead, it aims to provide enough information to appreciate the complications that come with the miniaturization of existing technologies.

For larger satellites, the available conventional technologies have been used reliably. For smaller satellite, successful implementation of conventional technologies become increasingly more difficult due to size and weight limitations. In the last two decades, several prototypes have been designed and tested with different degrees of success. Extensive reviews and similar surveys of the available thruster designs and their performances are available in literature [4], [8], [11], [15], [16], [17], [18], [19]. In this survey, the focus is on chemical and electric propulsion categories of thruster designs and their subtypes based on the working principle, design details, and propellant types.

### **Chemical Propulsion Devices for Small Satellites**

Chemical propulsion options are usually characterized by limited specific impulse [16]. Their thrust levels may exceed several Newton for micro-propulsion designs. Chemical propulsion options are of particular interest when rapid maneuvering is required, such as rapid plane change or orbit change, or proximity operations near other

spacecraft, such as for inspection purposes, where sufficient agility is required for collision avoidance [16].

### **Cold Gas Thrusters**

The cold gas thruster is one of the most simple propulsion systems. A gas from a high-pressure supply tank that expands through a valve and a nozzle produces thrust. Cold gas thrusters offer low impulse bits and can operate with contamination-free, non-toxic propellant (e.g.,  $N_2$ ) [4]. Thrust values range from 4.5 mN to 100 N and some designs, such as Moog's thruster model 58x125A, can weigh as little as 9 grams and are as small as (12 × 35 mm) [15], [19].



Figure 2-1. Cold gas thruster from Moog, model 58x125A [15]. This cold gas thruster uses  $N_2$  for propellant, has a thrust of 4.4 mN, a mass of 9 g, a size of (11.9 × 34.7 mm), operational pressure from 0 to 50 psia, an  $I_{sp}$  of 65 s, an impulse bit of 100  $\mu$ N-s, and it requires 10 W to operate its valve.

Most of the cold thruster designs in existence were not designed for micro-spacecraft applications. The power levels required for valve actuation (~ 10 W for the Moog 58x125A model) exceed today's CubeSat capabilities [15].

Cold gas thrusters have low specific impulse,  $I_{sp} < 75$  s for  $N_2$  propellant [4], leading to large propellant mass fractions. The larger propellant mass fraction increases the propellant system mass since a heavy tank is required to contain the high-pressure

gas supply (~ 3500 psia) [4]. The large storage pressure also creates a risk of propellant leakage across valve seats. Several approaches have been considered to avoid some of the problems with the cold gas thruster and are elaborated in detail by Mueller et al. [15]. The following table lists the typical cold gas performances, depending on propellant type using data from Micci et al. [4].

Table 2-1. Cold gas propellant performance. Assuming propellant is at 25°C and the flow expansion is to zero pressure in the case of the theoretical value [4].

Propellant	Molecular weight (kg/kmol)	Density (3500 psia, 0 °C) (g/cm <sup>3</sup> )	Isp (s)	
			Theoretical	Measured
Hydrogen	2.0	0.02	296	272
Helium	4.0	0.04	179	165
Neon	20.4	0.19	82	75
Nitrogen	28.0	0.28	80	73
Argon	39.9	0.44	57	52
Krypton	83.8	1.08	39	37
Xenon	131.3	2.74	31	28
Freon 12	121	-	46	37
Freon 14	88	0.96	55	45
Methane	16	0.19	114	105
Ammonia	17	Liquid	105	96
Nitrous oxide	44	-	67	61
Carbon dioxide	44	Liquid	67	61

Neither hydrogen nor helium is commonly used, due to the requirement of a large heavy tank caused by the low gas densities and leakage problems due to the low molecular weight of these gases [4].

### **Mono Propellant Thrusters**

Monopropellant thrusters use only one working propellant. The propellant undergoes an exothermic chemical reaction that provides the power to generate thrust producing a typical specific impulse of ~220 s [4]. If hydrazine is used as a propellant, it decomposes catalytically in a catalyst bed consisting of iridium coated alumina pellets.

The decomposition is highly exothermic and produces a 1000 °C gas that is a mixture of nitrogen, hydrogen, and ammonia [4]. Ammonia decomposes into hydrogen and nitrogen and the degree of decomposition depends on the feed pressure, catalyst type, and geometry, among other factors. The smallest hydrazine thrusters have a thrust in the (0.9 - 4.45 N) range [4]. Hydrazine thrusters are suitable as the primary propulsion system for intermediate to low ( $\Delta$ -V) maneuvers ~1000 m/s and some designs, such as the Primex MR-103 C/D model, can produce small impulse bits (50 – 100  $\mu$ N-s) for fine attitude control in small satellites [4].

A hydrazine milli-Newton thruster (HmNT) at JPL may fit the mass and volume envelope of a CubeSat for small to intermediate ( $\Delta$ -V) applications [15], [20].

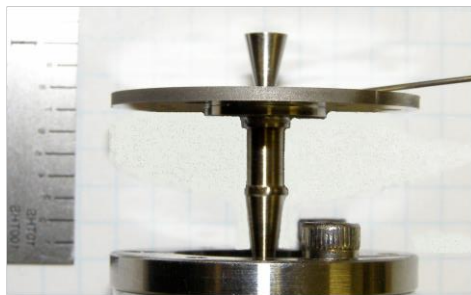


Figure 2-2. JPL Hydrazine milli-Newton Thrusters (HmNT), a monopropellant technology [20]. It has a thrust of 129 mN, a mass of 40 g, a volume of 8 cc, an  $I_{sp}$  of 150 s, and it requires 8 W (open)/ 1 W (hold) to operate its valve. It can produce minimum impulse bits of 50  $\mu$ N-s [4], [15].

Two disadvantages of hydrazine engines are its toxicity and flammability, which results in complexity and cost of ground handling and propellant loading procedures [4].

Another technology available uses hydrogen peroxide, purified to 90% or higher concentration. Hydrogen peroxide is self-decomposing at high temperatures or when a catalyst is presented. Hydrogen peroxide thrusters may fill a similar function as the HmNT hydrazine thrusters. The main advantage of hydrogen peroxide is that it is non-

toxic unlike hydrazine [15]. The disadvantage is that hydrogen peroxide slowly decomposes when it is heated or exposed to a catalyst, and almost any organic residue can act as a catalyst [15]. Other monopropellant technologies are explained by Soni [8] and Micci et al. [4].

The main problems with the monopropellant thrusters for small satellite applications seem to be the toxicity of the propellant, the storage of the propellant, and the heat loss through the thruster structure along with degradation of the catalyst bed depending on the propellant and design used.

### **Bipropellant Thrusters**

Bipropellant thrusters require two types of propellants, a fuel and an oxidizer, and are pressure regulated to maintain the mixture ratio. The added complexity and dry mass associated with the design is a tradeoff to obtain higher specific impulse (~ 300 s) than the one in monopropellant thrusters [4], [15]. Due to the additional components in bipropellant thrusters, the monopropellant thrusters outperform them in terms of wet propulsion mass below  $\Delta-V$ 's of approximately 500-1000 m/s, depending on spacecraft mass [15]. The added complexity increases the cost of bipropellant systems, usually making them more expensive than monopropellant thrusters [4].

A good example of a miniaturized bipropellant thruster is the MEMS-micro fabricated bipropellant rocket engine achieved by London et al. [21]. The thruster chip consists of an integrated thrust chamber, nozzle, turbine pumps, and inlet valves [22]. Some of the challenges associated with miniaturizing bipropellant engines include managing the losses in combustion efficiency due to reduced mixing and vaporization and dealing with an increase in heat losses into the engine structure resulting in thermal control issues [4].

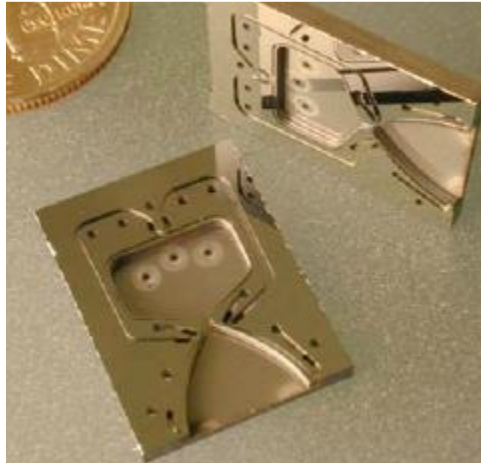


Figure 2-3. MIT micro-bipropellant engine concept [22]. Testing has been performed with gaseous oxygen and ethanol, the thrust obtained is 2.7 N, with an Isp of 300 s. The entire assembly of the thruster chip is about 20x5 mm and consists of an integrated thrust chamber, nozzle, turbine pumps, and inlet valves [15].

### **Electric Propulsion Devices for Small Satellites**

The acceleration method producing the thrust is typically used to describe the electric thruster. These methods are separated into three categories [2]:

- Electrothermal
- Electrostatic
- Electromagnetic

#### **Electrothermal Thrusters**

Electro-thermal thrusters are a class of electric propulsion devices that convert electrical energy into thermal energy of the propellant. Then, the propellant is expanded through a nozzle, or through a long thin channel, to produce thrust. Elevating the propellant temperature increases the specific impulse.

## Free molecule micro-resistojet (FMMR)

In this concept, propellant from a plenum at very low stagnation pressures (50 to 500 Pa) flows through very thin micro slots (1-100  $\mu\text{m}$ ) such that the flow is in the free molecular regime [4]. Collisions over the characteristic thruster dimensions only take place with the hot wall surfaces, not among the molecules of the propellant flow due to the degree of rarefaction of the gas. Since there is no momentum exchange between the flow particles, all the particles colliding with the heater wall surface will acquire the kinetic energy equivalent to the heater wall temperature [15]. The increase in propellant kinetic energy increases the  $I_{sp}$  of the thruster over similar cold gas thrusters.

There are different designs for the FMMR thruster, they are all based on the same concept but the geometry is adapted to improve heat transfer to the gas and minimize heat losses. In the design shown in Micci et al. [4], the FMMR geometry is as follows,

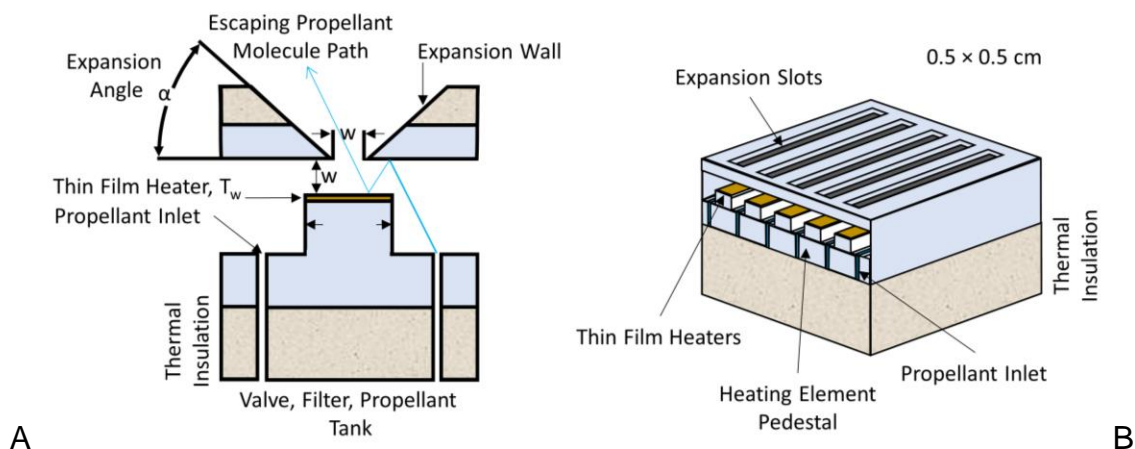


Figure 2-4. FMMR thruster design [4]. A) Schematic cross section showing the heating element arrangement with the expansion slot, and B) multi-slot ( $w = 100 \mu\text{m}$ ) configuration with a  $0.5 \times 0.5 \text{ cm}$  cross-sectional area.

where the design requirement is to arrange the thin film heater at a given stagnation temperature to be the last surface contacted by a propellant molecule before it is ejected from the expansion slot. Using this design, with ten different  $100\ \mu\text{m} \times 8\ \text{mm}$  slots and expansion angle of 54.74 degrees, the FMMR is able to produce 0.25 mN of thrust at an  $I_{sp}$  of 45 s for argon propellant and thin film heater temperature of 600 K. The same design working under the same parameters using water as a propellant is able to produce an  $I_{sp}$  of 68 s. The effect of propellant gas (molecular mass, MM) on the  $I_{sp}$  has been investigated and shown in Micci et al. [4] for thin film heater temperature of 600 K, where the  $I_{sp} \propto \sqrt{1/MM}$ . Gases with smaller MM produce higher  $I_{sp}$  (e.g. helium,  $I_{sp} \sim 140\ \text{s}$  [4]), a similar effect is observed in cold gas thrusters. However, propellants that can be stored in liquid or solid states at standard temperature and pressure (STP) such as water or ammonia are favored to decrease propellant tank mass and valve leakage. The heat loss analysis, shown previously in chapter 1, is performed using this design with forty  $100\ \mu\text{m} \times 1\ \text{cm}$  slots.

A different design has the slots etched into the heater chip, with the resistive elements patterned around the periphery of the slots as shown in [Figure 2-5](#) [23].

Experimental testing with a heater chip temperature of 580 K, using water propellant, achieved thrust values and specific impulse of 129  $\mu\text{N}$  and 79.2 s, respectively [24]. This design has higher  $I_{sp}$  at lower heater temperature than the one in Micci et al. [4]. However, the main problem associated with the FMMR concept is the low energy conversion efficiency due to heat loss which increases the power consumption and may present a significant demand on the power system of a small satellite [8], [15].

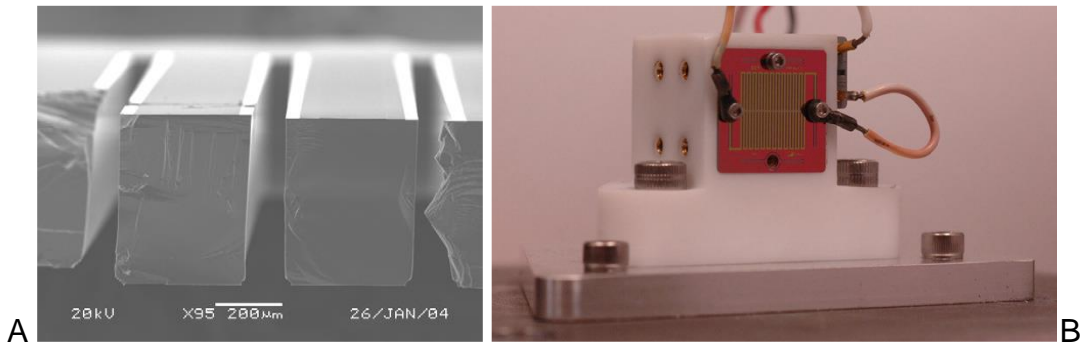


Figure 2-5. FMMR thruster [23]. A) Scanning electron microscope side image of cleaved expansion slots, and B) heater chip installed in Teflon flight plenum.

### Low-power DC arcjets

Arcjet thrusters use an electrical arc discharge to impart additional energy to the propellant in order to increase the  $I_{sp}$  at the cost of increased power consumption. The design typically has the electrodes placed at the nozzle exit to minimize heat loss. It can operate with gaseous, liquid, or solid propellant. If the device uses gaseous propellant, it functions as a warm gas thruster with the arc discharge heating the flow. If the design uses solid propellant, the arc ablates a small amount of material from the propellant block, which sometimes is designed to act as the cathode. Subsequently, the vaporized material is accelerated using thermal expansion [8].

The Vacuum Arc Thruster (VAT) is an example of an ablative pulse plasma DC arcjet thruster [15]. A high voltage between two metal electrodes causes high electric field near surface roughness spikes. The high power density in the spikes leads to vaporization, electric breakdown, and plasma generation in an arc discharge. The plasma plume expands into a vacuum and produces a thrust pulse. Test on a JPL micro-Newton thrust stand demonstrated up to 100  $\mu\text{N}\cdot\text{s}$  impulse bits for 100 Hz pulse trains using Cr as the propellant block material [25]. This technology has demonstrated

the ability to achieve very high specific impulse of 1000-3000 s [26], [25]. The thruster heads weigh ~ 100 g and the power consumption range between 1-100 W with an effectiveness of up to 10  $\mu\text{N/W}$  [15], [25].

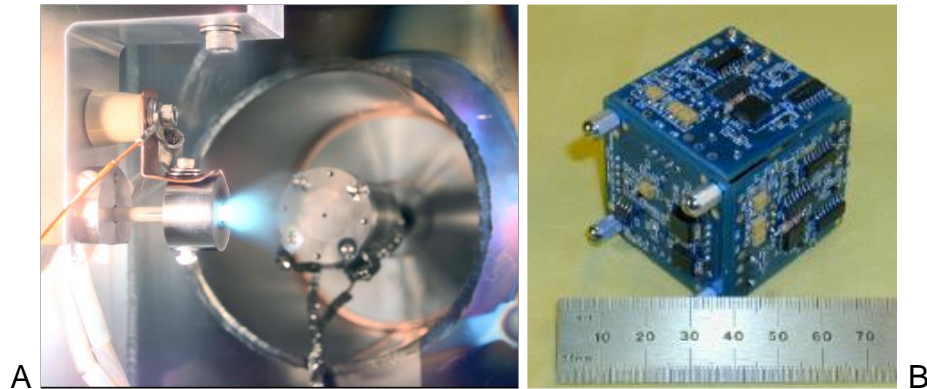


Figure 2-6. VAT thruster. A) VAT firing on thrust stand, and B) power processing unit (PPU) configured for CubeSat with mass of 150 g capable of supplying four VAT thruster heads with power using a 12-24 V bus voltage [15], [25].

The advantages of the VAT are its very small impulse bits for attitude control, its solid propellant storage, and integrated propellant design, which allows for a compact, modular propulsion system. The negative characteristics of the design are that large ( $\Delta$ -V) applications may not be possible due to the small impulse bits that limit the thrust and impulse values [15]. Rapid maneuvering may not be possible due to low thrust values. The VAT main applications could be precision pointing and attitude control.

### **Microcavity discharge thrusters**

The Micro-Cavity Discharge Thruster (MCD) is a type of electrothermal thruster concept that utilizes a micro discharge in a cavity as small as 10  $\mu\text{m}$  in diameter to heat the gas as high as 1500 K [15]. The gas is heated by an applied voltage (400-1200 V<sub>AC</sub>) to the electrodes at a frequency of 50-150 kHz, which causes the gas to partially ionized

with a low degree of ionization ( $\ll 1\%$ ) [15]. The following figure shows the thruster concept and etched micro-nozzle [15], [27].

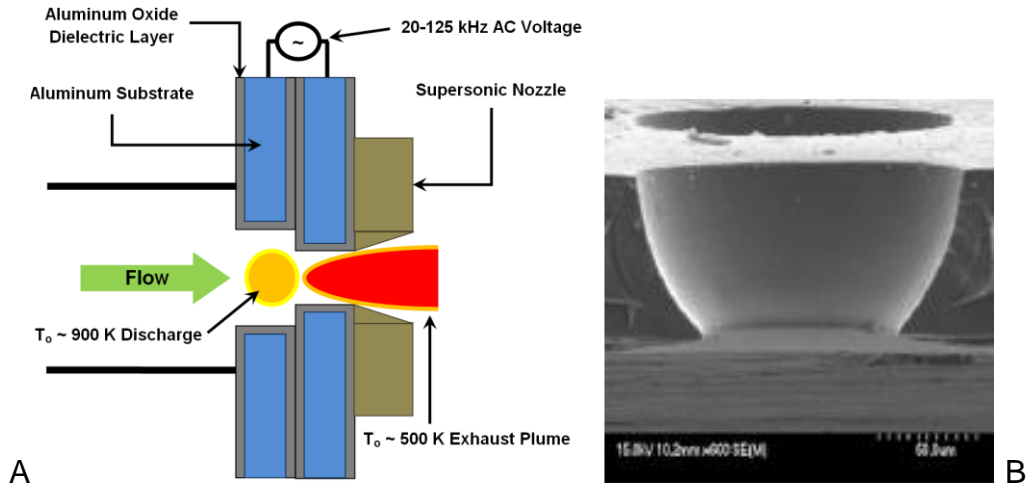


Figure 2-7. Electro-thermal thrusters. A) Schematic of MCD electro-thermal thruster concept, and B) micro-nozzle [15], [27].

For an array of 4 cavities, each with  $120 \mu\text{m}$  throat and  $210 \mu\text{m}$  exit plane diameter, the mass flow rate and thrust values obtained were between  $0.99\text{-}5.22 \text{ mg/s}$  and  $0.6\text{-}2.7 \text{ mN}$ , respectively, operating with plenum pressures of  $120\text{-}240 \text{ kPa}$  and  $0.25 \text{ W}$  per cavity [15]. These values produce an  $I_{sp}$  of  $50\text{-}60 \text{ s}$ . The MCD thrusters operate at higher gas temperatures than conventional resistojets, promising higher  $I_{sp}$ . Their design has higher thrust and effectiveness than electrospray arrays, yet lower specific impulse values [15]. Their possible uses include attitude control, rapid slew maneuvers, proximity operations, and low ( $\Delta\text{-}V$ ) applications [15].

### Micro-plasma thruster (MPT)

The micro-plasma thruster (MPT [10]), developed to improve the performance of cold gas thrusters, consists of a cylindrical geometry comprising a constant area flow section combined with a diverging exit nozzle with dimensions of  $\mathcal{O}(\sim 100 \mu\text{m})$  [10], [11].

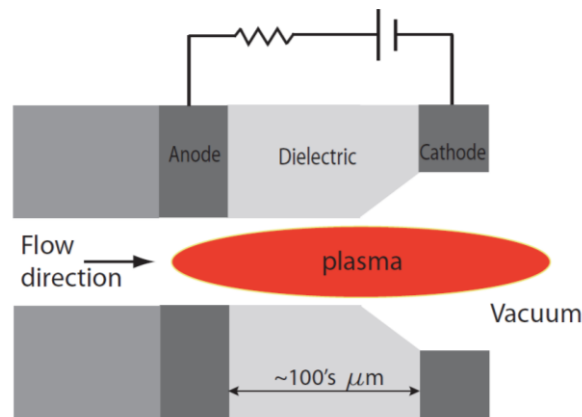


Figure 2-8. Schematic of the micro-plasma thruster (MPT) [11].

The geometry consists of an axisymmetric constant area section, a diverging section, and a second constant area section, which are 500, 200, and 120  $\mu\text{m}$  in length, respectively. The radiuses of the upstream constant area section and exit section are 50 and 150  $\mu\text{m}$ . The inlet total pressure is 100 Torr and a small but nonzero outlet pressure is required to stabilize the numerical scheme in the “vacuum” domain. The temperature was constant at 300 K for the inlet, the outlet, and the solid walls.

The MPT has a mass flow rate of 0.14 mg/s, a thrust of 67.4  $\mu\text{N}$  for the cold gas thruster case, and a thrust of 100  $\mu\text{N}$  for the 750 (V) and 650 (mW) plasma-aided case which produces an  $I_{sp}$  of  $\sim 74$  (s) [10], [11]. These values make the MPT’s thrust effectiveness and total efficiency equal to 50 ( $\mu\text{N/W}$ ) and 0.6%, respectively.

### Electrostatic Thrusters

Electrostatic thrusters accelerate the propellant to high exit velocities using mainly Coulomb force. The design uses electrostatic forces to accelerate heavy charged ions towards the thruster exit. Electrostatic thrusters are classified into three main types: gridded ion engines, Hall-effect thrusters, and colloid thrusters.

## **Miniature ion engines**

In an ion engine, the propellant is ionized in a discharge chamber and ions are extracted from this chamber using an electrostatic grid system. Usually, heavy inert gases are used as a propellant (e.g. xenon). Two main types of ion engines are available: DC electron bombardment (Kaufmann-type thruster) and Radio-Frequency (RF) ion engine [15].

In a DC electron-bombardment ion engine, a plasma is generated in a hollow cathode. From this plasma, electrons are extracted and injected into the discharge chamber to ionize the propellant gas by accelerating the electrons towards an anode surface [15]. Typically, the design uses permanent magnets to increase the engine efficiency by reducing electron loss to the walls and increasing the electron path through the discharge.

In an RF ion engine, an electromagnetic coil is wrapped around a dielectric discharge chamber to generate an oscillating, axial magnetic field that generates an oscillating azimuthal electric field [15]. Free electrons always present in a gas are accelerated with enough speed to cause ionization of the neutral particles, which increases the number of free electrons, causing an electron avalanche that forms the plasma.

The effectiveness, the thrust per power, of the DC discharge engines is typically higher than for RF discharges, but no life-limiting internal cathode is needed for the second design, making RF engines very desirable for long-term operations. Both designs require a neutralizer to avoid spacecraft charging, consisting of another hollow cathode outside the thruster that neutralizes the positively charged ion beam exiting the thruster.

In recent years, different miniature ion engines have been developed for formation flying applications of space telescopes, such as the JPL Miniature Xenon Ion Thruster (MiXI [28]), the  $\mu$ NRIT-2.5 Miniature Ion Thruster [29], and the Miniature Radio Frequency Ion Thruster (MRIT [15]).

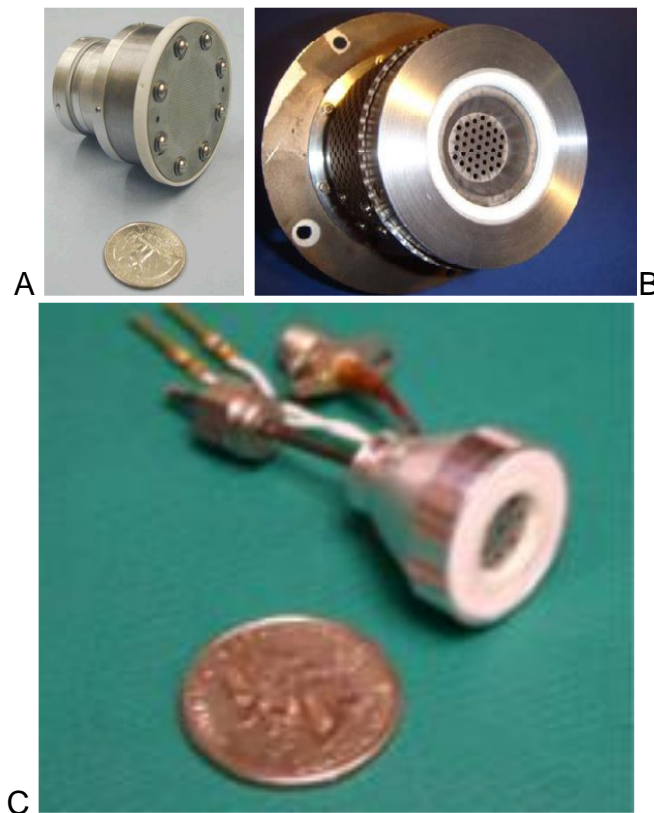


Figure 2-9. Ion thrusters. A) JPL Miniature Xenon Ion thruster (MiXI) [28], B) the  $\mu$ NRIT-2.5 miniature ion thruster of the University of Giessen [29], and C) Miniature Radio Frequency Ion Thruster (MRIT) of the Pennsylvania State University [15].

Miniature ion engines have multiple beneficial characteristics as space telescopes propulsion systems such as the use of non-contaminating propellant, which is of great importance near sensitive optical surfaces, and the ability to modulate the thrust amplitude without inducing jitter [8]. The following table shows the performance parameters of these three designs [15].

Table 2-2. Micro-ion engine performance [15].

Parameter	Units	MiXI	$\mu$ NRIT-2.5	MRIT
Propellant	-	Xe	Xe	Ar
Thrust	(mN)	0.01 - 1.5	0.05 - 0.6	0.001 - 0.06
Specific Impulse	(s)	2500 - 3200	2861	5480
Power	(W)	13 - 50	13 - 34	-
Electrical Efficiency	(%)	>40	4 - 47	15
Diameter	(cm)	3	2.5	2
Mass	(g)	200	210	-

As observed in the previous table, these engines have a high specific impulse, but higher power consumption and mass requirements in comparison to other technologies. In addition, performance deterioration due to grid erosion caused by heavy ion bombardment is a problem encountered in gridded ion thrusters [8]. In order to adapt micro-ion engines to small satellites, their size, as well as the size of the power-processing unit, would have to be drastically reduced.

### Miniature hall thrusters

In a Hall thruster, the external cathode, outside the thruster, emits electrons that are accelerated towards the anode located inside an annular channel. The electrons encounter a radial magnetic field near the exit plane of the thruster. The Lorentz force, which is caused by the combined electric and magnetic forces on a point charge due to electromagnetic fields, makes the electrons gyrate around the magnetic field lines and drift azimuthally through the annular channel causing ionization. The ions are accelerated out of the thruster by the electric field generated by the electric potential difference between anode and cathode. The ion flow exiting the thruster generates the majority of the thrust. The Larmor radius, the radius of circular motion of a charged particle in the presence of a uniform magnetic field, is larger for ions than for electrons due to the higher inertia of the ions. Since the ions are affected less by the magnetic

field, the ions move out of the channel without the magnetic field affecting their path. The external cathode neutralizes the ions outside of the channel by providing a source of electrons. As a result, Hall thrusters are more compact than ion engines for a given ion beam strength [16]. The main difference between Hall thrusters and ion engines is that Hall thrusters do not require grid systems.

A Hall thruster design can be categorized as either a stationary plasma thruster (SPT) or a thruster with anode layer (TAL) design [2]. The main difference is that SPT design has a wide acceleration zone and uses dielectric insulating walls such as alumina ( $\text{Al}_2\text{O}_3$ ) with low sputtering yield and low secondary electron emission coefficient. The TAL design has a narrow acceleration zone and metallic conducting walls with exit plane metallic guard rings biased at cathode potential to reduce the electron loss along the field lines. The SPT type was used in the Meteor spacecraft in 1971. Unfortunately, neither of these designs is suitable for miniaturization.

The miniaturization of Hall thrusters faces many challenges since the reduction in size requires smaller electron Larmor radius (stronger magnetic fields) to avoid excessive electron losses to the walls and the associated decrease in electrical efficiency [15]. A micro-Hall thruster requires stronger magnets. However, the smaller devices suffer from increased heating of the magnets by the plasma, which could lead to demagnetization and the loss of electron containment causing the electric efficiency of the device to drop drastically. A miniature 50 W Hall thruster concept by MIT suffered from this particular problem, having a poor efficiency of 6% [30].

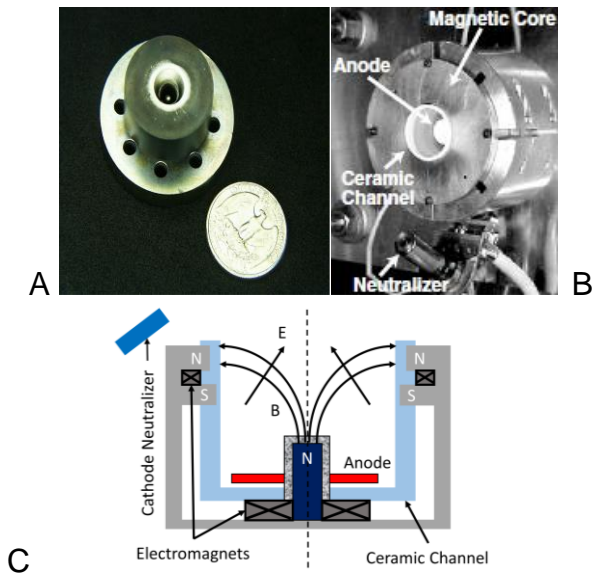


Figure 2-10. Hall thrusters. A) MIT 50 W Hall Thruster, B) 3-cm CHT device, and C) Schematic of 3-cm CHT device [15].

A new type of miniature Hall thruster has been developed by Princeton Plasma Physics Laboratory (PPPL) to improve the efficiency observed in previous versions [15]. This new design uses a cylindrical Hall thruster (CHT [31], [32]) geometry with a largely axial magnetic field, instead of the annular flow channel with a radial magnetic field [33]. In the CHT design, the axial magnetic field is concentrated at the anode end of the channel causing electrons to be mirrored back, away from the anode region [15]. The CHT efficiency, ~30%, is higher than for other micro-Hall thrusters. However, it is significantly less than for conventional Hall thrusters, which may suggest performance deterioration as a result of downscaling [2]. [Table 2-3](#) shows the performance parameters of several micro-Hall thrusters and their range of efficiency [15].

The improvement in specific impulse and electrical efficiency of the new design looks promising. The miniature Hall thrusters have some advantages over ion engines since they require a power-processing unit capable of producing 300 V instead of 1 kV and fewer power supplies than their counterparts do.

Table 2-3. Small and micro-Hall thruster performances [15].

Parameter	Units	BHT-200	SPT-30	MIT	PPPL CHT 2.6	PPPL CHT 3.0
Propellant	-	Xe	Xe	Xe	Xe	Xe
Thrust	(mN)	4-17	5.6-13	1.8	2.5-12	3-6
Specific Impulse	(s)	1200-1600	576-1370	865	-	1100-1650
Power	(W)	100-300	99-258	126	50-300	90-185
Electrical Efficiency	(%)	20-45	16-34	6	15-32	20-27
Diameter	(cm)	2.1	3	0.4	2.6	3
Mass	(g)	<1	~1	-	-	-

However, Hall thrusters are heavier due to their magnet mass, which increases the total mass of the propulsion system [15].

### Colloidal and field emission electric propulsion (FEEP) thrusters

Colloidal thrusters are a type of electrostatic thruster that does not require a plasma discharge eliminating the efficiency losses associated with the miniaturization of the plasma chamber found in ion engine and hall thruster designs. Colloidal thrusters emit ions or charged droplets directly from a liquid propellant column when a strong electrostatic field is applied, dry powder propellants have also been used [16].

In an electrospray thruster, the propellant is injected through an emitter. The emitter can be either a sharp needle, a capillary, or a narrow slit. An electric field is applied between the emitter and an opposing electrode. The sharp emitter tip causes the field to intensify. Due to the balance of surface tension and electrostatic forces at the tip of the emitter, the conductive propellant is distorted into a sharp Taylor cone whose shape intensifies the electric field strength even further [15]. Depending on the choice of propellant either ions or charged liquid droplets are emitted. Thrusters that work with liquid metal propellants and emit ions are typically referred to as Field Emission Electric Propulsion (FEEP) [15]. Thrusters that use primarily droplet

emissions, typically working with glycerol or ionic liquid propellants, are referred to as colloidal thrusters [15]. It is important to note that the difference between these two thruster types is not well defined in the case of the thrusters using ionic liquid, molten salts at room temperature since they can emit either ions or droplets depending on the operating conditions [15].

Figure 2-11(A, B) shows the ST-7/LISA colloid propulsion system consisting of four heads per cluster and nine individually machined emitters per head [15], [34].



Figure 2-11. Colloid thruster. A) Individual ST-7 colloid thruster emitter, actual thruster is composed of multiple emitters, and B) cluster head (4 per cluster) [15], [34].

The following table shows the operational parameters of the ST-7 colloid thruster [15], [35].

Table 2-4. ST-7 colloid thruster cluster performance characteristics [15], [35].

Parameter	Units	Demonstrated Performance
Thrust	( $\mu\text{N}$ )	5 - 35.8
Thrust Noise	( $\mu\text{N}$ )	< 0.01
Specific Impulse	(s)	240
Max Power	(W)	24.6 (2 W per head)
Nominal Power	(W)	16
Beam Divergence (1/2 angle)	(degree)	<23
Mass	(kg)	15

The ST-7 colloid thruster cluster is too large for CubeSat applications, but each thruster head could form a stand-alone thruster. The biggest miniaturization challenge of colloid

propulsion systems is not the thruster head itself, but the required miniaturization of the dedicated feed and power processing unit (PPU) subsystems.

The FEEP-5 created by the University of Pisa and Centrosazio is shown in the following figure, which is a field emission electric propulsion thruster design [15].



Figure 2-12. FEEP-5 thruster by Centrosazio/Alta [15].

One of the main differences between colloid and FEEP thrusters, besides the latter emitting predominantly ions instead of charged liquid droplets, is that FEEP thrusters are not pressure fed [15]. Capillary forces supply the propellant to the emitter, simplifying the design of the thruster by not requiring valves or propellant tanks. The following table shows the performance parameters of several FEEP thrusters [15].

Table 2-5. FEEP Performance Characteristics [15].

Parameter	Units	In-FEEP 100	GOCE MTA	In-FEEP 1000	FEEP- 5	FEEP- 50
Thrust	(mN)	0.001-0.1	0.002-0.65	0.001-1	0.04	1.4
$I_{sp}$	( $10^3$ s)	8-12	8-12	8-12	9	9
Power	(W)	0.5-10	6-52	2-80	2.7	93
PPU Mass	(kg)	Incl.	Incl.	Incl.	1	1.2
Mass	(kg)	0.3	3.5	1.5	0.6	1.2

FEEP thrusters allow for extremely high specific impulse values, however, at reduced thrust-to-power ratios, requiring either long transfer times or high power levels

[15]. Cesium, the most common propellant used, is very corrosive and may clog emitter slits. A more suitable propellant is indium, requiring heater power to liquefy it.

### Electromagnetic Thrusters

Electromagnetic thrusters accelerate the flow utilizing electrical current and magnetic fields. They accelerate the ionized propellant using the Lorentz force or they accelerate the ionized propellant by the effect of an electromagnetic field where the electric field is not in the direction of the acceleration.

**Pulse plasma thrusters (PPTs):** In a PPT, a capacitor connected to two electrodes is charged and discharged [15]. The arc produced between the two electrodes by the capacitor discharge ablates the solid Teflon used as a fuel rod. The ablated material accelerates due to the Lorentz force produced by the current flowing through it and its interaction with the self-induced magnetic field. The following figure shows the Micro Liquid Pulsed Plasma Thruster (MILIPULT), containing a small liquid reservoir that allows a flow to creep between the electrodes [8], [15], [36].

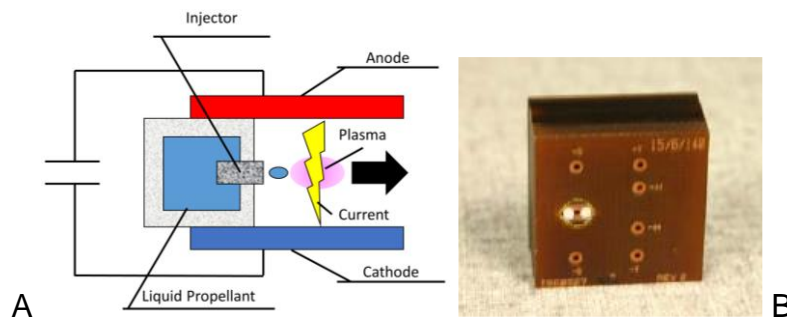


Figure 2-13. PPT thruster. A) Schematic of a liquid propellant PPT [8], and B) APL MILIPULT liquid micro-PPT [15], [36].

PPTs offer very small impulse bits, solid propellant storage in the form of Teflon fuel rods, modularity, and proven operation. The following table shows the performance of different designs [15].

Table 2-6. Micro-PPT Performances [15].

Parameter	Units	Dawgstar	AFRL μPPT	ARCS μPPT	MILIPULT
Propellant	-	Teflon	Teflon	Teflon	Water
Impulse bit	(μN-s)	60	2	2-25	0.4-0.6
Thrust	(μN)	61-264	-	-	-
Specific Impulse	(s)	266	-	-	-
Mass	(g)	4200	500	30 (5 g prop.)	13.5
Power	(W)	15.6-36	1-20	0.5-4	
Capacitance	(μF)	1.3 (per module)	0.42	2-6	0.937
Voltage	(kV)	2.8	2.45- 5.36	-	0.2-0.7
Efficiency	(%)	1.8	-	-	-

The power electronics and storage capacitors account for 40 - 45% of the thruster's system mass [15]. Miniaturization of PPT technology should focus on reducing the mass of the thruster head as well as supporting power electronics. The thruster itself faces challenges during miniaturization for small satellite applications. For example, if the discharge energy, because of overall system miniaturization, is too small then the carbon neutrals in the plasma arc can return to the fuel rod surface and result in charring which can cause shorting of the thruster electrodes.

### **Conclusion of Micro-propulsion Technologies Survey**

The above survey was presented in order to provide some documentation on the existing competing technologies and to depict the strengths and weaknesses of each design. Due to the vast number of micro-propulsion technologies under investigation, only some of the existing designs are presented here and only a few of these designs have actually been commissioned and successfully flown as part of the propulsion system of small satellites [8]. Many of these technologies available cause concerns

related to their reliability, weight, power requirements, and propellant dispensation, or thrust resolution and repeatability [8]. The goal of the Rarefied Gas Electro Jet (RGEJ) thruster presented in this dissertation is to improve cold gas thruster technologies and provide a viable alternative propulsion system for small satellites.

## CHAPTER 3 GAS DISCHARGE PHYSICS

Some basic plasma physics concepts are explained in this chapter in order to understand the physics used to model numerically the RGEJ thruster. Plasma refers to a system of charged particles, which demonstrate collective behavior [37]. Irwin Langmuir chose the term “plasma” due to its similarity with blood plasma, which is composed of two kinds of ‘particle’: the red and white blood cells, similar to positive ions and electrons in a plasma [38]. In the real world, plasmas are composed of more than two particles. They may also contain negative ions as well as metastable atoms or molecules. The plasma state is known as the fourth state of matter due to its unique properties that separate it from solids, liquids, and neutral gases. The charged particles that plasma contains make it electrically conductive, allowing it to interact with external electromagnetic fields and to produce its own electromagnetic fields due to space charge effects and charge-carrier currents [39], [40], [41]. It is estimated that 99% of the matter in the entire visible universe is plasma, making it the most prevalent observable state of matter.

In a laboratory, plasma is typically produced by the coupling of electromagnetic energy into a neutral gas through a discharge [42], [43]. There are many types of discharges at low pressure such as glow discharges, capacitively coupled plasma (CCP) discharges, inductively coupled plasma (ICP) discharges, etc. [11].

Glow discharges use a Direct-Current (DC) or a low-frequency Radio Frequency (RF) electric field (<100 kHz) applied to a gap between electrodes. Capacitively coupled plasma (CCP) discharges use high-frequency RF electric fields (~10 MHz). Inductively

coupled plasma (ICP) discharges are similar to CCP with the difference that electrodes consist of a coil wrapped around the plasma chamber.

In this study, DC glow discharges are of particular interest. Glow discharges are generated due to an electrical breakdown of gases by an externally applied potential [43]. The mechanism of electrical breakdown of gases is best described in terms of voltage-current characteristics of the discharge [8], which is explained further in the following section.

### **Electrical Breakdown of Gases**

Plasmas are generated when electrons are ejected from neutral atoms when energetic photons, or free electrons with sufficient energy, collide with the neutral atoms (or molecules) generating ions and more free electrons [8]. This effect could be achieved in the laboratory by applying an external electric potential to a gas [43]. The mechanism of electric breakdown can be better understood by considering what happens to the current flowing through a low-pressure gas (1-10 Torr) contained in a sealed glass tube with electrodes at either end as the voltage across the electrodes is gradually increased [41]. [Figure 3-1](#) shows the voltage-current characteristics of a DC gas discharge in a cold cathode tube [44]. The discharge has three main regions: *dark discharge*, *glow discharge*, and *arc discharge*. The voltage-current characteristics plot of a DC gas discharge is nonlinear and it depends on the geometry of the electrodes, the gas used, the pressure, and the electrode material.

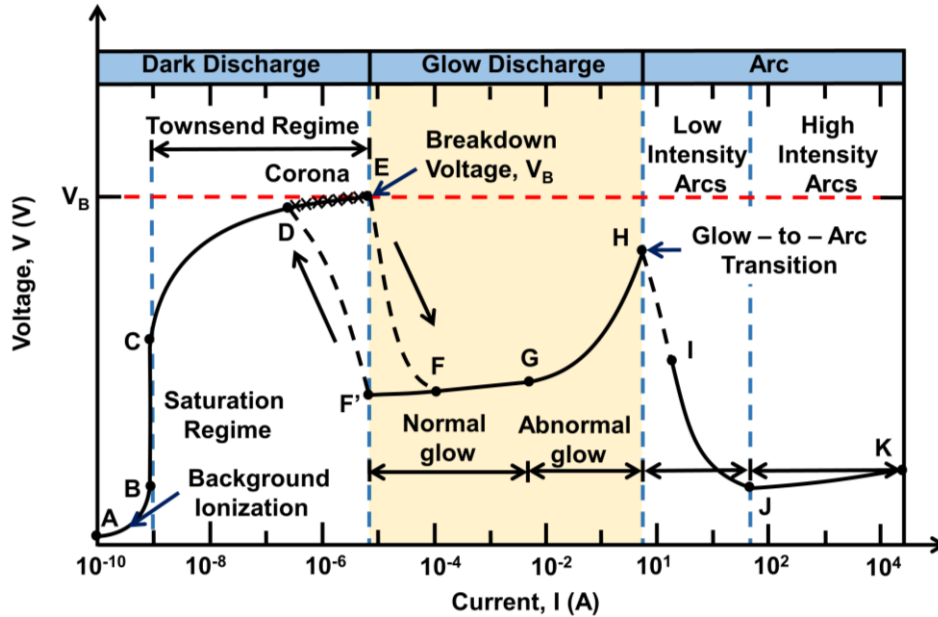


Figure 3-1. Voltage-Current Characteristics of a DC gas discharge [44].

### Dark Discharge

In the dark-discharge region, the regime between A and E in Figure 3-1, the discharge remains invisible to the human eye except for corona discharges and the breakdown itself. In this regime, the current is less than  $10^{-5}$  A [43]. The dark discharge is subdivided into three distinct sub-regions: the background ionization stage, the saturation regime, and the Townsend regime.

In the A-B sub-region, called the background ionization stage, the background radiation generated by cosmic rays and other sources causes a constant degree of ionization of the neutral particles in the gas. The applied electric field sweeps out the ions and electrons produced by the ionization process. Increasing the voltage between electrodes causes an increasing fraction of these charged particles to be sweep toward the electrodes producing a weak electric current.

In the B-C sub-region, called the saturation region, the current remains constant with increasing voltage. The voltage between electrodes is high enough at point B to

sweep all available electrons and ions away. The current in this region depends linearly on the background-radiation source strength and reaches a saturation point at point B. The electric field is too weak to provide enough energy for electrons produced by the background-radiation to ionize other neutral particles.

In the C-E sub-region, known as the Townsend discharge, as the voltage is increased the current profile is characterized by an exponential increase. The electrons present in the gas are now able to gain enough energy from the electric field to ionize the neutral particles. As the voltage is further increased, the secondary electrons produce during ionization are more likely to become part of the ionization process along with the electrons produced by background radiation leading to an avalanche of electron and ion production. The D-E sub-region, the corona discharge, is part of the Townsend discharge regime and occurs in areas of high electric field near sharp points, edges, or wires preceding to electric breakdown (at point E). If the current is high enough, corona discharges can become visible to the human eye, emitting light in the UV spectral region and the visible blue spectral region, but for low currents, they are dark discharges.

At point E, electrical breakdown occurs in the Townsend regime due to the production of secondary electrons generated by ion or photon impacts on the cathode electrode. At point E, when the voltage reaches the sparking potential ( $V_B$ ), the current increases by a factor of  $10^4$  to  $10^8$ . Only the internal resistance of the power supply limits the current. When the discharge tube cannot draw enough current to break down the gas, due to high internal resistance, the discharge remains in the corona regime. Otherwise, the discharge transitions into the normal glow regime due to electron

avalanche processes. The pressure-distance (pd) product and the secondary electron coefficient of the electrode material ( $\gamma_{sec}$ ) determine the breakdown voltage ( $V_B$ ) for a particular gas as described by the Paschen's law [41].

### Glow Discharge

In the glow-discharge region, the electron energy and electron number density are high enough for excitation collisions to generate visible light causing the plasma to be luminous. In this regime, the current is usually between  $10^{-5}$  A and 1 A for a typical laboratory cold cathode tube. The transition between point E and F is discontinuous.

In the F-G sub-region, called the normal glow regime, the voltage is almost independent of the current and the electrode current density is independent of the total current because at low currents the plasma is in contact with only a small area of the cathode. As the current increases, the cathode area in contact with the plasma increases, until point G is reached and the entire cathode area is in contact with the plasma. The transition from normal to abnormal glow discharge happens between current values of  $10^{-3}$  to  $10^{-2}$  A.

In sub-region G-H, called the abnormal glow regime, the plasma covers all the cathode area, a higher current is only achievable by having a higher current density. The voltage increases significantly with the increasing current. The abnormal glow regime discharge is brighter than the normal glow regime, and the structures of the discharge near the cathode can blend into one another, forming a uniform glow.

A form of hysteresis, a time-based dependence of a system's output on current and past inputs, is observed in the voltage-current characteristics when moving to the

left of point G. The discharge reaches a lower current value and current density than at point F, making a discontinuous transition back to the Townsend regime at point F'.

### Arc Discharge

In the H-K region, the arc discharge region, after point H the cathode becomes hot enough to emit electrons in a process called thermionic emissions. The discharge undergoes glow-to-arc transition, in the H-I regime, when the power supply has low internal resistance at currents of  $\sim 1$  A. In the I-J regime, known as the low-intensity arc, the discharge voltage decreases as the current increases, the arc column is governed by thermal conduction losses [45], and thermionic emission of electrons from the electrodes support the arc. After point J, which is at approximately 20 to 50 A, the voltage increases slowly as the current increases, radiation becomes the dominant loss mechanism yielding the positive gradient characteristic [45].

### **Qualitative Characteristics of DC Glow Discharge**

DC glow discharges produce weakly ionized (low degree of ionization,  $10^{-8}$  -  $10^{-4}$ ), non-thermal plasmas. Laboratory plasmas are usually categorized as either “thermal” or “non-thermal” plasmas. In a thermal plasma, the particles (ions, electrons, neutrals, others) are in thermodynamic equilibrium and are characterized by a single temperature. In a non-thermal plasma, the electron temperature is much higher ( $\sim 10,000$  K to  $\sim 100,000$  K) than the temperature of the heavy particles which is roughly the same as the room temperature [11].

The degree of ionization refers to the proportion of neutral particles that are ionized into charged particles and it is defined as,

$$I_{\text{deg}} = \frac{n_i}{n_i + n_n}, \quad (3-1)$$

where  $n_i$  and  $n_n$  represent ion and neutral number densities, respectively [8]. The degree of ionization for DC glow discharges are in the range of  $10^{-8} - 10^{-4}$ . Due to the low degree of ionization, recombination is of minor importance and most of the charged particles are lost (neutralized) by transport to the solid surfaces.

The usual pressure range of operation is between 10 mTorr and 10 Torr and typically, only a few hundreds of volts between cathode and anode is required to maintain the discharge [41]. In a laboratory discharge, the cathode is an electrical conductor, usually a metal, with a secondary emission coefficient; it emits electrons when bombarded by incoming positive ions.

The behavior of a DC glow discharge can be quite complicated, with many light and dark regions. Figure 3-2 shows the qualitative characteristics of DC glow discharge in a glass tube containing low-pressure gas [46].

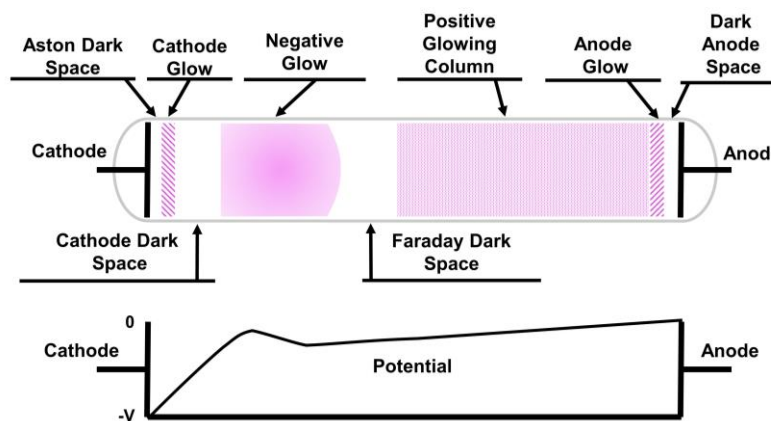


Figure 3-2. Qualitative characteristics of DC glow discharge and electric potential distribution at low pressures (0.1 – 10 Torr) and room temperature [46].

All of the regions are gas, pressure, and voltage-dependent in their size and intensity, with some of the smaller features being essentially absent over various parameter ranges [41].

The Aston dark space is a thin region next to the cathode containing a layer of negative charge and a strong electric field. Electrons are accelerated through this space away from the cathode. The plasma appears dark since the electron density and/or energy is too low to excite the gas. In this region, the combined electrons number density of stray initial electrons and secondary electrons from the cathode outnumber the ion number density causing the negative charge.

In the cathode glow, the electrons are energetic enough to excite the neutral atoms, resulting in the luminous cathode glow. This region has relatively high ion density and sometimes masks the Aston dark space by clinging to the cathode. Its axial length depends on the carrier gas, the pressure, and temperature.

Cathode dark space (Crooks dark space) is a positive-space-charge layer that has a moderately strong electric field and a relatively high ion density [47]. Its axial length depends on the pressure and the applied voltage. In this region, electrons are accelerated by the strong electric field from the cathode to the anode, while the positive ions are accelerated in the opposite direction. These accelerated ions cause the pulverization of the cathode material and the emission of secondary electrons. The secondary electrons accelerate and cause the creation of new ions through collision with neutral atoms. The majority of the potential drop happens in this region [41]. Therefore, the cathode dark space is also called “cathode fall”. From the end of the

cathode dark space to the anode, the plasma experiences only low values of electric fields [47].

The negative glow region has the brightest intensity in the whole discharge. Electrons that have been accelerated in the cathode region to high speeds produce ionization, while slower electrons that have had experienced inelastic collisions produce excitations [41]. The slower electrons are responsible for the glow, although other processes also play a role [47]. In this region, the electrons predominantly carry the current due to their higher mobility. At the end of this region, the electric field must decrease rapidly and the electrons slow down by elastic and inelastic collisions. The electric field can reverse in this region to keep the electron current balance [41]. The field reversal excludes ions from a region of the column; this region of low ion density prevents the negative glow from joining directly onto the positive column [41].

In the Faraday dark space, a transition region between the negative glow and the positive column, the electrons do not have enough energy to produce excitations, therefore, no glow is observed [41]. In this region, the electrons begin to feel the effects of the positive anode potential and are accelerated toward it, although there is only a relatively low field strength [47].

The positive column is typically the physically largest component of a normal discharge. If the discharge tube is increased at constant pressure, the cathode structures remain the same size, but the positive column lengthens. In this region, the plasma is quasi-neutral and the electric field is weak. Usually, the positive column is a long, uniform glow mode discharge, except when standing or moving striations (traveling or stationary perturbations in the electron number density), or other

instabilities are triggered by disturbance [43]. Striations occur due to electron absorption during ionization and the formation of slow secondary electrons that require acceleration before they can cause ionization.

The Anode glow is usually brighter than the positive column, and it is not always present. It is the boundary of the anode sheath.

The Anode dark space (anode sheath), is a single layer of negative space net charge density that separates the anode glow from the anode itself. This region has stronger electric field than the positive column.

Figure 3-2 shows the typical potential and light distribution when the distance between electrodes is large in comparison to the size of the electrodes. If the electrodes are brought closer together, the positive column shrinks and eventually is completely eliminated. In this case, the anode is in contact with the Faraday dark space and the anode is at equipotential with the bulk plasma. If the distance between electrodes is further decreased, the Faraday dark space also disappears and the anode is in contact with the negative glow, which is called *obstructed glow* [48]. In this case, the negative glow region has the most positive potential and the anode zone has a negative potential fall that repels electrons and attracts positive ions [48]. The *obstructed glow* is the most common mode of operation for plasma processing used in industry [48].

In the previous discussion, the typical characteristics in the normal glow mode have been considered, which usually occurs between the range of current densities of  $10^{-5}$  to  $10^{-3}$  A/cm<sup>2</sup> [41]. The abnormal glow discharge appears very similar to the normal glow discharge with the exception of being more intensely luminous, as the normal glow transitions to abnormal glow, the cathode voltage drop increases rapidly, and the

cathode dark space shrinks. Sometimes, the structures near the cathode blend into one another, providing a uniform glow.

For further information about the electric breakdown of gases and the qualitative characteristics of DC glow discharges, consult Conrads & Schmidt [49], Fridman [50], Howatson [51], Raizer [43] and Madou [48].

### **Paschen's law**

Previously, the Paschen's Law was described as the equation determining the breakdown voltage of a given gas. The Paschen's Law was introduced by Friedrich Paschen to predict the breakdown voltage ( $V_B$ ), the voltage necessary to start a discharge, between two electrodes in a gas as a function of the pressure and the gap length ( $pd$ ). The formula that describes the breakdown voltage is defined as [41]

$$V_B = \frac{Bpd}{\ln(Apd) - \ln\left(\ln\left(1 + \frac{1}{\gamma_{\text{sec}}}\right)\right)}. \quad (3-2)$$

For large values of ( $pd$ ),  $V_B$  increases essentially linearly with ( $pd$ ). There is a limiting value of ( $pd$ ) below which breakdown cannot occur according to

$$(pd)_{\text{Limit}} = A^{-1} \ln\left(1 + \frac{1}{\gamma_{\text{sec}}}\right). \quad (3-3)$$

The breakdown voltage is a minimum ( $V_{\text{min}}$ ) at some intermediate value of ( $pd$ )

$$(pd)_{\text{Vmin}} = \frac{2.71828}{A} \ln\left(1 + \frac{1}{\gamma_{\text{sec}}}\right), \quad (3-4)$$

$$V_{\text{min}} = 2.71828 \frac{B}{A} \ln\left(1 + \frac{1}{\gamma_{\text{sec}}}\right). \quad (3-5)$$

The breakdown voltage curve is called the Paschen curve, and it is a function of the gas and weakly a function of the electrode material [41]. The following table shows the values of A and B coefficients for several gases obtained from page 546 in Lieberman and Lichtenberg [41].

Table 3-1. Breakdown voltage constants A and B [41].

Gas	A ( $\text{cm}^{-1}\text{Torr}^{-1}$ )	B ( $\text{Vcm}^{-1}\text{Torr}^{-1}$ )	Range of E/p ( $\text{Vcm}^{-1}\text{Torr}^{-1}$ )
He	2.8	77	30-250
Ne	4.4	111	100-400
Ar	11.5	176	100-600
Kr	15.6	220	100-1000
Xe	24	330	200-800
H <sub>2</sub>	4.8	136	15-600
N <sub>2</sub>	11.8	325	100-600
O <sub>2</sub>	6.5	190	50-130
CH <sub>4</sub>	17	300	150-1000
CF <sub>4</sub>	11	213	25-200

For argon, the following table gives the  $V_{min}$  values and the values of  $(pd)$  at which  $V_{min}$  occurs for several secondary electron emission coefficients ( $\gamma_{sec}$ ) as well as the value of  $(pd)_{Limit}$  below which the Paschen curve can no longer predict the breakdown voltage.

Table 3-2. Limit of  $(pd)$  and minimum breakdown voltage values for argon.

$(\gamma_{sec})$	$(pd)_{Limit}$ (Torr-cm)	$(pd)_{Vmin}$ (Torr-cm)	$V_{min}$ (V)
0.01	0.401	1.091	192.0
0.05	0.265	0.720	126.7
0.07	0.237	0.645	113.4

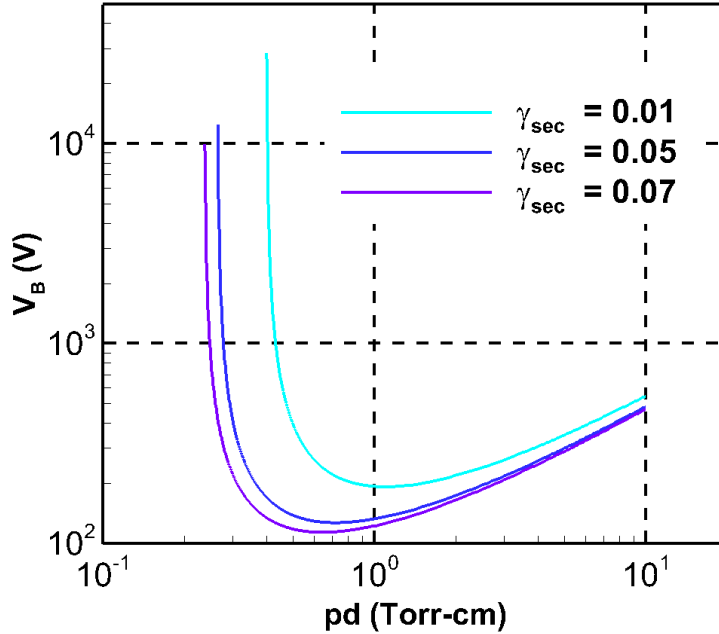


Figure 3-3. Paschen curves for argon at different values of  $\gamma_{sec}$ .

As observed in [Figure 3-3](#), the breakdown voltage depends strongly on the strength of the applied electric field, increasing with increasing electrode spacing for  $(pd)$  values higher than  $(pd)_{Vmin}$ . For  $(pd)$  values lower than  $(pd)_{Vmin}$ , the breakdown voltage increases with decreasing electrode gap due to a decrease in the probability of collisions between electrons and atoms. For the cases shown in this study, the distance between electrodes is chosen in order to satisfy  $(pd)_{Vmin}$  at the given inlet pressures and the initial voltage of each numerical simulation is chosen higher than  $V_{min}$ .

### Sputtering

At energies above a threshold of  $\epsilon_{thr} = 20 - 50$  eV [41], heavy particles can sputter atoms from a surface. The sputtering yield ( $\gamma_{sput}$ ) represents the number of atoms sputtered per incident ion. Sputtering can cause erosion of electrodes, which eventually can damage a thruster. In an argon glow discharge, operating at 1.0 Torr and

~950 V voltage difference, the average ion bombardment energy is ~60 eV, which produces a primary sputter yield of ( $\gamma_{\text{sput}} = 0.1$ ) for copper electrodes [52].

The sputtering rate,  $R_{\text{sput}}$ , can be calculated from the following equation [41],

$$R_{\text{sput}} = \gamma_{\text{sput}} \frac{\bar{J}_i}{en_{\text{Target}}} \quad (\text{cm/ s}), \quad (3-6)$$

where  $\bar{J}_i$  is the ion current density in ( $\text{A/cm}^2$ ), and  $n_{\text{Target}}$  is the number density of the target material in ( $\text{cm}^{-3}$ ). For example, the number density of Cu is equal to  $8.49 \times 10^{22} \text{ cm}^{-3}$  and the primary sputter yield is equal to 0.1. For an ion current density of  $5.0 \times 10^{-3} \text{ (A/cm}^2)$ , the peak value of the ion current density for *Case 750V* in this study, the  $R_{\text{sput}}$  is approximated as  $3.68 \times 10^{-8} \text{ cm/s}$ . For copper electrodes, the cathode region experiencing peak ion current density will be eroded 1 mm every 755 hours of continuous thruster operation. Thus, the cathode must be replaced when the erosion track becomes comparable to the cathode thickness or the thruster will be impaired. The erosion rate can be decreased by using more suited materials with lower sputtering yield such as tungsten.

## CHAPTER 4 GOVERNING EQUATIONS

In order to simulate the RGEJ, two different numerical models are used: an ionized gas model, which uses a hydrodynamic plasma model called the Local Mean Energy Approximation (LMEA) to simulate the plasma (charged and excited particles), and a rarefied gas model to simulate the gas itself (the aggregate of all particles as a single mixture).

The ionized gas model is used to calculate the volumetric plasma-induced electrostatic force components ( $F_x, F_y$ ) and the volumetric electro-thermal heating source ( $q'''$ ) needed by the rarefied gas model. The rarefied gas model is used to calculate the gas density ( $\rho$ ), components of velocity ( $u, v$ ), and temperature ( $T$ ) needed by the ionized gas model. In this chapter, an overview of the governing equations, boundary conditions, and equations used to obtain  $F_x, F_y$ , and  $q'''$ .

### **Hydrodynamic Plasma Model**

#### **Boltzmann Equation**

Since a plasma is an assembly of a great number of moving and interacting particles, plasma problems can be solved by methods of physical kinetics [53]. The distribution function is the main statistical characteristic of an assembly and to find it the whole configuration space and the entire range of particle velocities must be divided into small intervals such that the particle density variation within each interval could be neglected. The distribution function ( $F$ ) can be represented as the product of the density of the particles in the configuration space ( $n$ ) and the velocity distribution function ( $f$ ) as described by Golant et al. [53].

The equation describing the time evolution of the velocity distribution function ( $f$ ) for a particle species ( $j$ ) is known as the kinetic (or Boltzmann) equation [53], [54]

$$\frac{\partial (nf)_j}{\partial t} + \mathbf{v}_j \cdot \nabla (nf)_j + \frac{Z_j e}{m_j} [\mathbf{E} + \mathbf{v}_j \times \mathbf{B}] \cdot \nabla_v (nf)_j = \frac{\delta (nf)_j}{\delta t}. \quad (4-1)$$

The vector  $\mathbf{x}$  describes the spatial coordinates,  $\mathbf{v}$  describes the velocity coordinates,  $t$  is the time,  $\mathbf{E}$  and  $\mathbf{B}$  are the electric and magnetic fields, and  $n_j$  is the number density [54].  $Z_j$  represents the ionizity (or valence) of the charged particles and  $m_j$  is the species mass. The sign of  $Z_j$  denotes the polarity of the charge. The R.H.S. term represents the rate of change in distribution function due to the particle collisions [53]. Since the different collisions occur independently of each other, the rate of change in distribution function because of various types of collision can be summed. For  $\alpha$ -type particles

$$\frac{\delta (nf)_\alpha}{\delta t} = \sum_\beta \sum_p S_{\alpha\beta}^p (nf)_\alpha, \quad (4-2)$$

where the summation is extended to all species of  $\beta$ -type particles and all types of  $p$  collisions. Since  $f_j(\mathbf{x}, \mathbf{v}_j, t)$  varies in up to six dimensions (3-D and 3-V) and time, solving this equation along with the additional coupled governing equations of electric and magnetic fields is computationally prohibited [54]. To reduce the high dimensionality, the velocity distribution function is projected and integrated in velocity space. The necessary normalization condition is [53]

$$\int_{(v)} f_j(\mathbf{x}, \mathbf{v}_j, t) d^3 v_j = 1. \quad (4-3)$$

The distribution function makes it possible to average out any value over the particle distribution. The average value of a quantity in velocity space can be defined as follows (using velocity as an example) [53], [54]

$$\mathbf{u}_j(\mathbf{x}, t) = \langle \mathbf{v}_j \rangle = \int_{(v)} \mathbf{v}_j f_j(\mathbf{x}, \mathbf{v}_j, t) d^3 v_j. \quad (4-4)$$

These two equations, previously shown, are used to integrate the Boltzmann equation and allow more realistic fluid and plasma problems to be solved.

### **Distribution Function Moments Equation**

In order to obtain the general form of the moments equation, the Boltzmann equation is multiplied by some combination of the velocity projections, denoted by  $g$ , corresponding to a certain time instant, and then each term in the equation is integrated over the entire velocity space [53]. The distribution function moment corresponding to this combination is

$$\langle g \rangle = \int_{(v)} g f(\mathbf{v}) d^3 v. \quad (4-5)$$

After (4-1) is multiplied by  $g$  and integrated over the velocity space, the first term in the equation is

$$\int_{(v)} g \frac{\partial (nf)}{\partial t} d^3 v = \frac{\partial}{\partial t} \left( n \int_{(v)} g f d^3 v \right) = \frac{\partial n \langle g \rangle}{\partial t}. \quad (4-6)$$

The order of integration and differentiation can be reversed since time  $t$  and velocity components  $\mathbf{v}$  are independent variables. The coordinates in configuration space  $\mathbf{x}$  is also independent of  $\mathbf{v}$ , therefore the second term is transformed as

$$\begin{aligned} \int_{(v)} g[\mathbf{v} \cdot \nabla(nf)] d^3v &= \sum_k \int_{(v)} g v_k \frac{\partial(nf)}{\partial x_k} d^3v \\ &= \sum_k \frac{\partial}{\partial x_k} \left[ n \int_{(v)} g v_k f d^3v \right] = \nabla \cdot (n \langle \mathbf{v}g \rangle), \end{aligned} \quad (4-7)$$

where  $k$  is the number of components of  $\mathbf{v}$ .

The third term, which is related to the Lorenz force, can be separated into two parts: the one proportional to the electric field and the other one proportional to the magnetic field. Using integration by parts and taking into account that the distribution function must vanish as  $v_k \rightarrow \pm\infty$ , each part becomes

$$\begin{aligned} \int_{(v)} g \frac{Ze}{m} \mathbf{E} \cdot \nabla_v(nf) d^3v &= \frac{Zen}{m} \int_{(v)} g \sum_k E_k \frac{\partial f}{\partial v_k} d^3v \\ &= -\frac{Zen}{m} \sum_k E_k \int_{(v)} \frac{\partial g}{\partial v_k} f d^3v = -\frac{Ze}{m} n \mathbf{E} \cdot \langle \nabla_v(g) \rangle, \end{aligned} \quad (4-8)$$

$$\begin{aligned} \int_{(v)} g \frac{Ze}{m} \{[\mathbf{v} \times \mathbf{B}] \cdot \nabla_v(nf)\} d^3v &= \frac{Zen}{m} \sum_k \int_{(v)} [\mathbf{v} \times \mathbf{B}]_k \frac{\partial f}{\partial v_k} g d^3v \\ &= -\frac{Zen}{m} \sum_k \int_{(v)} \left\{ [\mathbf{v} \times \mathbf{B}]_k \frac{\partial g}{\partial v_k} + g \frac{\partial [\mathbf{v} \times \mathbf{B}]_k}{\partial v_k} \right\} f d^3v \\ &= -\frac{Zen}{m} \sum_k \int_{(v)} [\mathbf{v} \times \mathbf{B}]_k \frac{\partial g}{\partial v_k} f d^3v = -\frac{Zen}{m} \sum_k \left\langle [\mathbf{v} \times \mathbf{B}]_k \frac{\partial g}{\partial v_k} \right\rangle \\ &= -\frac{Zen}{m} \langle [\mathbf{v} \times \mathbf{B}] \cdot \nabla_v g \rangle. \end{aligned} \quad (4-9)$$

In (4-9), the term  $\partial[\mathbf{v} \times \mathbf{B}]_k / \partial v_k$  is equal to zero since  $[\mathbf{v} \times \mathbf{B}]_k$  depends only on the velocity component perpendicular to  $v_k$ . The final term is obtained by integrating the collision term,

$$\int_{(v)} \frac{\delta(nf)}{\delta t} g d^3v = \frac{\delta n \langle g \rangle}{\delta t}. \quad (4-10)$$

The general form of the moments equations is [53]

$$\frac{\partial n \langle g \rangle}{\partial t} + \nabla \cdot (n \langle g \mathbf{v} \rangle) - \frac{Zen}{m} \mathbf{E} \cdot \langle \nabla_v (g) \rangle - \frac{Zen}{m} \langle [\mathbf{v} \times \mathbf{B}] \cdot \nabla_v g \rangle = \frac{\delta n \langle g \rangle}{\delta t}. \quad (4-11)$$

Using (4-11) the zero-moment equation, defined as the equation for the concentration (density), can be derived by setting  $g$  equal to 1, the first-moment equation is derived by setting  $g$  equal to  $v_k$ , in the second-moment equation  $g$  equals  $v_k v_l$  and so on.

### Continuity Equation

As previously explained, the zeroth-moment (or continuity) equation is obtained by setting  $g = 1$ , which makes the average of the quantities contained in (4-11) equal to [53]

$$\begin{aligned} \langle g \rangle &= 1, \\ \langle g v_k \rangle &= \langle v_k \rangle = u_k, \\ \langle \nabla_v (g) \rangle &= 0, \\ \frac{\delta n \langle g \rangle}{\delta t} &= \frac{\delta n}{\delta t} = S. \end{aligned} \quad (4-12)$$

The term  $S$  represents the chemical reactions (gains and losses of particles due to collisions) [54]. To evaluate the collision integral, some assumptions about the velocity

distribution function are necessary such as its deviation is small, which allows the Boltzmann equation to be solved by the method of successive approximations. In this case, the distribution function is represented as a series in the powers of the parameters ( $f = f_{(0)} + f_{(1)} + f_{(2)} + \dots$ ) determining its deviation from equilibrium (forces affecting the particles and the concentration and temperature gradients) [53]. The first term of the series ( $f_{(0)}$ ) is the equilibrium (Maxwellian) distribution, the second term ( $f_{(1)}$ ) includes a linear combination of the parameters, the second term ( $f_{(2)}$ ) a quadratic combination, and so on. If a homogeneous electric field  $\mathbf{E}$  is the source of disequilibrium, the field determines the only isolated direction, therefore it is assumed that the Oz axis is parallel to it. This means that  $f$  may depend only on the velocity  $v$  and on the angle  $\theta$  due to anisotropy, the angle between the directions  $v$  and  $\mathbf{E}$ . The distribution function is expanded using a series, typically the orthogonal Legendre polynomials

$$f(\mathbf{v}) = \sum_{n=0}^{\infty} f_n(v) P_n(\cos \theta). \quad (4-13)$$

The function  $f_n$  depends only on the velocity. The Boltzmann solver BOLSIG+, used to calculate the reaction rates in this study, uses a two-term expansion

$$f(\mathbf{v}) = f_{(0)}(v) + \cos(\theta) f_{(1)}(v) = f_{(0)}(v) + \frac{v_z}{v} f_{(1)}(v) \quad (4-14)$$

The final zeroth-moment (or continuity) equation for a species ( $j$ ) is

$$\frac{\partial n_j}{\partial t} + \nabla \cdot (n_j \mathbf{u}_j) = S_j. \quad (4-15)$$

The species velocity  $\mathbf{u}_j$ , introduced as an unknown, is solved using the first-moment equation.

### Momentum Equation

The first-moment (or momentum) equation is obtained by setting  $g = v_k$ , which makes the average of the quantities contained in (4-11) equal to [53]

$$\begin{aligned} \langle g \rangle &= \langle v_k \rangle = u_k, \\ \langle g v_l \rangle &= \langle v_k v_l \rangle = \frac{P_{kl}}{nm} = u_k u_l + \frac{p}{nm} \delta_{kl} + \frac{\pi_{kl}}{nm}, \\ \langle \nabla_v(g) \rangle &= \langle \nabla_v(v_k) \rangle = \hat{k}, \\ \frac{\delta n \langle g \rangle}{\delta t} &= \frac{\delta n \langle v_k \rangle}{\delta t} = \frac{\delta n u_k}{\delta t}. \end{aligned} \quad (4-16)$$

In (4-16),  $\hat{k}$  is a unit vector in the direction of the k-axis, while the set of  $P_{kl}$  values is the momentum flux density tensor [53]. In the momentum flux density tensor,  $p$  is the normal scalar pressure and  $\pi_{kl} = nm \langle w_k w_l - \frac{1}{3} w^2 \delta_{kl} \rangle$  is the set of values of the viscous stress tensor due to the deviation of the distribution from spherical symmetry, where  $\mathbf{w}$  is the random velocity vector.

After substituting (4-16) in (4-11), the first-moment equation is defined as

$$\frac{\partial(nu_k)}{\partial t} + \sum_l \frac{\partial}{\partial x_l} (nu_k u_l) + \frac{1}{m} \frac{\partial p}{\partial x_k} + \frac{1}{m} \sum_l \frac{\partial \pi_{kl}}{\partial x_l} - \frac{Zen}{m} \{E_k + [\mathbf{u} \times \mathbf{B}]_k\} = \frac{\delta(nu_k)}{\delta t}. \quad (4-17)$$

The first term in (4-17) is expanded and transform with the help of the zeroth-moment equation

$$\frac{\partial(nu_k)}{\partial t} = n \frac{\partial u_k}{\partial t} + u_k \frac{\partial n}{\partial t} = n \frac{\partial u_k}{\partial t} - u_k \sum_l \frac{\partial(nu_l)}{\partial x_l} + u_k \frac{\delta n}{\delta t}, \quad (4-18)$$

while the last term in (4-17) can be decomposed as

$$\frac{\delta(nu_k)}{\delta t} = n \frac{\delta u_k}{\delta t} + u_k \frac{\delta n}{\delta t}. \quad (4-19)$$

Substituting (4-18) and (4-19) into the first-moment equation and finding identical equations for the other two components of the vector  $\mathbf{u}$ , the vector equation for the directed velocity for a species ( $j$ ) is [53]

$$m_j n_j \left[ \frac{\partial \mathbf{u}_j}{\partial t} + \mathbf{u}_j \cdot \nabla \mathbf{u}_j \right] = Z_j e n_j \{ \mathbf{E} + \mathbf{u}_j \times \mathbf{B} \} - \nabla p_j - \nabla \cdot \vec{\pi}_j + m_j n_j \frac{\delta \mathbf{u}_j}{\delta t}. \quad (4-20)$$

In this equation, the viscous effects due to  $\vec{\pi}_j$  can be neglected if the characteristic length scale of the bulk velocity change is much larger than the mean free path, and the random thermal motion is much faster than the bulk fluid velocity [53]. These conditions are satisfied since the velocity distribution function is near Maxwellian (small anisotropy). Furthermore, in the absence of magnetic field, the pressure along all directions can be related to the temperature using the state equation

$$p_j = n_j k_B T_j, \quad (4-21)$$

where  $k_B$  is the Boltzmann constant ( $1.602 \times 10^{-19}$  J/eV) and  $T_j$  is the particle temperature (eV), which requires an additional moment equation to be calculated [54].

In a weakly ionized plasma, the charged-neutral particle collision frequency is much larger than the collision frequency between charged particles [54]. If collisions between charged particles are neglected and the distribution function over the random velocities can be considered isotropic then [53]

$$m_j n_j \frac{\delta \mathbf{u}_j}{\delta t} = -m_j n_j \left( \frac{m_n}{m_j + m_n} \right) \nu_{jn} (\mathbf{u}_j - \mathbf{U}_n), \quad (4-22)$$

where  $(\nu_{jn})$  is the charged-neutral particle collision frequency for a species  $(j)$  and  $U_n$  is the neutral velocity vector (approximated as the bulk gas velocity vector).

### Energy Equation

The second-moment (or energy) equation is obtained by setting  $g = mv^2/2$ , which makes the average of the quantities contained in (4-11) equal to [53]

$$\begin{aligned} \langle g \rangle &= \left\langle \frac{mv^2}{2} \right\rangle = \langle K \rangle, \\ \langle g \mathbf{v} \rangle &= \left\langle \frac{\mathbf{v}mv^2}{2} \right\rangle = \frac{\mathbf{Q}}{n}, \\ \langle \nabla_v (g) \rangle &= \langle m \mathbf{v} \rangle = m \mathbf{u}, \\ \langle ([\mathbf{v} \times \mathbf{B}] \cdot \nabla_v (g)) \rangle &= \langle ([\mathbf{v} \times \mathbf{B}] \cdot m \mathbf{v}) \rangle = 0 \\ \frac{\delta n \langle g \rangle}{\delta t} &= \frac{\delta n \langle K \rangle}{\delta t}. \end{aligned} \quad (4-23)$$

After substituting (4-23) in (4-11), the second-moment equation is obtained as

$$\frac{\partial(n\langle K \rangle)}{\partial t} + \nabla \cdot \mathbf{Q} + Zen(\mathbf{u} \cdot \mathbf{E}) = \frac{\delta n\langle K \rangle}{\delta t}, \quad (4-24)$$

where  $\langle K \rangle$  is the sum of the energies due to random and directed motion and  $\mathbf{Q}$  is the energy flux vector [53]

$$\begin{aligned} \mathbf{Q} &= \mathbf{q} + n\langle K \rangle \mathbf{u} + \vec{\bar{p}} \mathbf{u}, \\ \langle K \rangle &= \frac{mu^2}{2} + \frac{3}{2} k_B T, \\ p_{kl} &= p\delta_{kl} + \pi_{kl} \approx p\delta_{kl}, \\ p &= nk_B T, \end{aligned} \quad (4-25)$$

which depends on the heat flux density vector ( $\mathbf{q}$ ), the pressure tensor ( $\vec{\bar{p}}$ ), and other previously defined variables. The pressure tensor is simplified (the viscous stress tensor is neglected) by assuming that the particle velocity distribution function is near isotropic (small anisotropy) [53].

The heavy ion and metastable atoms species are assumed to be in thermal equilibrium with the neutral gas. The feasibility of this assumption depends on the number of collisions between ions (or metastable atoms) and the neutral particles in a weakly ionized plasma [54]. In the cases shown in this study, the ions rapidly equilibrate with the gas since the ion-neutral mean free path is orders of magnitude smaller than the device length-scale, meaning that many collisions happen between an ion and multiple neutral particles before the ion reaches one of the walls [55].

For the electrons, a simplified energy equation must be solved. This approach is called the Local Mean Energy Approximation (LMEA) [54]. For the electrons, a common approximation is made. The kinetic energy due to random motion is considered much

larger than the kinetic energy due to directed motion, which makes the total kinetic energy  $\langle K_e \rangle$  approximately equal to the mean energy ( $\bar{\varepsilon}$ )

$$\langle K_e \rangle = \frac{m_e u_e^2}{2} + \frac{3}{2} k_B T_e \approx \frac{3}{2} k_B T_e = \bar{\varepsilon}. \quad (4-26)$$

After applying all the assumptions previously explained, the energy flux vector becomes

$$\mathbf{Q}_e = \mathbf{q}_e + \frac{3}{2} n_e k_B T_e \mathbf{u}_e + p_e \mathbf{u} = \mathbf{q}_e + \frac{5}{2} n_e k_B T_e \mathbf{u}_e. \quad (4-27)$$

The second-moment energy equation for electrons is

$$\frac{3}{2} \frac{\partial n_e k_B T_e}{\partial t} + \nabla \cdot \mathbf{q}_e + \frac{5}{2} \nabla \cdot (n_e k_B T_e \mathbf{u}_e) + e n_e (\mathbf{u}_e \cdot \mathbf{E}) = \frac{\delta(n_e \bar{\varepsilon})}{\delta t}. \quad (4-28)$$

In the present model, the fourth moment, known as the electron heat flux ( $\mathbf{q}_e$ ), is approximated using a closure model instead of solving a separate conservation equation, similarly to Houba [54]

$$\mathbf{q}_e = -\frac{2}{3} \kappa_e \nabla(\bar{\varepsilon}) = -\frac{5}{2} D_e n_e \nabla(\bar{\varepsilon}). \quad (4-29)$$

### Drift-Diffusion Approximation

The drift-diffusion approximation is used to drastically reduce the computational cost of a plasma numerical simulation by eliminating the need to solve the full momentum equation separately since the velocity is calculated as a direct function of

the other variables. Several assumptions are necessary for this approximation. As previously mentioned, the viscous terms ( $\sim \bar{\bar{\pi}}_j$ ) are assumed negligible in the momentum equation and the pressure along all directions can be related to the temperature using the state equation ( $p_j = n_j k_B T_j$ ). The second term ( $\mathbf{m}_j \mathbf{u}_j \cdot \nabla \mathbf{u}_j \approx \mathbf{m}_j u_j^2 / L$ ) in the momentum equation (quadratic with respect to  $\mathbf{u}$ ) is neglected since it is much less than the term proportional to the pressure gradient ( $\nabla p_j / n_j \approx p_j / n_j L \approx k_B T_j / L$ ) when the anisotropy of the velocity distribution is small (L is the characteristic length over which the plasma parameters change substantially) [53]. For a weakly ionized gas, this assumption is true for electrons, which are not thermalized with the heavy particles. For ions, which are thermalized with the gas, the term ( $\mathbf{m}_j \mathbf{u}_j \cdot \nabla \mathbf{u}_j \approx \mathbf{m}_j u_j^2 / L$ ) is much smaller than ( $\mathbf{m}_j \mathbf{u}_j v_{jn}$ ).

The first term ( $|m_j \partial \mathbf{u}_j / \partial t| \approx m_j \mathbf{u}_j / \tau \ll m_j \mathbf{u}_j v_{jn}$ ) of the momentum equation (4-20) is considered negligible when the characteristic time of variation in plasma parameter ( $\tau$ ) greatly exceeds the time between collisions [53]. For electrons, due to their very large electron-neutral collision frequency ( $\nu_{en} = e / m_e \mu_e$ ), the first term is typically negligible [43]. If the frequency of the applied electric field is not large in comparison to the ion-neutral collision frequency, the first term of the momentum equation is negligible even for heavier species [56]. For the cases simulated in this study, the applied electric field varies slowly enough in the RF-cases to neglect this term (the ion-neutral collision frequency is about twenty times higher than the applied RF-frequency of 13.56 MHz). In

the absence of magnetic field, taking the previous assumptions, the following momentum equation is obtained,

$$Z_j e n_j \mathbf{E} - \nabla(n k_B T_j) - n_j m_{jn} v_{jn} (\mathbf{u}_j - \mathbf{U}_n) = 0, \quad (4-30)$$

where  $m_{jn} = \frac{m_j m_n}{m_j + m_n}$ .

After (4-30) is divided by the collision frequency and the reduced mass ( $m_{jn}$ ), the species flux is obtained as

$$\Gamma_j = \mathbf{u}_j n_j = \frac{Z_j e}{m_{jn} v_{jn}} n_j \mathbf{E} - \frac{k_B T_j}{m_{jn} v_{jn}} \nabla(n_j) - \frac{k_B T_j}{m_{jn} v_{jn}} \left( \frac{n_j}{k_B T_j} \right) \nabla(k_B T_j) + \mathbf{U}_n n_j. \quad (4-31)$$

To obtain the final drift-diffusion form, the mobility, diffusion and thermal diffusion coefficients are defined as

$$\begin{aligned} \mu_j &= \frac{e}{m_{jn} v_{jn}}, \\ D_j &= \frac{k_B T_j}{m_{jn} v_{jn}}, \\ D_j^T &= \frac{k_B T_j}{m_{jn} v_{jn}}. \end{aligned} \quad (4-32)$$

There exists a defined relationship between these three coefficients [53]. For particle velocity distributions close to *Maxwellian*, the mobility and diffusion coefficients are related as

$$\frac{D_j}{\mu_j} = \frac{k_B T_j}{e}, \quad (4-33)$$

which is known as the *Einstein relation* and  $D_j^T = D_j$ . For electrons  $\mu_e = e/m_e v_{en}$  and  $D_e = k_B T_e / m_e v_{en}$ , and for ions  $\mu_i = 2e/m_i v_{in}$  and  $D_i = 2k_B T_i / m_i v_{in}$ . The thermal diffusion coefficient is equal to [53]

$$D_j^T = \frac{k_B T_j}{m_{jn} v_{jn}} (1 - g_{T_j}),$$

$$\text{where } g_{T_j} \approx \frac{T_j}{v_{jn}} \frac{dv_{jn}}{dT_j}. \quad (4-34)$$

The coefficient ( $g_{T_j}$ ) has an accuracy of the order of unity, to find a more accurate value the motion and heat flux equations must be solved simultaneously [53]. Using this estimate, the thermal diffusion can be written as

$$D_j^T = T_j \frac{\partial D_j}{\partial T_j}. \quad (4-35)$$

The drift-diffusion approximation of the species flux is

$$\Gamma_j = Z_j \mu_j n_j \mathbf{E} - D_j \nabla(n_j) - D_j^T \left( \frac{n_j}{T_j} \right) \nabla(T_j) + \mathbf{U}_n n_j. \quad (4-36)$$

For electrons, the third term in (4-36), called the thermodiffusion flux, is usually smaller than the diffusion flux and it is typically neglected [43]. For all the cases shown in this study, the previous statement is also true for ions, therefore

$$\begin{aligned}\Gamma_j &= Z_j \mu_j n_j \mathbf{E} - \nabla(D_j n_j) + \mathbf{U}_n n_j, \\ &\cong Z_j \mu_j n_j \mathbf{E} - D_j \nabla(n_j) + \mathbf{U}_n n_j.\end{aligned}\quad (4-37)$$

Using the drift-diffusion approximation of the species flux, the continuity equation for each species can be solved without the corresponding momentum equations

$$\frac{\partial n_j}{\partial t} + \nabla \cdot \Gamma_j = S_j. \quad (4-38)$$

Likewise, the drift-diffusion approximation can be used in the electron energy equation. The energy equation can be cast in a form similar to the continuity equation with the help of the mean energy density ( $n_\varepsilon = n_e \bar{\varepsilon}$ ) as described by Hagelaar and Pitchford [57].

$$\begin{aligned}\frac{\partial n_\varepsilon}{\partial t} + \nabla \cdot \Gamma_\varepsilon + e \Gamma_e \cdot \mathbf{E} &= S_\varepsilon, \\ \text{where } \Gamma_\varepsilon &= -\mu_\varepsilon n_\varepsilon \mathbf{E} - D_\varepsilon \nabla(n_\varepsilon) + \frac{5}{3} \mathbf{U}_n n_\varepsilon,\end{aligned}\quad (4-39)$$

where the electron energy mobility and diffusion coefficients are related to the electron transport properties as [57]

$$\begin{aligned}\mu_\varepsilon &= \frac{5}{3} \mu_e, \\ D_\varepsilon &= \frac{5}{3} D_e.\end{aligned}\quad (4-40)$$

## Maxwell's Equations

The Maxwell's equations govern the behavior of the electric and magnetic fields that induce forces on the charged particles in a plasma. In a linear medium, where the electric polarization and magnetization are proportional to the electric and magnetic fields, Maxwell's equations are defined as [58]

$$\nabla \cdot (\epsilon \mathbf{E}) = \rho_{charge}, \quad (4-41)$$

$$\nabla \cdot \mathbf{B} = 0, \quad (4-42)$$

$$\nabla \times \mathbf{E} = -\frac{\partial \mathbf{B}}{\partial t}, \quad (4-43)$$

$$\nabla \times \left( \frac{1}{\mu} \mathbf{B} \right) = \mathbf{J}_{net} + \frac{\partial (\epsilon \mathbf{E})}{\partial t}. \quad (4-44)$$

In these equations,  $(\epsilon)$  and  $(\mu)$  are the permittivity and permeability of the material. For an argon plasma,  $(\epsilon = \epsilon_0 = 8.85418782 \times 10^{-12} m^{-3} kg^{-1} s^4 A^2)$  and  $(\mu = \mu_0 = 1.25663706 \times 10^{-6} m kg s^{-2} A^2)$  are the permittivity and permeability of free space. The net charge  $(\rho_{charge})$  and net current  $(\mathbf{J}_{net})$  are functions of the number densities and fluxes of the charged particles, respectively, and are obtained from the mass conservation equation, defined as [54]

$$\rho_{charge} = \sum_j (Z_j e n_j), \quad (4-45)$$

$$\mathbf{J}_{net} = \sum_j (Z_j e n_j \mathbf{u}_j) = \sum_j (Z_j e \Gamma_j). \quad (4-46)$$

For all the cases in this study, no external magnetic field  $\mathbf{B}$  is applied. The induced magnetic field generated by the time derivative  $\partial \mathbf{B} / \partial t$  of equation (4-43) is characterized by the magnetic Reynolds number defined as [54]

$$\text{Re}_m = \frac{UL}{\eta_m} = UL\mu_0\sigma, \quad (4-47)$$

where  $U$  and  $L$  are typical velocity and length scales of the flow. The variable ( $\sigma$ ) is the electrical conductivity of the material in question, which in the case of weakly ionized plasmas is equal to

$$\sigma = \frac{n_e e^2}{m_e v_{en}}. \quad (4-48)$$

If the magnetic Reynolds number is small ( $\text{Re}_m \ll 1$ ) the induced magnetic field is negligible due to the smoothing effect of the magnetic diffusivity ( $\eta_m$ ). For all the cases shown in this dissertation, the maximum magnetic Reynolds number, based on the electron velocity ( $U=U_e$ ), is of an order of  $10^{-2}$ . Therefore, the induced magnetic field is neglected.

In the absence of magnetic fields, equation (4-42) is satisfied automatically. Faraday's law (4-43) is satisfied by defining an electric potential ( $\phi$ ) such that ( $\mathbf{E} = -\nabla\phi$ ), since

$$\nabla \times \mathbf{E} = -\nabla \times \nabla \phi = 0. \quad (4-49)$$

The Ampere's law (4-44) is satisfied by solving the system of continuity equations (4-38). Each species continuity equation is multiplied by the species charge ( $Z_j e$ ) before they are added together

$$\begin{aligned} \sum_j \frac{\partial (Z_j e n_j)}{\partial t} + \nabla \cdot \sum_j (Z_j e \mathbf{\Gamma}_j) &= \sum_j Z_j e S_j = 0, \\ \frac{\partial \rho_{charge}}{\partial t} + \nabla \cdot \mathbf{J}_{net} &= 0, \\ \frac{\partial}{\partial t} [\nabla \cdot (\epsilon \mathbf{E})] + \nabla \cdot \mathbf{J}_{net} &= 0 = \nabla \cdot \nabla \times \left( \frac{1}{\mu} \mathbf{B} \right), \end{aligned} \quad (4-50)$$

where  $\sum_j Z_j e S_j = 0$  as long as the net charge is conserved through the constraint [54].

Gauss' law (4-41) is the only equation that needs to be solved in addition to the conservation laws, completing the coupling between the species number density and the electric field. The Poisson equation is obtained from Gauss' law as

$$\begin{aligned} \nabla \cdot (\epsilon \mathbf{E}) &= \rho_{charge}, \\ -\nabla \cdot (\epsilon \nabla \phi) &= \sum_j (Z_j e n_j). \end{aligned} \quad (4-51)$$

The governing equations defined by (4-38), (4-39), and (4-51) are written in the non-dimensional form using reference number density of  $10^{16} \text{ (m}^{-3}\text{)}$ , an electric potential of 100 (V), a length scale of 0.01 (m), an electron temperature of 10 (eV) and a time scale of  $10^{-10} \text{ (s)}$ .

## Transport Properties

The solution of the system of equations defined by (4-38), (4-39), and (4-51) requires models for the transport coefficients ( $\mu_j$  and  $D_j$ ) and the reaction rates ( $S_j$ ). In the LMEA model, the electron transport coefficients and reaction rates are calculated as functions of the mean electron energy ( $\bar{\varepsilon}$ ), which is computed from the electron energy equation given that ( $n_\varepsilon = n_e \bar{\varepsilon}$ ). The coefficients are tabulated using an electron Boltzmann equation solver called BOLSIG+ [57].

The ion mobility coefficient is obtained from Rafatov et al. [59] as

$$\mu_i = \left( \frac{4.411 \times 10^{21}}{n_n} \right) \left( 1 + \left( 7.721 \times 10^{-3} \left( 10^{21} \frac{|\mathbf{E}|}{n_n} \right) \right)^{3/2} \right)^{-0.33}, \quad (4-52)$$

where the electric field ( $\mathbf{E}$ ) is in (V/m) and the neutral number density ( $n_n$ ) is in ( $\text{m}^{-3}$ ), giving a mobility in ( $\text{m}^2/\text{Vs}$ ). The diffusion coefficient is obtained from *Einstein relation* ( $D_i = k_B T_i \mu_i / e$ ).

The mobility is zero for all the metastable species in this model and the metastable diffusion is the same as in Deconinck [11]

$$\begin{aligned} D_j &= \frac{k_B T_j}{m_j \bar{v}_{jn}}, \\ \bar{v}_{jn} &= n_n \bar{\sigma}_{jn} \bar{V}_{th,j}, \\ \bar{V}_{th,j} &= \sqrt{\frac{8k_B T_j}{\pi m_{jn}}}, \\ m_{jn} &= 0.5m_n, \end{aligned} \quad (4-53)$$

where  $(\bar{\nu}_{jn})$  is the collision frequency between metastable species ( $j$ ) and the background neutral species ( $n_n$ ),  $(\bar{\sigma}_{jn})$  is an approximate hard-sphere momentum transfer collision cross section based on the Lennard-Jones interaction potentials [60], and  $(\bar{V}_{th,j})$  is the average relative molecular speed.

The electron energy transport coefficients ( $\mu_\varepsilon$  and  $D_\varepsilon$ ) may be calculated using BOLSIG+ software [54]. Otherwise, the approximations (4-40) may be used to decrease the nonlinearity of the numerical simulation.

For an argon plasma with ions, electrons, and three types of metastable species, the neutral number density ( $n_n$ ) is calculated by solving the state equation

$$P_{gas} = k_B \left( n_n + \underbrace{n_i + n_S + n_P + n_D}_{\ll n_n} \right) T_{gas} + k_B n_e T_e, \quad (4-54)$$

where the subscripts ( $i$ ) and ( $e$ ) represent ions and electron, while the subscripts ( $S$ ,  $P$ , and  $D$ ) represent three types of metastable atoms named after their energy levels [61].

The reaction model includes elastic collisions and collisions that cause ionization, excitation, transition, and spontaneous emission. The elementary reactions considered for low-pressure, argon chemistry are given in [Table 4-1](#) [57].

The cross-sections for these reactions were obtained from Biagi [62] and the kinetic model section of Petrov and Ferreira [61] marked with superscripts B and P, respectively.

Detailed balancing was used for the reverse reaction of all “excitation” and “transition between excited states” reactions.

Table 4-1. Relevant Reactions. All reaction rates calculated using BOLSIG+ unless otherwise stated [57].

Index	Reaction	Type	$\Delta E_r^e$ (eV)	Coefficient
1	$e+Ar \rightarrow e+Ar$	Elastic collision	0	Boltz. <sup>B</sup>
2	$e+Ar \rightarrow 2e+Ar^+$	Direct ionization	15.7	Boltz. <sup>B</sup>
3	$e+Ar \leftrightarrow e+Ar_S^*$	Excitation	11.55	Boltz. <sup>B</sup>
4	$e+Ar \leftrightarrow e+Ar_P^*$	Excitation	13.0	Boltz. <sup>B</sup>
5	$e+Ar \leftrightarrow e+Ar_D^*$	Excitation	14.0	Boltz. <sup>B</sup>
6	$e+Ar_S^* \rightarrow 2e+Ar^+$	Stepwise Ionization	4.07	Boltz. <sup>P</sup>
7	$e+Ar_P^* \rightarrow 2e+Ar^+$	Stepwise Ionization	2.52	Boltz. <sup>P</sup>
8	$e+Ar_D^* \rightarrow 2e+Ar^+$	Stepwise Ionization	1.66	Boltz. <sup>P</sup>
9	$e+Ar_S^* \leftrightarrow e+Ar_P^*$	Trans. b/w Excited States	1.51	Boltz. <sup>P</sup>
10	$e+Ar_P^* \leftrightarrow e+Ar_D^*$	Trans. b/w Excited States	0.90	Boltz. <sup>P</sup>
11	$Ar_S^* + Ar_S^* \rightarrow Ar^+ + Ar + e$	Penning Ionization	-	$5.0 \times 10^{-16} \text{ m}^3/\text{s}^{\text{P}}$
12	$Ar_P^* + Ar_P^* \rightarrow Ar^+ + Ar + e$	Penning Ionization	-	$5.0 \times 10^{-16} \text{ m}^3/\text{s}^{\text{P}}$
13	$Ar_P^* + Ar_S^* \rightarrow Ar^+ + Ar + e$	Penning Ionization	-	$5.0 \times 10^{-16} \text{ m}^3/\text{s}^{\text{P}}$
14	$Ar_P^* + 2Ar \rightarrow Ar_S^* + 2Ar$	Trans. b/w Excited States	-	$5.0 \times 10^{-44} \text{ m}^6/\text{s}^{\text{P}}$
15	$Ar_P^* + Ar \rightarrow Ar_S^* + Ar$	Trans. b/w Excited States	-	$5.0 \times 10^{-17} \text{ m}^3/\text{s}^{\text{P}}$
16	$Ar_S^* \rightarrow Ar + hv$	Radiation	-	$7.00 \times 10^8 \text{ 1/s}^{\text{P}}$
17	$Ar_D^* \rightarrow Ar + hv$	Radiation	-	$5.96 \times 10^8 \text{ 1/s}^{\text{P}}$
18	$Ar_P^* \rightarrow Ar_S^* + hv$	Radiation	-	$3.76 \times 10^8 \text{ 1/s}^{\text{P}}$
19	$Ar_D^* \rightarrow Ar_P^* + hv$	Radiation	-	$1.46 \times 10^8 \text{ 1/s}^{\text{P}}$

<sup>B</sup> Cross-sections for these reactions were obtained from Biagi [62].

<sup>P</sup> Cross-sections for these reactions were obtained from Petrov and Ferreira [61].

The source terms ( $S_j$ ) in the continuity equations are determined by the reactions occurring in the discharge described in Table 4-1, where the source terms for ions and electrons are identical due to the particle conservation,

$$S_e = S_i = R_2 n_n n_e + R_6 n_S n_e + R_7 n_P n_e + R_8 n_D n_e + R_{11} n_S n_S + R_{12} n_P n_P + R_{13} n_S n_P, \quad (4-55)$$

$$S_S = R_3 n_n n_e - R_{3(rev)} n_S n_e - R_6 n_S n_e - R_9 n_S n_e + R_{9(rev)} n_P n_e - 2R_{11} n_S n_S - R_{13} n_P n_S + R_{14} n_P n_n n_n + R_{15} n_P n_n - R_{16} n_S + R_{18} n_P, \quad (4-56)$$

$$S_P = R_4 n_n n_e - R_{4(rev)} n_P n_e - R_7 n_P n_e + R_9 n_S n_e - R_{9(rev)} n_P n_e - 2R_{12} n_P n_P - R_{13} n_P n_S - R_{14} n_P n_n n_n - R_{15} n_P n_n - R_{18} n_P + R_{19} n_D, \quad (4-57)$$

$$S_D = R_5 n_n n_e - R_{5(rev)} n_D n_e - R_8 n_D n_e + R_{10} n_P n_e - R_{10(rev)} n_D n_e - R_{17} n_D - R_{19} n_D, \quad (4-58)$$

where the subscript (*rev*) in some of the reaction rates (*R*) is for the reverse reaction. In order to complete the model, the source term for the electron energy equation is defined as [11]

$$S_\epsilon = -\frac{3}{2} \frac{2m_e}{m_n} \bar{v}_{en} n_e k_B (T_e - T_{gas}) - e \sum_r R_r N n_e \Delta E_r^e, \quad (4-59)$$

where *N* is the number density of the heavy particle in the given reaction,  $\bar{v}_{en}$  is the electron atomic elastic collision, and  $\Delta E_r^e$  is the energy loss (or gain) due to inelastic collisions during the reaction (*r*). These two terms in the equation represent the changes in electron energy due to elastic collisions and inelastic processes, respectively.

### Boundary Conditions

In order to solve the drift-diffusion model, a set of boundary conditions is necessary. The imposed boundary conditions are different depending on the behavior of the system near an anode electrode, cathode electrode, dielectric wall, or an open

surface exposed to the gas. A more extensive discussion of the typical boundary conditions for fluid models of gas discharge is presented by Hagelaar et al. [63].

### Open surface boundary

If the boundary is an open surface exposed to the gas, then the flux components due to the mobility and the diffusion normal to the boundary are equal to zero in (4-37) and (4-39). Similarly, the electric field (or potential gradient) normal to the boundary is assumed to be zero because the given boundary is sufficiently far away from the area of high number density of charged particles (near the cathode).

For the 2-D cases, the inlet boundary and the bottom of the computational domain have

$$\Gamma_j \cdot \hat{\mathbf{n}} = 0, \text{ and } \Gamma_\varepsilon \cdot \hat{\mathbf{n}} = 0, \quad (4-60)$$

where ( $\hat{\mathbf{n}}$ ) is the outward normal unit vector to the boundary in question. This condition is imposed at the inlet due to numeral stability reasons. The exit plane of the channel has

$$\Gamma_j \cdot \hat{\mathbf{n}} = \mathbf{U}_n n_j, \text{ and } \Gamma_\varepsilon \cdot \hat{\mathbf{n}} = \frac{5}{3} \mathbf{U}_n n_\varepsilon. \quad (4-61)$$

When the solution reaches steady state, the number densities are so small that these boundary conditions become the same as (4-60). The electric field normal to the boundary is

$$\mathbf{E} \cdot \hat{\mathbf{n}} = -\nabla \phi \cdot \hat{\mathbf{n}} = 0. \quad (4-62)$$

## Anode boundary

The flux of particles towards a surface can be derived using kinetic theory as

$$\Gamma_j \cdot \hat{\mathbf{n}} = \underbrace{\frac{1}{4} v_{th,j} n_j}_{\text{Thermal Flux}} + \underbrace{\hat{\alpha} n_j \mu_j \text{sgn}(Z_j) (\mathbf{E} \cdot \hat{\mathbf{n}})}_{\text{Drift Flux}}, \quad (4-63)$$

$$v_{th,j} = \sqrt{\frac{8k_B T_j}{\pi m_j}},$$

where the coefficient ( $\hat{\alpha}$ ) is set equal to zero if the electric field normal to the wall multiplied by the sign of the charge of the species  $\text{sgn}(Z_j)(\mathbf{E} \cdot \hat{\mathbf{n}})$  is in the direction pointing away from the wall, and it is set equal to one otherwise [54]. The variable  $v_{th,j}$  is the average thermal velocity of species ( $j$ ). The diffusion of the charged species in the sheath region (near the wall) is smaller than the drift flux and it is usually neglected [64]. For the electrons, ( $\hat{\alpha} = 0$ ) for all the cases in this study due to the short distance between electrodes, which makes all the cases operate in an *obstructed glow* mode (previously explained in the section labeled as *Qualitative Characteristics of DC Glow Discharge*).

The energy flux towards a surface has the form

$$\Gamma_e \cdot \hat{\mathbf{n}} = 2k_B T_e (\Gamma_e \cdot \hat{\mathbf{n}}). \quad (4-64)$$

The expression for the energy flux is not equal to the product of the wall flux ( $\Gamma_e \cdot \hat{\mathbf{n}}$ ) with the mean energy ( $\bar{\varepsilon}$ ) because particles with higher energy hit the wall more frequently and contribute more power to the wall [44].

The electric potential ( $\phi$ ) at the anode is fixed to an applied value (Dirichlet boundary condition or first type), which may vary in time for the RF-cases.

### Cathode boundary

The cathode boundary conditions are identical to the anode boundary conditions except for an additional term in the electron particle flux and a corresponding additional term in the electron energy flux. These terms are due to the secondary electron emission, characterized by the secondary emission coefficient ( $\gamma_{sec}$ ), which depends on the cathode material and gas [54]. The cathode boundary condition for electrons is

$$\begin{aligned} \Gamma_e \cdot \hat{n} &= \underbrace{\frac{1}{4} v_{th,e} n_e}_{\text{Thermal Flux}} - \underbrace{\hat{\alpha} n_e \mu_e (\mathbf{E} \cdot \hat{n})}_{\text{Drift Flux}} - \underbrace{\gamma (\Gamma_i \cdot \hat{n})}_{\text{Secondary Emission}}, \\ \Gamma_\varepsilon \cdot \hat{n} &= 2k_B T_e (\Gamma_e \cdot \hat{n}). \end{aligned} \quad (4-65)$$

### Dielectric wall

The particle and electron energy fluxes for a dielectric wall are identical to the ones at the anode. At the interface between two materials (in the RGEJ case dielectric above and plasma below the interface) with different permittivity constants, the electric field is defined as [65]

$$(\epsilon \mathbf{E} \cdot \hat{n})_{dielectric} - (\epsilon \mathbf{E} \cdot \hat{n})_{plasma} = \rho_s, \quad (4-66)$$

where ( $\rho_s$ ) is the charge on the dielectric surface calculated by assuming that the charged particles striking the wall recombine instantly and no diffusion of charge along the wall occurs [54]. The surface charge is calculated as [11]

$$\frac{\partial \rho_s}{\partial t} = \sum_j Z_j e (\Gamma_j \cdot \hat{n}). \quad (4-67)$$

For all cases shown, the electrodes are exposed instead of embedded inside the dielectric material. The boundary condition used in the RGEJ cases is

$$\left( \epsilon_0 \frac{\partial \phi}{\partial y} \right) = \rho_s, \quad (4-68)$$

$$\frac{\partial \rho_s}{\partial t} = e (\Gamma_i - \Gamma_e),$$

where it is assumed that the contribution of the dielectric material to the dielectric boundary equation is negligible due to several thrusters being stack together (similar to the design of FMMR) and separated by a relatively thin dielectric wall.

### **Plasma Electrostatic Force and Electrothermal Heating Source**

The volumetric plasma-induced electrostatic force and the volumetric electrothermal heating source are calculated as [11], [66]

$$\mathbf{F} = e(n_i - n_e)\mathbf{E}, \quad (4-69)$$

$$q''' = e(\Gamma_i \cdot \mathbf{E}). \quad (4-70)$$

In equation (4-70), the term on the RHS is the ion Joule heating, since only the heavy particles thermalize with the bulk gas. The ion Joule heating term usually has a thermalization factor that accounts for the fraction of energy that is locally equilibrated with the gas. In a xenon discharge at 100 (Torr), it was assumed by Boeuf et al. [67] that only 25% of the energy was deposited in the neutral gas and the maximum gas temperature (~460 K) of their simulation matched relatively well with the gas temperature (~500 K) obtained from experiments. In this case, the ion Joule heating rapidly equilibrates with the gas since the ion-neutral mean free path ( $\lambda_i = v_{th,i}/v_{in}$ ) is orders of magnitude smaller than the device length scale, a conservative approach is taken to obtain the upper bound for the gas heating, and the thermalization factor is assumed to be equal to one [66].

### Rarefied Gas Equations

In the rarefied gas simulation, density-based compressible flow equations were used with the assumption of ideal gas ( $P = \rho RT$ ) using argon as the working fluid. The continuity, momentum, and energy equations are given by Raju [68], with the additions of the terms ( $F_x, F_y, q'''$ ) in the right-hand-side of the momentum (in the x and y) and energy equations, respectively.

The continuity equation, compressible momentum equations in 2-D (in the x and y) with ideal gas assumption, and energy equation are

$$\frac{\partial \rho}{\partial t} + \frac{\partial (u\rho)}{\partial x} + \frac{\partial (v\rho)}{\partial y} = 0, \quad (4-71)$$

$$\begin{aligned} & \frac{\partial u}{\partial t} + u \frac{\partial u}{\partial x} + v \frac{\partial u}{\partial y} + R \frac{\partial T}{\partial x} + \frac{RT}{\rho} \frac{\partial \rho}{\partial x} - \frac{F_x}{\rho} \\ & - \frac{1}{\rho} \left[ \frac{4}{3} \frac{\partial}{\partial x} \left( \mu \frac{\partial u}{\partial x} \right) + \frac{\partial}{\partial y} \left( \mu \frac{\partial u}{\partial y} \right) - \frac{2}{3} \frac{\partial}{\partial x} \left( \mu \frac{\partial v}{\partial y} \right) + \frac{\partial}{\partial y} \left( \mu \frac{\partial v}{\partial x} \right) \right] = 0, \end{aligned} \quad (4-72)$$

$$\begin{aligned} & \frac{\partial v}{\partial t} + u \frac{\partial v}{\partial x} + v \frac{\partial v}{\partial y} + R \frac{\partial T}{\partial y} + \frac{RT}{\rho} \frac{\partial \rho}{\partial y} - \frac{F_y}{\rho} \\ & - \frac{1}{\rho} \left[ \frac{\partial}{\partial x} \left( \mu \frac{\partial v}{\partial x} \right) + \frac{4}{3} \frac{\partial}{\partial y} \left( \mu \frac{\partial v}{\partial y} \right) - \frac{2}{3} \frac{\partial}{\partial y} \left( \mu \frac{\partial u}{\partial x} \right) + \frac{\partial}{\partial x} \left( \mu \frac{\partial u}{\partial y} \right) \right] = 0, \end{aligned} \quad (4-73)$$

$$\begin{aligned} & \frac{\partial T}{\partial t} + u \frac{\partial T}{\partial x} + v \frac{\partial T}{\partial y} + \frac{RT}{c_v} \left[ \frac{\partial u}{\partial x} + \frac{\partial v}{\partial y} \right] - \frac{1}{\rho c_v} \left[ \frac{\partial}{\partial x} \left( \kappa \frac{\partial T}{\partial x} \right) - \frac{\partial}{\partial y} \left( \kappa \frac{\partial T}{\partial y} \right) - q''' \right] \\ & - \frac{\mu}{\rho c_v} \left[ \frac{4}{3} \left( \frac{\partial u}{\partial x} \right)^2 + \frac{4}{3} \left( \frac{\partial v}{\partial y} \right)^2 - \frac{4}{3} \frac{\partial u}{\partial x} \frac{\partial v}{\partial y} + \left( \frac{\partial v}{\partial x} \right)^2 + \left( \frac{\partial u}{\partial y} \right)^2 + 2 \frac{\partial v}{\partial x} \frac{\partial u}{\partial y} \right] = 0. \end{aligned} \quad (4-74)$$

In these equations, ( $\rho$ ) is the density, ( $u$ ) and ( $v$ ) are the  $x$  and  $y$  components of velocity, ( $T$ ) is the gas temperature,  $R$  is the gas constant ( $R=208.1$  J/kg-K) for argon, ( $c_v$ ) is the specific heat at constant volume,  $c_v = R/(\gamma - 1)$ , where the specific heat ratio ( $\gamma$ ) is equal to 1.667. The thermal conductivity ( $\kappa$ ) and the viscosity ( $\mu$ ) are functions of the gas temperature [69]

$$\begin{aligned} \mu = & -4.688268 \times 10^{-18} T^4 + 2.608773 \times 10^{-14} T^3 - 5.761201 \times 10^{-11} T^2 \\ & + 9.224244 \times 10^{-8} T - 3.936359 \times 10^{-7}, \end{aligned} \quad (4-75)$$

$$\begin{aligned} \kappa = & -3.591506 \times 10^{-15} T^4 + 2.006139 \times 10^{-11} T^3 - 4.456168 \times 10^{-8} T^2 \\ & + 7.199751 \times 10^{-5} T - 3.170661 \times 10^{-4}, \end{aligned} \quad (4-76)$$

where ( $\mu$ ) is in (Pa-s), ( $\kappa$ ) is in (W/m-K), and ( $80 \text{ K} \leq T \leq 2000 \text{ K}$ ).

The governing equations are written in the non-dimensional form using a velocity of 100 (m/s), a length scale of 0.01 (m), a pressure of 100 (Pa), a temperature of 300 K, and density from the ideal gas law using these parameters.

**Boundary conditions for rarefied gas:** The Knudsen number ( $Kn$ ) is defined as the ratio of the molecular mean free path length ( $\lambda_m$ ) to a representative physical length scale, which in this case is the height ( $H$ ) of the inlet of the micro-channel and it is much smaller than the micro-channel length. The Knudsen number and mean free path are defined as [70], [71]

$$Kn = \frac{\lambda_m}{H}, \tag{4-77}$$

$$\lambda_m = \frac{1}{\sqrt{2}n\pi d^2}, \tag{4-78}$$

where  $d$  and  $n$  are the atomic diameter and gas number density.

$Kn$  is used to determine which numerical modeling approach is more appropriate: statistical mechanics or continuum mechanics. The figure below shows the equations use to model different flow regimes.

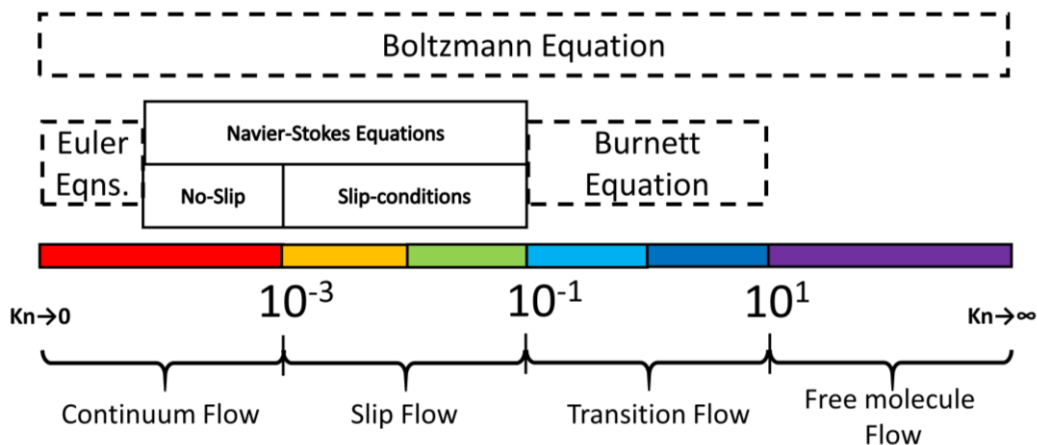


Figure 4-1. Gas flow regimes depending on  $Kn$  [68].

As  $Kn \rightarrow 0$ , the flow is assumed sufficiently continuous, while for  $Kn > 10$ , the flow is assumed free-molecule. For  $10^{-3} < Kn < 10$  the flow is neither sufficiently continuum nor completely molecular [68]. For this range, the flow is further divided into two subcategories: slip flow regime  $10^{-3} < Kn < 10^{-1}$  and transitional regime for  $10^{-1} < Kn < 10$  as explained by Raju [68]. In the RGEJ cases,  $Kn$  is in the slip regime by design.

The boundary conditions for the rarefied gas simulations of the RGEJ are fixed stagnation density and temperature at the inlet ( $\rho_0 = P_0/RT_0$ ,  $T_0=300$  K, where  $P_0=133.3$  Pa). Isentropic flow assumption is used to calculate the static density and temperature at the inlet plane. At the walls there is no penetration, the normal velocity is equal to zero. At the outlet, static pressure is assumed to be ( $P_{Out}=0.05$  Torr) if Mach number is subsonic and ( $\rho_{Out}=P_{Out}/RT_{Out}$ ), else  $\rho$  is extrapolated from internal nodes. Boundary conditions for a rarefied gas are used for tangential velocity and temperature at the wall face, as described by Maxwell [72] and Smoluchowski [73], similar to Raju [68]. For example, for the top wall face inside the channel, the tangential velocity boundary condition is

$$u - u_{wall} = \frac{2 - \sigma_v}{\sigma_v} \lambda_m \left( \frac{\partial u}{\partial r} \right) \Big|_w + \frac{3}{4} \frac{\mu}{\rho T} \left( \frac{\partial T}{\partial x} \right) \Big|_w. \quad (4-79)$$

The corresponding temperature boundary condition for an isothermal wall is

$$T - T_{wall} = \frac{2 - \sigma_T}{\sigma_T} \left[ \frac{2\gamma}{\gamma + 1} \right] \frac{\lambda_m}{Pr} \left( \frac{\partial T}{\partial r} \right) \Big|_w. \quad (4-80)$$

For these equations, ( $r$ ) is the distance from the wall normal to it, for the top surface ( $r=H-y$ ). If a case is adiabatic,  $\partial T/\partial x = 0$  or  $\partial T/\partial y = 0$  is used as a temperature boundary condition at the wall. In these equations, the new variables introduced are the *Prandtl number* ( $Pr$ ), the specific heat ratio ( $\gamma$ ), the tangential-momentum-accommodation coefficient ( $0 \leq \sigma_v \leq 1$ ), and the thermal-accommodation coefficient ( $0 \leq \sigma_T \leq 1$ ).

*Specular* reflection happens when the gas molecules are reflected from the wall at an angle equal to the incident angle exerting no shear stress on the wall. *Diffuse* reflection happens when the channel surface is rough and the gas molecules are reflected at random angles. The accommodation coefficients indicate the fraction of the molecules reflected diffusively from the walls [68]. The tangential momentum accommodation coefficient ( $\sigma_v = 0.89$  [74]) and the thermal accommodation coefficient ( $\sigma_T = 0.87$  [75]) found in the formulas of slip flow boundary conditions are selected based on average values for argon interacting with different materials.

Using the definition of mean free path (4-78) and the expression of the viscosity of dilute gases [71]

$$\begin{aligned}\mu &= \frac{5}{64a^2} \left( \frac{mk_B T}{\pi} \right)^{1/2}, \\ P &= nk_B T = \rho R T, \quad \rho = mn, \quad d = 2a, \\ \lambda_m &= \frac{1}{\sqrt{2}n\pi d^2} \cong \frac{16\mu}{5\rho\sqrt{2\pi R T}},\end{aligned}\tag{4-81}$$

obtained using the Chapman-Enskog method where  $m$  is the molecular mass and  $a$  is the atomic radius, the boundary condition formulas can be modified.

The boundary conditions can be solved for the fluxes as [68]

$$-\frac{\mu}{\rho} \left( \frac{\partial u}{\partial y} \right) \Big|_{y=H/2} = \frac{5\sqrt{2\pi RT}}{16} \frac{\sigma_v}{(2-\sigma_v)} \left[ u - \frac{3}{4} \frac{\mu}{\rho T} \left( \frac{\partial T}{\partial x} \right) \Big|_{y=H/2} \right], \quad (4-82)$$

$$-\frac{\kappa}{\rho c_v} \left( \frac{\partial T}{\partial y} \right) \Big|_{y=H/2} = \frac{5\sqrt{2\pi RT}}{16} \frac{\sigma_T}{(2-\sigma_T)} \left( \frac{\gamma+1}{2} \right) [T - T_{wall}], \quad (4-83)$$

which allows the boundary conditions to be implemented into the simulation through the weak statement of the Galerkin method.

The rest of the boundary conditions needed are zero flux normal to the edges of the domain [ $\partial(\dots)/\partial x = 0$  or  $\partial(\dots)/\partial y = 0$ ].

### Heat Transfer Governing Equations

For micro-propulsion devices, heat loss via radiation and conduction are major concerns. As stated in [chapter 1](#), FMRR was shown to have significant heat loss, a problem that ultimately prevented its application. In order to estimate the heat loss through radiation and conduction in the RGEJ, the temperature distributions inside the channel walls and the external walls are used as boundary conditions or inputs to perform a thermal analysis. These temperature distributions are obtained from the numerical simulation of the loosely couple gas modules of the numerical code. The thermal analysis is not couple with the gas modules.

### Thermal Radiation Heat Transfer

In the thermal radiation analysis, a simplified model is used with the assumption of grey, diffuse surfaces with a non-participating medium, allowing the radiation properties to be independent of wavelength and direction. To model the problem the

equation for radiative exchange between gray, diffuse surfaces was used and written in the following way

$$\frac{q_i}{\varepsilon_i} - \sum_{j=1}^N \left( \frac{1}{\varepsilon_j} - 1 \right) F_{i-j} q_j + H_{oi} = E_{bi} - \sum_{j=1}^N F_{i-j} E_{bj}, \quad (4-84)$$

where  $E_b = \sigma_{SB} T^4$ ,  $\sigma_{SB} = 5.67 \times 10^{-8} \left( \frac{\text{kg}}{\text{s}^3 \text{K}^4} \right)$  and  $i = 1, 2, \dots, N$ .

In this equation,  $\varepsilon_j$  are the emissivities of the given surface,  $q_j$  are the unknown heat fluxes,  $E_{bj}$  are the known emissive powers,  $H_{oi}$  are the external irradiations.

Additionally,  $\delta_{ij}$  is the *Kronecker delta*  $\sigma_{SB}$  is the Stefan-Boltzmann constant,  $T$  is the temperature of the surfaces, and  $F_{i-j}$  are the view factors for  $N$  number of surfaces.

### View Factor Formulas

The view factor of a plate with itself or any other plate on the same face is equal to zero since the faces are all flat surfaces. The view factors are calculated using equations from Modest [76].

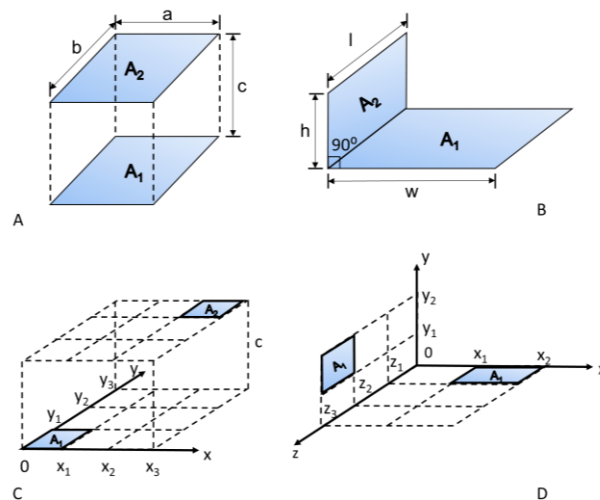


Figure 4-2. View Factors. A) Parallel plates, B) perpendicular plates, C) any two parallel plates, and D) any two perpendicular plates [76].

The view factors are numerically calculated by first coding the simple formulas for “identical, parallel, directly opposed rectangles,” see [Figure 4-2\(A\)](#),

$$F_{1-2} = \frac{2}{\pi XY} \left\{ \ln \left[ \frac{(1+X^2)(1+Y^2)}{(1+X^2+Y^2)} \right]^{1/2} + X\sqrt{1+Y^2} \tan^{-1} \left( \frac{X}{\sqrt{1+Y^2}} \right) \right. \\ \left. + Y\sqrt{1+X^2} \tan^{-1} \left( \frac{Y}{\sqrt{1+X^2}} \right) - X \tan^{-1}(X) - Y \tan^{-1}(Y) \right\}, \quad (4-85)$$

$$X = \frac{a}{c}, \quad Y = \frac{b}{c},$$

and for “two finite rectangles of the same length, having one common edge, and at an angle of 90° to each other,” see [Figure 4-2\(C\)](#),

$$F_{1-2} = \frac{1}{\pi W} \left( W \tan^{-1} \left( \frac{1}{W} \right) + H \tan^{-1} \left( \frac{1}{H} \right) - \sqrt{H^2 + W^2} \tan^{-1} \left( \frac{1}{\sqrt{H^2 + W^2}} \right) \right. \\ \left. + \frac{1}{4} \ln \left\{ \frac{(1+W^2)(1+H^2)}{(1+W^2+H^2)} \right. \right. \\ \left. \left. \left[ \frac{W^2(1+W^2+H^2)}{(1+W^2)(W^2+H^2)} \right]^{W^2} \left[ \frac{H^2(1+H^2+W^2)}{(1+H^2)(H^2+W^2)} \right]^{H^2} \right\} \right), \quad (4-86)$$

$$H = \frac{h}{l}, \quad W = \frac{w}{l}.$$

These two previous simple formulas are subroutines of the more complicated functions that calculate the view factors for “any two parallel plates,” see [Figure 4-2\(B\)](#),

$$\begin{aligned}
4A_1F_{1-2} &= f(x_3, y_3) - f(x_3, y_2) - f(x_3, y_3 - y_1) + f(x_3, y_2 - y_1) \\
&- [f(x_2, y_3) - f(x_2, y_2) - f(x_2, y_3 - y_1) + f(x_2, y_2 - y_1)] \\
&- [f(x_3 - x_1, y_3) - f(x_3 - x_1, y_2) - f(x_3 - x_1, y_3 - y_1) + f(x_3 - x_1, y_2 - y_1)] \\
&+ f(x_2 - x_1, y_3) - f(x_2 - x_1, y_2) - f(x_2 - x_1, y_3 - y_1) + f(x_2 - x_1, y_2 - y_1),
\end{aligned} \tag{4-87}$$

where  $f(a, b) = A_1F_{1-2}$  and for “any two perpendicular plates,” see [Figure 4-2\(D\)](#),

$$\begin{aligned}
2A_1F_{1-2} &= f(x_2, y_2, z_3) - f(x_2, y_1, z_3) - f(x_1, y_2, z_3) + f(x_1, y_1, z_3) \\
&+ f(x_1, y_2, z_2) - f(x_1, y_1, z_2) - f(x_2, y_2, z_2) + f(x_2, y_1, z_2) \\
&- f(x_2, y_2, z_3 - z_1) + f(x_2, y_1, z_3 - z_1) + f(x_1, y_2, z_3 - z_1) - f(x_1, y_1, z_3 - z_1) \\
&+ f(x_2, y_2, z_2 - z_1) - f(x_2, y_1, z_2 - z_1) - f(x_1, y_2, z_2 - z_1) + f(x_1, y_1, z_2 - z_1),
\end{aligned} \tag{4-88}$$

where  $f(w, h, l) = A_1F_{1-2}$ .

### Conduction Heat Transfer

To calculate the conduction heat transfer through the wall of the thruster, the heat transfer equation was used,

$$\rho c_p \frac{\partial T}{\partial t} - \nabla \cdot (\kappa \nabla T) = \dot{q}_v. \tag{4-89}$$

In this equation,  $c_p$  is the specific heat capacity,  $\rho$  is the density, and  $\kappa$  is the thermal conductivity of the material, while  $\dot{q}_v$  is the volumetric heat source. For the case examined, only the solution at steady state is important and there is no volumetric heat source in the equation, therefore, only the Laplace equation is solved as

$$\frac{\partial^2 T}{\partial x^2} + \frac{\partial^2 T}{\partial y^2} = 0. \tag{4-90}$$

## Conduction Heat Transfer Boundary Conditions

The boundary conditions for the conduction simulation can be either a fixed temperature (Dirichlet or first type) or heat flux via radiation. Dirichlet is used everywhere the temperature is known. Heat flux via radiation boundary is used in places where there is heat transfer from the thruster walls to the internal components of the small satellite, assuming the temperature of the components of a small satellite is known and is quasi-statically constant. This boundary is written as [77]

$$\begin{aligned} -\kappa \frac{\partial T}{\partial y} \Big|_{Wall} &= \varepsilon_{Total} \sigma_{SB} (T_{Wall}^4 - T_{Comp.}^4), \\ \varepsilon_{Total} &= \left( \frac{1}{\varepsilon_1} + \frac{1}{\varepsilon_2} + \frac{1 - \varepsilon_{3,1}}{\varepsilon_{3,1}} + \frac{1 - \varepsilon_{3,2}}{\varepsilon_{3,2}} \right)^{-1}. \end{aligned} \tag{4-91}$$

for multiple layers of thermal radiation insulation dividing the space between the thruster and the other components of the small satellite separated from the thruster by a small distance. The multiple layers are a layer of aluminum surrounding the dielectric material ( $\varepsilon_1 = 0.02$ ) and a thin layer of aluminum ( $\varepsilon_{3,1} = \varepsilon_{3,2} = 0.02$ ) in-between the thruster and all other components. The components of the small satellite are assumed to be a black body ( $\varepsilon_2 = 1$ ) for simplicity.

## CHAPTER 5 NUMERICAL MODEL

In this study, an existing, previously described in literature, in-house modular Multi-scale Ionized Gas (MIG) flow solver platform developed by Balagangadhar and Roy [78], [79] was used. The MIG flow solver platform has been utilized for many different applications using different finite element modules, including electric propulsion, micro-flows, nanoscale flows, fluid dynamics, and plasma physics [80], [81], [82], [83]. For this dissertation, two modules of the MIG code have been utilized: an existing finite element based rarefied gas module (RGM) and a recently developed finite difference based ionized gas module (IGM). They are loosely coupled in the following sequence. The RGM runs until convergence, producing the gas density ( $\rho$ ), components of velocity ( $u$ ,  $v$ ), and temperature ( $T$ ). These variables from the RGM are passed to the IGM. Then, the IGM runs until convergence, producing the volumetric plasma-induced electrostatic force components ( $F_x$ ,  $F_y$ ) and the volumetric electro-thermal heating source ( $q'''$ ) needed by the new run of the RGM. The information obtained by each module is exchanged in this fashion until the steady-state solution is obtained. [Figure 5-1](#) shows the process.

In [Figure 5-1](#), the first step initializes the variables of both modules, including the initial voltage ( $V_i$ ) value, based on the plasma breakdown voltage of the gas ( $\sim 150$  V for argon). Each module uses the  $L^2$ -norm of the solution to test for convergence. After both modules have reached convergence at a given voltage, the voltage is increased by a voltage difference ( $\Delta V$ ) and the process is repeated, until the maximum voltage ( $V_{\max}$ ) desired is achieved. For all cases in this study, ( $\Delta V$ ) is 50 V. After the IGM reaches local convergence, a test for global convergence is performed.

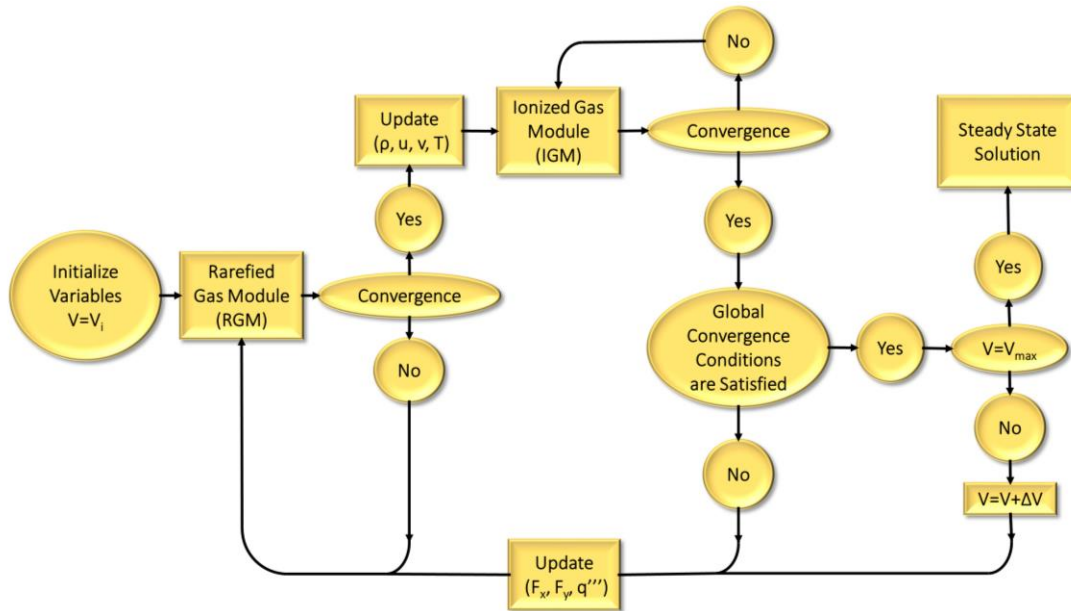


Figure 5-1. Schematic of the new MIG code with rarefied gas and ionized gas modules.

The RGM and the IGM are run for five time steps even if their  $L^2$ -norms are less than their tolerances. If the  $L^2$ -norm of each module is less than its tolerance for all five consecutive time steps for three consecutive iterative loops between the RGM and the IGM, then global convergence conditions are satisfied. The  $L^2$ -norms for the RGM and the IGM, using the given non-dimensionalization explained in the following sections, are  $10^{-4}$  and  $10^{-10}$  for time steps of  $10^{-8}$  and  $5 \times 10^{-13}$  seconds for each module, respectively.

In this chapter, an overview of the numerical schemes and relevant information for each model will be provided.

### The Ionized Gas Module

The system of governing equations for the plasma, the system of equations defined by (4-38), (4-39), and (4-51), is solved using the semi-implicit, finite difference scheme module of the Multiscale Ionized Gas (MIG) code [78], [79]. The equations are solved decoupled starting with the steady Poisson equation, then the ion continuity

equation, and the three metastable atoms continuity equations. The electron continuity and electron energy density equations are solved coupled with each other. Poisson equation is approximated by combining the continuity equations of ions and electrons to predict the charge at present time step as

$$\nabla^2 \phi^{n+1} = -\frac{e}{\epsilon_0} (n_i^{n+1} - n_e^{n+1}) \approx -\frac{e}{\epsilon_0} [n_i^n - n_e^n + \Delta t (\nabla \cdot \Gamma_e^n - \nabla \cdot \Gamma_i^n)]. \quad (5-1)$$

The Poisson equation is solved using second-order central difference scheme where the right-hand-side is treated as a source ( $S_\phi$ ) since it depends on previous time step information.

$$\frac{\phi_{i+\Delta x, j}^{n+1} - 2\phi_{i, j}^{n+1} + \phi_{i-\Delta x, j}^{n+1}}{\Delta x^2} + \frac{\phi_{i, j+\Delta y}^{n+1} - 2\phi_{i, j}^{n+1} + \phi_{i, j-\Delta y}^{n+1}}{\Delta y^2} = (S_\phi)_{i, j}^n. \quad (5-2)$$

In this equation, the superscripts ( $i, j$ ) and ( $n$ ) refer to the grid spacing and time discretization.

The continuity equations for ions, electrons, and metastable atoms are solved using second-order central difference on a staggered mesh and first-order, implicit Euler method time discretization schemes for numerical stability.

$$\frac{(n_k)_{i, j}^{n+1} - (n_k)_{i, j}^n}{\Delta t} + \frac{(\Gamma_{k, x})_{i+\Delta x/2, j}^{n+1} - (\Gamma_{k, x})_{i-\Delta x/2, j}^{n+1}}{\Delta x} + \frac{(\Gamma_{k, y})_{i, j+\Delta y/2}^{n+1} - (\Gamma_{k, y})_{i, j-\Delta y/2}^{n+1}}{\Delta y} = (S_k)_{i, j}^n, \quad (5-3)$$

where the fluxes are solved using the Scharfetter-Gummel flux discretization scheme and the sources ( $S_k$ ) are treated explicitly [84]. The Scharfetter-Gummel flux

discretization was devised to solve the drift-diffusion equations for semiconductor applications [54]. An upwind discretization of the flux is embedded in the method, causing monotonic solutions for large values of electric field. The Scharfetter-Gummel flux discretization assumes that the flux between two grid points is constant and the potential is linear. The value of the flux is found at the center between these two grid points. The  $(k)$  subscript in these equations refers to ions, electrons, or three types of metastable atoms. The discretization of one of the fluxes needed is given as

$$\begin{aligned}
 (\Gamma_{k,x})_{i+\Delta x/2,j}^{n+1} &= (b_{k,x})_{i+\Delta x/2,j}^{n+1} (\eta_{k,x})_{i+\Delta x/2,j}^{n+1} + (n_k)_{i,j}^{n+1} (u_{i,j}), \\
 (b_{k,x})_{i+\Delta x/2,j}^{n+1} &= \frac{\text{sgn}(q_k) (\mu_k)_{i+\Delta x/2,j}^{n+1} (E_x)_{i+\Delta x/2,j}^{n+1}}{(D_k)_{i+\Delta x/2,j}^{n+1}}, \\
 (\eta_{k,x})_{i+\Delta x/2,j}^{n+1} &= (D_k)_{i+\Delta x/2,j}^{n+1} \left[ \frac{(n_k)_{i,j}^{n+1}}{1 - \exp(-(\Delta x)(b_{k,x})_{i+\Delta x/2,j}^{n+1})} + \frac{(n_k)_{i+\Delta x,j}^{n+1}}{1 - \exp(+\Delta x(b_{k,x})_{i+\Delta x/2,j}^{n+1})} \right].
 \end{aligned} \tag{5-4}$$

In the previous equation,  $u$  is the x-component of the gas velocity since ( $\mathbf{U}_n \approx \mathbf{U}_{\text{gas}}$ ).

The electron energy density equation is solved in a similar manner, simultaneously with the electron continuity equation using a Newton-Raphson non-linear solver,

$$\begin{aligned}
& \frac{(n_\varepsilon)_{i,j}^{n+1} - (n_\varepsilon)_{i,j}^n}{\Delta t} + \frac{(\Gamma_{\varepsilon,x})_{i+\Delta x/2,j}^{n+1} - (\Gamma_{\varepsilon,x})_{i-\Delta x/2,j}^{n+1}}{\Delta x} + \frac{(\Gamma_{\varepsilon,y})_{i,j+\Delta y/2}^{n+1} - (\Gamma_{\varepsilon,y})_{i,j-\Delta y/2}^{n+1}}{\Delta y} = \\
& -e \frac{\left[ (\Gamma_{e,x})_{i+\Delta x/2,j}^{n+1} + (\Gamma_{e,x})_{i-\Delta x/2,j}^{n+1} \right] \left[ (E_x)_{i+\Delta x/2,j}^{n+1} + (E_x)_{i-\Delta x/2,j}^{n+1} \right]}{2} \\
& -e \frac{\left[ (\Gamma_{e,y})_{i,j+\Delta y/2}^{n+1} + (\Gamma_{e,y})_{i,j-\Delta y/2}^{n+1} \right] \left[ (E_y)_{i,j+\Delta y/2}^{n+1} + (E_y)_{i,j-\Delta y/2}^{n+1} \right]}{2} \\
& - \frac{2m_e}{m_n} \bar{v}_{en} \left[ (n_\varepsilon)_j^{n+1} - \frac{3}{2} (n_e)_j^{n+1} k_B (T_{gas})_j \right] - e \sum_r \Delta E_r^e (R_r N n_e)_j^n.
\end{aligned} \tag{5-5}$$

The fluxes are discretized in a similar fashion as in equation (5-4), giving the following form

$$(\Gamma_{\varepsilon,x})_{i+\Delta x/2,j}^{n+1} = (b_{\varepsilon,x})_{i+\Delta x/2,j}^{n+1} (n_{\varepsilon,x})_{i+\Delta x/2,j}^{n+1} + (n_\varepsilon)_{i,j}^{n+1} \left( \frac{5}{3} u_{i,j} \right). \tag{5-6}$$

The two equations can be written into a matrix system of the form

$$\begin{bmatrix} [K_{11}] & [0] \\ [K_{21}] & [K_{22}] \end{bmatrix} \begin{Bmatrix} \{n_e\} \\ \{n_\varepsilon\} \end{Bmatrix} - \begin{Bmatrix} \{F_e\} \\ \{F_\varepsilon\} \end{Bmatrix} = \begin{Bmatrix} \{0\} \\ \{0\} \end{Bmatrix}, \tag{5-7}$$

$$[K] \{n\} - \{F\} = \{0\}. \tag{5-8}$$

The electron continuity equation in matrix form is constructed by  $[K_{11}]$ ,  $\{n_e\}$ , and  $\{F_e\}$ .  $[K_{11}]$  is the matrix that contains all the factors that will be multiplied by vector  $\{n_e\}$  to discretize the fluxes and the part of the time derivative that is unknown.  $\{n_e\}$  is the vector to be solved that stores the values of  $n_e$ .  $\{F_e\}$  is the vector that contains the source of the electron continuity equation as well as the known part of the time derivative. Similarly,

the electron energy equation is formed by  $[[K_{21}][K_{22}]]$ ,  $\{\{n_e\} \{n_\varepsilon\}\}^T$ , and  $\{F_\varepsilon\}$ . Together, the two equations form the new equation (5-8). The Newton-Raphson non-linear solver for this equation can be written as

$$[K]\{\Delta n\} = -[K]\{n\} + \{F\}. \quad (5-9)$$

where  $\{n\}$  has the values of  $n_e$  and  $n_\varepsilon$  at iteration  $p$ , and  $\{\Delta n\} = \{n\}^{p+1} - \{n\}^p$ . This system of equations is solved using a GMRES numerical matrix solver [85].

### **The Rarefied Gas Module**

The rarefied gas is simulated using equations (4-71) to (4-74), modeled using finite element methods and loosely coupled with the ionized gas module as shown in [Figure 5-1](#). The finite element method (FEM) first gained popularity in the field of structural system analysis in the 1950's [86]. After the development of weighted-residual criteria, it has found new applications in the fields of fluid mechanics and heat transfer [87]. FEM is a popular numerical technique used for solving partial differential equations (PDE's) approximately. Its approach for solving the PDE's is to divide the domain into subdomains called elements. The solution within the element is constructed from the basis functions. This method has several advantages for solving transport problems such as simplicity for dealing with different meshes (e.g. triangular or quadrilateral) and order of elements (e.g. linear or quadratic), which makes it ideal for complex geometries [88]. In addition, complex Neumann (flux) or Robin (convection) boundary conditions are relatively easy to implement.

The numerical simulation of the rarefied gas code is performed using an existing, finite element based module in the Multi-scale Ionized Gas (MIG) flow solver platform developed by Roy et al. [78] [79]. This module of MIG utilizes the Galerkin weak statement combined with the Newton-Raphson nonlinear solver [89]. Bilinear elements are used in the RGC module for the numerical analysis of the RGEJ thruster. In order to provide stability to the solution, the streamline upwinding (SU) artificial diffusion method in 2-D is used (explained in subsection: *Verification of the RGM using plane Poiseuille flow*, for a simpler case) [90]. The MIG flow solver platform had been utilized for many different applications, including electric propulsion, micro-flows, nanoscale flows, fluid dynamics, and plasma physics [80], [81], [82], [83]. Most recently, the finite difference ionized gas module has been added to extend MIG's capabilities.

### Galerkin Weak Statement

The equation system (4-71) to (4-74) for the rarefied gas, can be written in a concise form as

$$L(\mathbf{q}) = \frac{\partial \mathbf{q}}{\partial t} + \frac{\partial(\mathbf{f}_j - \mathbf{f}_j^v)}{\partial x_j} - \mathbf{s} = \mathbf{0}, \quad (5-10)$$

$$1 \leq j \leq 2,$$

$$\mathbf{q} = \begin{pmatrix} \rho \\ \rho u_i \\ \rho c_p T + P \end{pmatrix}, \mathbf{f}_j = \begin{pmatrix} \rho u_j \\ u_j \rho u_i + P \delta_{ij} \\ u_j (\rho c_p T + P) \end{pmatrix}, \mathbf{f}_j^v = \begin{pmatrix} 0 \\ \tau'_{ij} \\ \kappa \frac{\partial T}{\partial x_j} + \tau'_{ij} u_i \end{pmatrix}, \mathbf{s} = \begin{pmatrix} 0 \\ F_i \\ q''' \end{pmatrix}, \quad (5-11)$$

$$1 \leq i \leq 2,$$

$$\tau'_{ij} = \mu \left( \frac{\partial u_i}{\partial x_j} + \frac{\partial u_j}{\partial x_i} \right) + \delta_{ij} \lambda \nabla \cdot \mathbf{V}, \quad (5-12)$$

and  $\delta_{ij} = 1$  if  $i = j$ , else  $\delta_{ij} = 0$ ,

where  $\mathbf{q}$  is the state variable,  $\mathbf{f}$  is the kinetic flux vector,  $\mathbf{f}^v$  the dissipative flux vector and  $s$  is the source term. In this set of equations, the specific heat at constant pressure ( $c_p$ ) is equal to the specific heat at constant volume ( $c_v$ ) minus the gas constant ( $R$ ). The pressure can be set in terms of density and temperature using the ideal gas law, and  $\lambda = -\frac{2}{3}\mu$  based on Stokes' hypothesis.

Any real world smooth problem can be approximated as a Taylor or power series of known functions  $x_j$ . The Galerkin weak statement can be used to construct an approximation to the solution as a series of known spatial function multiplied by a set of unknown expansion coefficients [89]. An approximation for the problem at hand can be constructed as

$$L(\mathbf{q}) = \sum a_i \phi_i(x_j), \quad (5-13)$$

where  $a_i$  are unknown coefficients and  $\phi_i(x_j)$  are known functions of  $x_j$ .

The Galerkin weak statement approach requires the approximation error to vanish in an overall integrated sense. The weak statement, the mathematical expression for minimizing the weighted residual over the domain is

$$WS = \int_{\Omega} wL(\mathbf{q})d\Omega \equiv 0, \quad (5-14)$$

in this equation,  $\Omega$  defines the domain for the problem statement and  $w$  is the weight function set, which is made identical to the corresponding trial function set  $\phi_i$  for the approximation of the state variables. This guarantees that the associated approximation error is a minimum since the error is orthogonal to all basis functions spanning the space of possible Galerkin solutions. The final form of the weak statement formulation becomes

$$WS = \int_{\Omega} \phi_i L(\mathbf{q}) d\Omega \equiv 0. \quad (5-15)$$

When using the Galerkin weak statement, the differentiability requirement for the approximation is “weakened” by one order. For example, the second order terms reduce to first order in the set of equations.

### **Finite Element Basis Function**

As described by Baker et al. [89], the finite element bases are a set of polynomials defined uniformly on every subdivision (finite element) of the solution domain  $\Omega$ , as created by placing nodes as desired for accuracy, and hence constructing the domain discretization denoted as  $\Omega^h$ . The introduction of the discretization  $\Omega^h$  of  $\Omega$  is a central concept of finite element analysis, which greatly simplifies the construction of a wide range of highly suitable trial function sets  $\phi_i(\mathbf{x}_j)$  as well as evaluation of the integrals in the weak statement.

The finite element bases are defined as the set of functions associated with the trial function ( $\phi_i$ ) that span a single generic element  $\Omega_{el}$ . Chebyshev, Lagrange, or Hermite interpolation polynomials can be used as the finite element basis ( $N_k$ ) to the  $k$

degree depending on the problem statement for one, two, or three dimensions. In this study, Lagrange interpolation polynomials are used.

The discrete approximation of the spatially discretized domain (the mesh)  $\Omega^h$  yields a union of elements  $\Omega_{el}$  as

$$\Omega^h = \bigcup_{el} \Omega_{el}. \quad (5-16)$$

Similarly, the integrated variables can be represented as the union of spatially and temporally discretized elements

$$q(t, \mathbf{x}_j) \approx q^h(t, \mathbf{x}_j) = \bigcup_{el} q_{el}(t, \mathbf{x}_j), \quad (5-17)$$

$$q_{el}(t, \mathbf{x}_j) = N_k(\mathbf{x}_j) Q_{el}(t). \quad (5-18)$$

The spatially discretized two-dimensional quadrilateral finite element basis definition yields

$$Q_{el}(\mathbf{x}_j) = \{N_k(\eta_j)\} \{Q_{el}\}, \quad (5-19)$$

where the intrinsic coordinates spanning the quadrilateral  $\Omega_{el}$  constitute the tensor product system  $\{N_k(\eta_j)\}$  [68]. Bilinear bases are chosen for this study (bilinear quadrilateral elements).

## Bilinear Basis

For the bilinear case ( $k = 1$ ) the basis  $\{N_i\}$  must involve polynomials expressible in the global coordinate system  $x_i$  with powers no higher than unity. The geometry of rectangular and straight-sided quadrilateral finite element domains  $\Omega_{el}$  is completely defined by the coordinates of the four intersections (vertices) of the boundary segment generators. Therefore, four expansion coefficients must be involved in the global coordinate equivalent of equation (5-19). The polynomial that involves  $x$  and  $y$  to powers no higher than unity is

$$Q_{el}(x, y) = a_1 + a_2x + a_3y + a_4xy, \quad (5-20)$$

and the  $a_i$  ( $1 \leq i \leq 4$ ) are the to-be-determined expansion coefficients [89]. The fourth term is called the bilinear term since  $xy$  remains linear in both arguments.

To establish the elements of  $\{N_i(\eta_j)\}$ , which is a column matrix of order four in order to match the four entries that must occur in  $Q_{el}$ , the requirement is to equate equations (5-20) and (5-19).

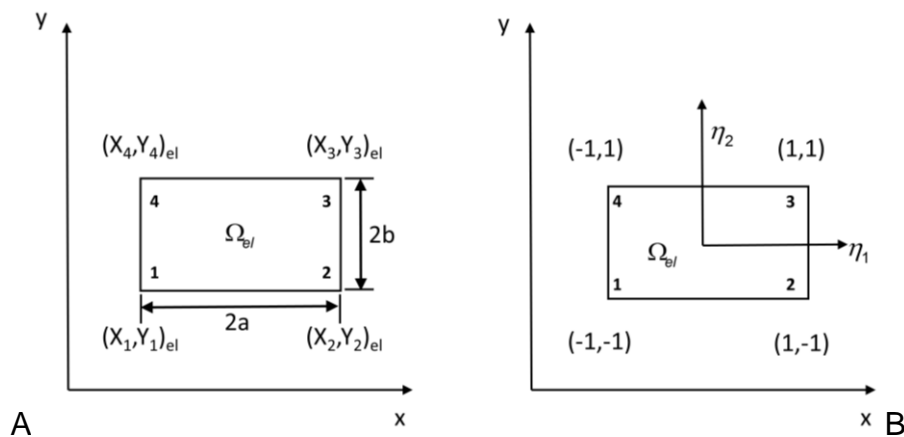


Figure 5-2. Generic rectangular parallelepiped element  $\Omega_{el}$ . A) Element in global coordinate system, and B) in transformed local coordinate system.

With a little insight, one can immediately write down the elements of  $\{N_i\}$  by inspection of [Figure 5-2](#) as [89]

$$\{N_i(\eta_j)\} = \frac{1}{4} \begin{Bmatrix} (1-\eta_1)(1-\eta_2) \\ (1+\eta_1)(1-\eta_2) \\ (1+\eta_1)(1+\eta_2) \\ (1-\eta_1)(1+\eta_2) \end{Bmatrix}. \quad (5-21)$$

The bilinear bases are not restricted to a rectangular parallelepiped finite element. They can be used for any generic straight-sided quadrilateral element with no particular orientation and no sides parallel to each other or to a global coordinate axis. The global element geometry bears no impact whatsoever on the finite element basis description.

The main new difference is the emergence of a nontrivial coordinate transformation between  $(x, y)$  and  $(\eta_1, \eta_2)$ . For all cases, the basis provide the following transformation

$$\begin{aligned} x_{el} &= \{N_k(\eta_j)\} \{X\}_{el}, \\ y_{el} &= \{N_k(\eta_j)\} \{Y\}_{el}. \end{aligned} \quad (5-22)$$

Therefore, the semi-discrete finite element formulation for the problem statement is represented as the *weak statement* ( $WS^h$ )

$$WS^h = S_{el} \left( \int_{\Omega_{el}} N_k L(Q_{el}) d\tau \right) \equiv 0, \quad (5-23)$$

$$\begin{aligned}
WS^h = S_{el} & \left( \int_{\Omega_{el}} N_k \frac{dQ_{el}}{dt} d\tau + \int_{\Omega_{el}} N_k (-s) d\tau - \int_{\Omega_{el}} \frac{dN_k}{dx_j} (f_j - f_j^v) d\tau \right. \\
& \left. + \oint_{d\Omega_{el} \cap d\Omega^h} N_k (f_j - f_j^v) \hat{n}_j d\sigma \right),
\end{aligned} \tag{5-24}$$

Where use of the Green-Gauss divergence theorem exposes the indicated boundary fluxes on  $(d\Omega^h)$ . The  $S_{el}$  symbolizes is the “assembly operator” carrying local matrix coefficients into the global arrays by doing a non-overlapping summation over all the elements. The  $d\tau$  and  $d\sigma$  in the equation differential elements on  $\Omega$  and  $\partial\Omega$ . The differentiation of the basis function depends on both the global and local coordinates

$$\begin{aligned}
\nabla\{N_k\} &= \hat{i} \frac{\partial\{N_k\}}{\partial x} + \hat{j} \frac{\partial\{N_k\}}{\partial y} = \frac{\partial\{N_k\}}{\partial \eta_i} \left( \hat{i} \left( \frac{\partial \eta_i}{\partial x} \right)_{el} + \hat{j} \left( \frac{\partial \eta_i}{\partial y} \right)_{el} \right), \\
1 \leq i \leq 2.
\end{aligned} \tag{5-25}$$

The inverse coordinate transformation, from  $\eta_i$  to  $x_j$ , is required to evaluate the formation of the assembly matrices containing the convection and diffusion information. The transformation, called the Jacobian matrix, is the inverse of the forward transformation

$$[J]_{el} = \left[ \frac{d\eta_i}{dx_j} \right]_{el} = \left[ \frac{dx_j}{d\eta_i} \right]_{el}^{-1}. \tag{5-26}$$

The weak statement naturally yields the surface integrals after the application of the Green-Gauss theorem in equation (5-25), which contains the unknown boundary

fluxes wherever Neumann boundary conditions are enforced. The zero gradient boundary conditions are automatically enforced when the surface integral is removed. The numerical integration method of choice for finite element matrix evaluation is Gaussian quadrature, a variable accuracy procedure that exactly integrates polynomials on regular regions. Specifically, a  $P^{\text{th}}$  – order Gaussian quadrature rule integrates exactly a polynomial of degree  $2P-1$  on  $\Omega_{el}$  in transform space, that is, the unit square as explained on page 219 of Baker et al. [89]. For a linear problem statement and bilinear elements the product of all terms forming each element of the element matrix can be no more than cubic in  $\eta_i$ . Thus,  $P = 2$  Gaussian quadrature rule is appropriate since  $2P-1 = 3$  (cubic polynomial) in this case. For this study, the problem statement is nonlinear and a ( $P = 3$ ) Gaussian quadrature is used.

### Newton-Raphson Scheme

The semi-discretized weak statement ( $WS^h$ ) of equation (5-23) always yields an ordinary differential equation (ODE) system of the following form

$$WS^h = S_{el} \left( M_{el} \frac{dQ}{dt} + \mathfrak{R}_{el}(Q) \right) = M \frac{dQ}{dt} + \mathfrak{R}(Q) \equiv \{0\}, \quad (5-27)$$

where  $Q$  is the time-dependent finite element nodal vector,  $M = S_{el}(M_{el})$  is the mass matrix associated with element level interpolation, and  $\mathfrak{R}(Q)$  carries the element convection information, the diffusion matrix, and all known data.

A  $\theta$ -implicit time integration procedure is used (for all cases shown in this study  $\theta = 1.0$ , meaning that the implicit first-order Euler time stepping method is employed) and the terminal ODE is usually solved using the Newton-Raphson scheme:

$$\begin{aligned} Q_{n+1} &= Q_n + \Delta t \left[ (\theta) \left( \frac{\partial Q}{\partial t} \right)_{n+1} + (1-\theta) \left( \frac{\partial Q}{\partial t} \right)_n \right] \\ &= Q_n - \Delta t (M^{-1}) [(\theta) \mathfrak{R}_{n+1} + (1-\theta) \mathfrak{R}_n], \end{aligned} \quad (5-28)$$

$$F = M(Q_{n+1} - Q_n) + \Delta t [(\theta) \mathfrak{R}_{n+1} + (1-\theta) \mathfrak{R}_n] = 0, \quad (5-29)$$

$$-F_{n+1}^p = J(\delta Q)^{p+1}, \quad (5-30)$$

$$J = \frac{\partial F}{\partial Q} = M + \theta \Delta t \left( \frac{\partial \mathfrak{R}}{\partial Q} \right), \quad (5-31)$$

$$(\delta Q)^{p+1} = - \left[ M + \theta \Delta t \left( \frac{\partial \mathfrak{R}}{\partial Q} \right) \right]^{-1} F, \quad (5-32)$$

$$Q_{n+1}^{p+1} \equiv Q_{n+1}^p + (\delta Q)^{p+1} = Q_n + \sum_{i=0}^p (\delta Q)^{i+1}, \quad (5-33)$$

where the subscript  $n$  represents the time level and  $p$  the iteration index of the Newton-Raphson scheme. Equation (5-28) uses the substitution of equation (5-27) solved for  $\partial Q/\partial t$ . Equation (5-29) is found by moving all the terms of (5-28) to the left-hand side, but  $F$  is only equal to zero at steady state. Equation (5-30) is the Newton algorithm for (5-29), where the Newton Jacobian definition ( $J$ ) given as (5-31) is obtained as a direct result of (5-30). Equations (5-32) and (5-33) show the Newton-Raphson scheme for the FEM and how the solution at the new sub-iteration is recovered.

The solution is declared convergent when the  $L^2$ -norms of the residual and solution for each of the state variables becomes smaller than a chosen convergence

criterion. The criterion for the  $L^2$ -norms of the solution is given in the introduction of this chapter and the criterion for the  $L^2$ -norms of the residual is not enforced since it is not as restrictive as the  $L^2$ -norms of the solution for the cases studied.

### Decoupled Heat Transfer Codes

#### Conduction Numerical Code

The Laplace equation (4-90) is used to solve the heat transfer through conduction using the finite element module of the MIG platform where

$$L(\mathbf{q}) = \frac{\partial \mathbf{q}}{\partial t} + \frac{\partial(\mathbf{f}_j - \mathbf{f}_j^v)}{\partial \mathbf{x}_j} - \mathbf{s} = \mathbf{0}, \quad (5-34)$$

$$1 \leq j \leq 2,$$

$$\mathbf{q} = (\rho c_p T), \mathbf{f}_j = (0), \mathbf{f}_j^v = \left( \kappa \frac{\partial T}{\partial \mathbf{x}_j} \right), \mathbf{s} = (0), \quad (5-35)$$

$$1 \leq i \leq 2,$$

similarly to the rarefied gas module in the section labeled as *The Rarefied Gas Module*.

In this equation, the time derivative vanishes at steady state.

#### Thermal Radiation Heat Transfer Numerical Code

In order to model the thermal radiation heat loss, equation (4-84) can be rewritten in terms of vectors and matrices as

$$\sum_{j=1}^N \left[ \frac{\delta_{ij}}{\varepsilon_j} - \left( \frac{1}{\varepsilon_j} - 1 \right) F_{i-j} \right] \mathbf{q}_j = \sum_{j=1}^N \left[ \delta_{ij} - F_{i-j} \right] E_{bj} - H_{oi}, \quad (5-36)$$

$$\begin{aligned}
\bar{C} \cdot \bar{q} &= \bar{A} \cdot \bar{E}_b - \bar{H}_o, \\
C_{ij} &= \frac{\delta_{ij}}{\varepsilon_j} - \left( \frac{1}{\varepsilon_j} - 1 \right) F_{i-j}, \\
A_{ij} &= \delta_{ij} - F_{i-j},
\end{aligned} \tag{5-37}$$

and solved by matrix inversion as

$$\bar{q} = \bar{C}^{-1} \cdot \left[ \bar{A} \cdot \bar{E}_b - \bar{H}_o \right]. \tag{5-38}$$

For the open surfaces of the rectangular prism form by the channel of the micro-thruster, an artificial surface is used to close the openings. Since any radiation leaving the cavity will not come back, barring any reflection from other surfaces nearby, the artificial surface must be black. In addition, the artificial surface is not emitting. These criteria are satisfied by making the artificial surface a black body at zero Kelvin [76]. The external irradiation is assumed negligible to obtain the highest possible heat loss. The matrix inversion in (5-38) is solved using MATLAB [91].

CHAPTER 6  
BENCHMARKING AND VALIDATION

**Ionized Gas Module (IGM)**

**Verification and Grid Convergence Study of the IGM**

In order to verify the plasma module, the veracity of the model was tested using the method of manufactured solutions with the same procedure as Houba [54]. A solution to a 1-D drift-diffusion equation with variable transport coefficients is developed as described in this subsection. The test equation is

$$\begin{aligned}\frac{\partial n}{\partial t} + \frac{\partial \Gamma_x}{\partial x} &= S, \\ \Gamma_x &= nV - D \frac{\partial n}{\partial x},\end{aligned}\tag{6-1}$$

where  $V$  is the drift velocity equivalent to  $Z\mu E_x$  and  $D$  is the diffusion coefficient. Both are defined to vary in space using a polynomial expression

$$\begin{aligned}D &= C_1 x^3 + C_2 x^2 + C_3 x + C_4, \\ V &= C_5 x^3 + C_6 x^2 + C_7 x + C_8.\end{aligned}\tag{6-2}$$

The constant  $C_8$  is set to zero for convenience to ensure  $V(x=0)$  is equal to zero, which is useful for Neumann boundary conditions. Two types of boundaries are tested, Neumann and Dirichlet boundaries, to test the discretization scheme. The boundaries are given as

$$\begin{aligned}\Gamma_x|_{x=0} &= 0, \\ n(x=1) &= A + B,\end{aligned}\tag{6-3}$$

where A and B are constants. A simple form for  $n$  that satisfies these boundary conditions is

$$n = Ax^2 + B.\tag{6-4}$$

The solution is manufacture by solving for a source term  $S$  that will produce equation (6-4) as the exact steady-state solution to the governing equation (6-1). The source term obtained after substituting the solution for  $n$  in the governing equations is [54]

$$S = \left\{ \begin{aligned} &5AC_5x^4 + (4AC_6 - 8AC_1)x^3 + \\ &3(AC_7 + BC_5 - 2AC_2)x^2 + \\ &2(BC_6 - 2AC_3)x + (BC_7 - 2AC_4) \end{aligned} \right\}.\tag{6-5}$$

Two cases were tested for the verification. In these cases, the magnitude of  $V$  is different by a factor of a thousand to test the behavior of the scheme in a region of high electric field, where the drift flux dominates over the diffusion flux. The coefficients for each case are given in [Table 6-1](#).

The accuracy of the solution was calculated using the  $L_1$ -norm defined as

$$\|E\|_1 = \frac{1}{N} \sum_{i=1}^N |n_i - n_{exact,i}|,\tag{6-6}$$

where  $N$  is the number of nodes in the mesh.

Table 6-1. Coefficients for the grid refinement study [54].

Coefficients	Case 1	Case 2
A	-3	-3
B	4	4
C <sub>1</sub>	1	1
C <sub>2</sub>	1	1
C <sub>3</sub>	1	1
C <sub>4</sub>	1	1
C <sub>5</sub>	2	2000
C <sub>6</sub>	2	2000
C <sub>7</sub>	3	3000
C <sub>8</sub>	0	0

The following figure shows the analysis of the convergence of the method.

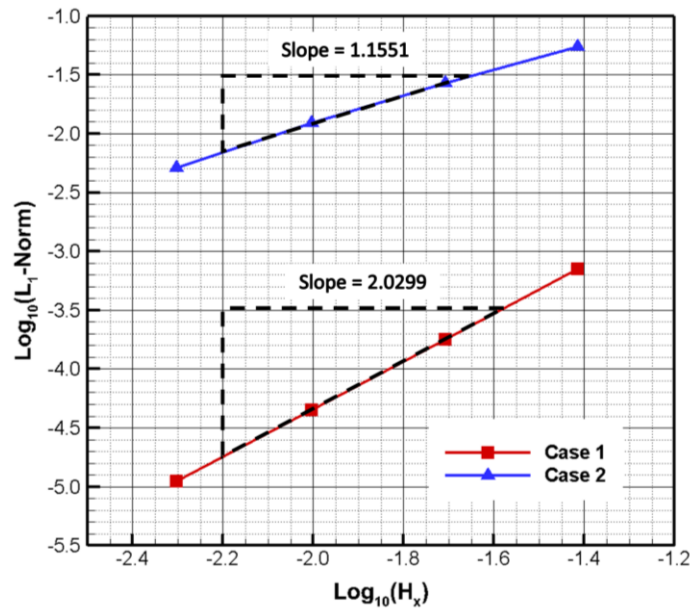


Figure 6-1. Order of accuracy for Scharfetter-Gummel flux discretization scheme for Case 1 and Case 2.

The Scharfetter-Gummel flux discretization scheme behaves as expected, similar to the study done by Houba [54]. If the drift velocity is low (low electric field), the diffusion-flux dominates and the scheme is second order. The logarithm of the L<sub>1</sub>-Norm increases as the logarithm of the distance between node increases with a slope of ~2.03 in a linear manner. If the drift velocity is high enough for the drift-flux to dominate,

then the scheme decreases to first order accurate with a slope of  $\sim 1.16$ . An important finding obtained from the convergence analysis is that the order of accuracy of the Neumann boundary affects the convergence of the entire simulation. If the boundary discretization scheme is first order, the solution is first order even when the diffusion-flux dominates. The Scharfetter-Gummel flux discretization scheme is used in this dissertation for its computational speed advantage and numerical stability. The Neumann boundaries are discretized using a second order scheme. The continuity equations for all particles and the electron energy equation used in this dissertation have the same form as the equation tested in this grid convergence study; therefore by verifying the discretization scheme of a single equation with a generic form, the plasma module is verified. The Poisson equation is always second order and its discretization was also tested using the method of manufactured solution, but its analysis was not included since it reaches maximum convergence with a smaller number of nodes than the drift-diffusion equations.

### **Validation of the IGM**

Additionally, a simulation in 1-D of a parallel-plate, capacitively coupled, low-pressure, symmetric RF discharge driven at 13.56 MHz was performed and compared with Godyak et al. [92]. Although the RGEJ cases in this study use a DC applied potential difference, the RF discharge experiment of Godyak et al. [92] is employed for this validation since the numerical models used for RF and DC glow discharges are almost identical except for the applied alternating voltage in RF discharges. In previous studies, Sitaraman and Raja [66] and Deconinck [11] have successfully used the LMEA

model to investigate an RF discharge thruster and a DC discharge thruster, respectively.

Godyak et al. [92] measured the discharge electrical characteristics (voltage, current, etc.) using argon (99.998% purity) at low pressure inside a glass cylinder with inner diameter of 14.3 (cm), cross-section area = 160 (cm<sup>2</sup>), and a discharge gap formed by the two parallel-plate aluminum electrodes of 6.7 (cm). The discharge separation was chosen to be large enough that “collisionless” discharges at pressures as low as 3.0 (mTorr) could be studied without overlapping electrode sheaths, and small enough that it could be considered as a 1-D discharge. For the cases shown, the pressure was 1.0 (Torr) and temperature of 300 K was assumed. The computational grid for all cases tested was composed of 671 nodes equally spaced.

The secondary electron emission ( $\gamma_{sec}$ ) depends sensitively on surface conditions, morphology, impurities, and contamination; the commonly assumed value for ( $\gamma_{sec}$ ) for pure aluminum in a DC discharge is 0.1 [41]. Since in Godyak et al [92], the purity of the aluminum or its surface condition are not given and the discharge is not DC, several values of ( $\gamma_{sec}$ ) were tested to validate the code. The discharge voltage amplitude is applied to each electrode with equal magnitude but opposite phase. The peak-to-peak voltage is the total voltage of the simulation at peak value. [Figure 6-2](#) shows the comparison between the experimental values and three different numerical simulations performed with different ( $\gamma_{sec}$ ).

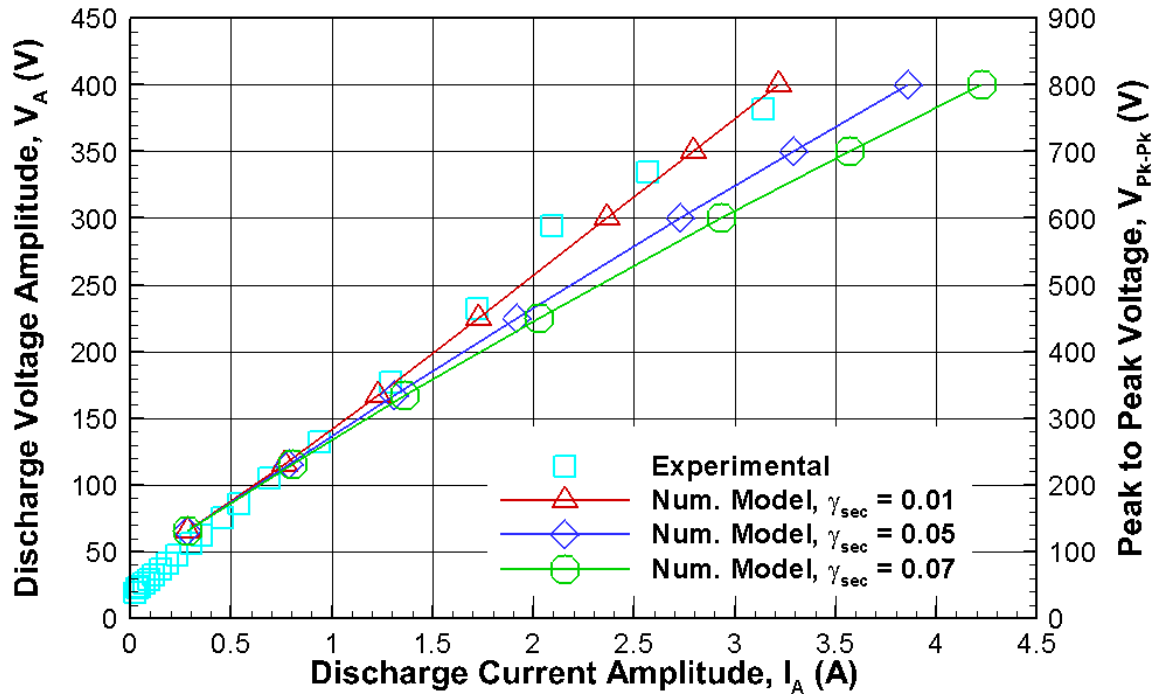


Figure 6-2. Comparison between numerical model and experiment [92].

The cases with ( $\gamma_{sec}$ ) equal to 0.01 matched the experimental results with the least error as shown in the following table.

Table 6-2. Comparison between experiment [92] and numerical model with ( $\gamma_{sec}=0.01$ ) for ( $300\text{ V} < V_{PK-PK} < 800\text{ V}$ ).

Current Amplitude	Experiment Data Voltage Amplitude	Numerical Model ( $\gamma_{sec}=0.01$ ) Voltage Amplitude	Percent Error
$I_A$ (A)	$V_A$ (A)	$V_A$ (A)	Error (%)
1.229	169.2	167.5	1.03
1.726	233.0	225.0	3.44
2.366	317.6	300.0	5.53
2.795	353.5	350.0	1.00
3.214	388.1	400.0	3.07

A linear interpolation was used to interpolate between the experimental data points and to calculate the voltage amplitude at the given current amplitude obtained from the numerical model. The maximum percent error of the voltage amplitude in the

range of interest for the peak-to-peak voltage (300 to 800 V) is 5.53% for ( $\gamma_{sec}$ ) equal to 0.01, a reasonable error by drift-diffusion model standards. Drift-diffusion models typically have relatively large errors due to inaccuracies in the input coefficients as well as the model's inherent approximation of the Boltzmann equation. For example, the variation in the reduced mobility ( $\mu_e n_n$ ) when using different collision cross-section libraries, in a Boltzmann solver such as BOLSIG+, for the electron mean energy (7-10 eV) region is of ~5% [44].

### Rarefied Gas Module (RGM)

#### Verification of the RGM using plane Poiseuille flow

A verification of the RGM is performed using a simple case of plane Poiseuille flow. Since the fluid dynamic solver used in the RGM is a multi-physics code that could be used to solve a variety of problems, a plane Poiseuille flow is used to test the implementation of the same derivatives and artificial diffusion method that are used to solve the rarefied gas equations.

The incompressible Navier-Stokes equations are used for the plane Poiseuille flow case, which can be written in non-dimensional form as [54]

$$\nabla \cdot \mathbf{u} = 0, \tag{6-7}$$

$$\frac{\partial \mathbf{u}}{\partial t} + (\mathbf{u} \cdot \nabla) \mathbf{u} = -\nabla P + \frac{1}{\text{Re}} \nabla^2 \mathbf{u}. \tag{6-8}$$

In an incompressible flow, the pressure waves must propagate at an infinite speed. This type of behavior is not a trivial task to numerically model. In order to solve

this problem, the continuity equation is modified by adding a time derivative of the pressure multiplied by the inverse of a compressibility factor ( $\beta$ ), which introduces a finite speed for the pressure disturbances to propagate through the domain. This approach is called the artificial compressibility method [93], and it produces a modified continuity equation given as

$$\frac{1}{\beta} \frac{\partial P}{\partial t} + \nabla \cdot \mathbf{u} = 0. \quad (6-9)$$

At steady-state, the additional term vanishes and the original continuity equation is recovered.

Additionally, the equations require an artificial diffusion method for numerical stability purposes. As explained in the section labeled as *The Rarefied Gas Module*, the streamline upwinding (SU) artificial diffusion method in 2-D is used [90]. For the cases in this dissertation, where only rectangular, bilinear elements are used and the velocity components ( $u_1 = u$ ,  $u_2 = v$ ) are defined in the same direction as the axes ( $x$ ,  $y$ ), respectively, the artificial diffusion tensor ( $\bar{\bar{v}}$ ) is

$$v_{ij} = \bar{\bar{v}} \frac{|u_i u_j|}{|\mathbf{u}|^2}, \quad (6-10)$$

$$1 \leq i \leq 2 \text{ and } 1 \leq j \leq 2,$$

where  $\mathbf{u}$  is the velocity vector and

$$\bar{v} = \frac{1}{2}(\alpha_x |u_1| h_x + \alpha_y |u_2| h_y),$$

$$\alpha_x = \coth(Pe_x) - 1/Pe_x, \alpha_y = \coth(Pe_y) - 1/Pe_y, Pe_x = \frac{|u_1| h_x}{(2/Re)}, Pe_y = \frac{|u_2| h_y}{(2/Re)}. \quad (6-11)$$

The modified incompressible Navier-Stokes equations are

$$\frac{1}{\beta} \frac{\partial P}{\partial t} + \nabla \cdot \mathbf{u} - [\nabla \cdot (\bar{v} \cdot \nabla)] P = 0, \quad (6-12)$$

$$\frac{\partial \mathbf{u}}{\partial t} + (\mathbf{u} \cdot \nabla) \mathbf{u} + \nabla P - \frac{1}{Re} \nabla^2 \mathbf{u} - [\nabla \cdot (\bar{v} \cdot \nabla)] \mathbf{u} = 0. \quad (6-13)$$

These modified equations approached the original equations at steady-state with grid refinement. The system of equations are solved with the same approach explained in the section labeled as *The Rarefied Gas Module*, where the equations can be written in a concise form as

$$L(\mathbf{q}) = \frac{\partial \mathbf{q}}{\partial t} + \frac{\partial (f_j - f_j^v)}{\partial x_j} - s = 0, \quad (6-14)$$

$$1 \leq j \leq 2,$$

$$f_j^v = \left( \begin{array}{c} \frac{\bar{v}}{|\mathbf{u}|^2} \left( |u_j u_j| \frac{\partial P}{\partial x_j} + |u_j u_{(3-j)}| \frac{\partial P}{\partial x_{(3-j)}} \right) \\ \frac{1}{Re} \left( \frac{\partial u_i}{\partial x_j} \right) + \frac{\bar{v}}{|\mathbf{u}|^2} \left( |u_j u_j| \frac{\partial u_i}{\partial x_j} + |u_j u_{(3-j)}| \frac{\partial u_i}{\partial x_{(3-j)}} \right) \end{array} \right), \quad (6-15)$$

$$\mathbf{q} = \left( \begin{array}{c} P \\ \beta \\ u_i \end{array} \right), f_j = \left( \begin{array}{c} u_j \\ u_j u_i + P \delta_{ij} \end{array} \right), s = \left( \begin{array}{c} 0 \\ 0 \end{array} \right), \text{ and } 1 \leq i \leq 2,$$

similarly to the rarefied gas equations.

The plane Poiseuille flow case studied consists of a channel form by two parallel plates with a pressure difference between its inlet and outlet.

The following figure shows its geometry and the boundary conditions used in the numerical simulation.

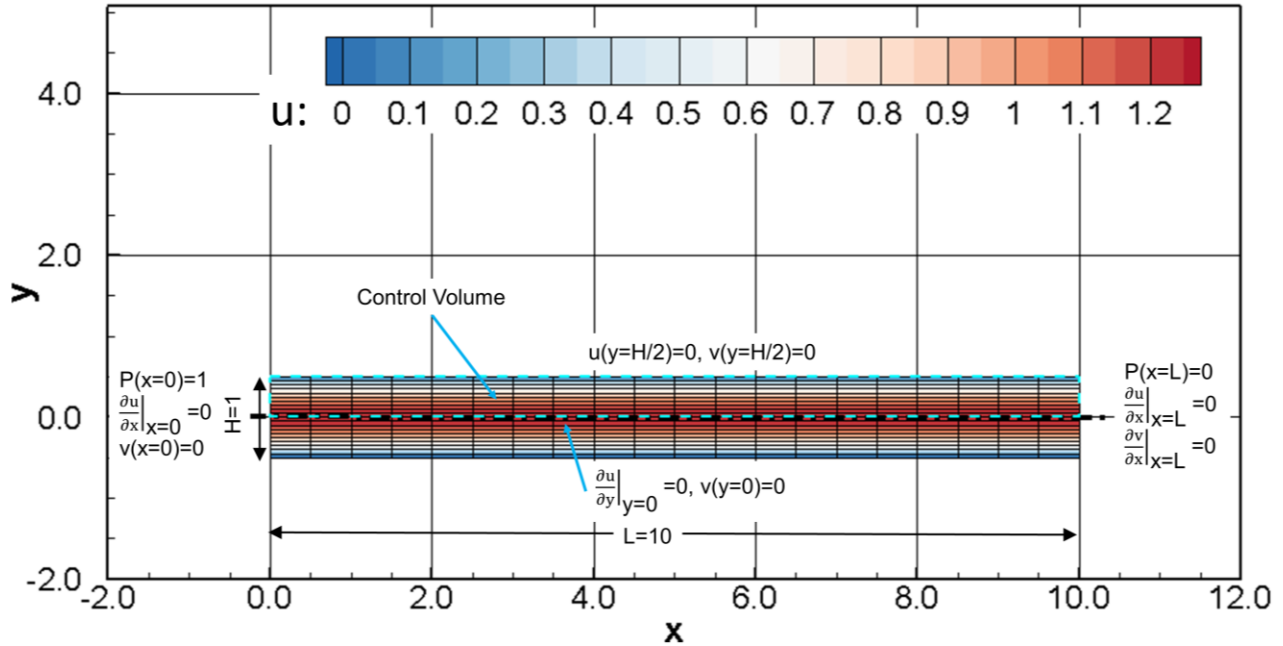


Figure 6-3. Plane Poiseuille flow in a ( $L=10, H=1$ ) channel with a ( $Re = 100$ ) using a ( $21 \times 11$ ) nodes mesh. All variables are non-dimensional and only half of the domain is numerically simulated due to symmetry.

For this simulation,  $Re$  and  $\beta$  were set equal to 100. Three different meshes were tested: ( $21 \times 11$ ), ( $41 \times 21$ ), and ( $81 \times 41$ ) nodes.

The test revealed the solution was mesh independent. Plane Poiseuille flow has an analytical solution assuming the flow is steady-state and fully developed. The analytical solution is

$$u(y) = \frac{\left(-\frac{\partial P}{\partial x}\right)}{\left(\frac{2}{\text{Re}}\right)} \left(y + \frac{H}{2}\right) \left(\frac{H}{2} - y\right),$$

where  $\frac{\partial P}{\partial x} = \frac{P_{\text{Outlet}} - P_{\text{Inlet}}}{L} = \left(\frac{0.0 - 1.0}{10.0}\right) = -0.1$  and  $\frac{\partial P}{\partial y} = 0,$  (6-16)

$$v(x, y) = 0,$$

$$P(x) = \left(\frac{\partial P}{\partial x}\right) x + P_{\text{Inlet}},$$

for  $0 \leq x \leq L,$  and  $-\frac{H}{2} \leq y \leq \frac{H}{2}.$

The comparison between the analytical and numerical solutions shows near perfect agreement. For the x-component of velocity ( $u$ ), the  $L_1$ -norm is  $\sim 3.14 \times 10^{-8}$  and the  $L_\infty$ -norm is  $\sim 5.70 \times 10^{-8}$ , where the  $L_1$ -norm and the  $L_\infty$ -norm are defined as

$$\|E\|_1 = \frac{1}{N} \sum_{i=1}^N |u_i - u_{\text{analytical},i}|,$$

$$\|E\|_\infty = \max |u_i - u_{\text{analytical},i}|,$$
(6-17)

respectively, and  $N$  is the number of nodes of the mesh. The discrepancy between the analytical and the numerical solutions for the pressure ( $P$ ) and the y-component of velocity ( $v$ ) are smaller than for  $u$ , therefore they are not shown.

### **Benchmarking/Validation of the RGM**

In this section, a benchmarking of the rarefied gas module is done for subsonic gas flows through a micro-channels using results from Chen et al. [94], which were validated within 1.15% accuracy with experimental results of Pong et al. [95]. The model assumes the gas flows through two parallel plates of length ( $L = 3000 \mu\text{m}$ ) and width ( $W$

= 40  $\mu\text{m}$ ) separated by a distance ( $H = 1.2 \mu\text{m}$ ). The end effects are neglected and only the two-dimensional geometry stretching in the  $x$  and  $y$  directions is considered.

Table 6-3. Microchannel Properties of Fluid for Subsonic Gas Flows [94].

<b>Fluid</b>	<b>P<sub>in</sub>/P<sub>out</sub></b>	<b>P<sub>out</sub></b>	<b>T<sub>in</sub></b>	<b>T<sub>w</sub></b>	<b><math>\mu</math></b>	<b><math>\kappa</math></b>	<b><math>\gamma</math></b>	<b>R</b>
	-	(kPa)	(K)	(K)	(Pa-s)	(W/m-K)	-	(J/kg-K)
N <sub>2</sub>	2.701	100.8	314	314	$1.85 \times 10^{-5}$	0.0259	1.4	296.7

In the previous table,  $T_{in}$  is the inlet gas temperature and  $T_w$  is the isothermal wall temperature.  $P_{in}/P_{out}$  is the ratio of inlet pressure vs. outlet pressure. All other parameters and boundary conditions are given by Chen et al. [94]. The inlet and outlet pressures produce Knudsen numbers of 0.0217 and 0.0585, respectively. The flow in the microchannel is in the slip flow regime, which is the regime of interest for this study. The following table shows the grid dependence test done by Chen et al. [94].

Table 6-4. Grid dependence test of the centerline  $u$ -velocity (m/s) at different  $x$ -locations [94].

<b>Grid</b>	<b>x = 500</b>	<b>x = 1000</b>	<b>x = 1500</b>	<b>x = 2000</b>	<b>x = 2500</b>
	( $\mu\text{m}$ )				
1500x7	0.4765853	0.5225323	0.5845432	0.6745498	0.8216915
3000x13	0.4760927	0.5222115	0.5845377	0.6749501	0.8229470
6000x23	0.4759963	0.5222144	0.5845423	0.6749584	0.8229740

Table 6-5. Grid dependence test done using MIG of the centerline  $u$ -velocity (m/s) at different  $x$ -locations.

<b>Grid</b>	<b>x = 500</b>	<b>x = 1000</b>	<b>x = 1500</b>	<b>x = 2000</b>	<b>x = 2500</b>
	( $\mu\text{m}$ )				
1500x7	0.47601	0.52127	0.58127	0.66794	0.80982
3000x13	0.47606	0.52127	0.58126	0.66798	0.80984
6000x23	0.47620	0.52111	0.58124	0.66794	0.80988

The maximum discrepancy between Chen et al. [94] and our results, in the  $u$ -velocity at the centerline, occurs at  $x = 2500 \mu\text{m}$ . This maximum discrepancy of 1.6 %

can be attributed to using different values of thermal conductivity and different numerical schemes. Chen et al. [94] did not provide the thermal conductivity and explicit finite difference method was used to solve the governing equations. The pressure discrepancy along the centerline is similar to the u-velocity discrepancy. Exact values for the pressure along the centerline are not given in Chen et al. [94], only a figure is provided, therefore an exact comparison of the pressure is not performed. The temperature remains near constant throughout the domain ( $\sim T_w=314$  K), and the v-velocity is close to zero. Overall, the rarefied gas module matched closely with results in literature.

A comparison between the experimental results for the pressure at the centerline from Pong et al. [95] given in Chen et al. [94] are provided in the following table.

Table 6-6. Comparison of centerline pressure ratios at different x-locations [95].

<b>x/L</b>	<b>Pong et al.</b>	<b>MIG (6000x23 Nodes)</b>	<b>Relative Error (%)</b>
	<b>P/P<sub>out</sub></b>	<b>P/P<sub>out</sub></b>	
0.102841	2.559144	2.571570	0.485558
0.351046	2.243178	2.231138	0.536748
0.601134	1.831036	1.837706	0.364236
0.858915	1.376518	1.343269	2.415414

The maximum difference occurs closer to the exit of the channel, while Chen et al. [94] overshoots the solution by 1.15%, the MIG code solution is lower than the experimental value by 2.4%. This discrepancy could be due to the different viscosity  $1.8540724 \times 10^{-5}$  (Pa-s) and thermal conductivity (0.02675 W/m-K) at gas temperatures of  $\sim 314.01$  K found at the given data point in the experimental solution.

## CHAPTER 7 CASES STUDIED

### Geometry and Grid

The micro-thruster was designed with a long (20 mm), narrow (3 mm) slot to prevent the possibility of catastrophically plugging the thruster's throat as shown in the following figure.

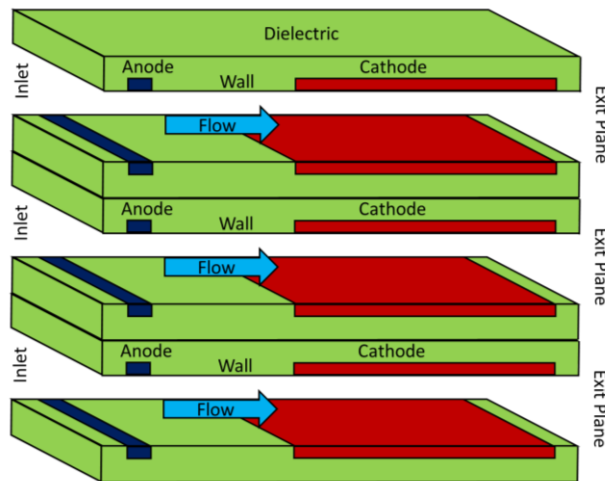


Figure 7-1. Geometry and design of the RGEJ thruster using several stack slots similarly to the FMMR thruster.

The absence of an expansion nozzle at the exit of the channel is due to predicted low Reynolds numbers ( $< 100$ ). In the limit of continuum isentropic flow through a large pressure drop, the nozzle's thrust is proportional to the operating pressure and the throat area [4]

$$F_{\text{Thrust}} \propto P_0 A_t \propto P_0 W H, \quad (7-1)$$

where  $W$  and  $H$  are width and height.

The Reynolds number gives a measure of nozzle efficiency in terms of viscous flow losses. The nozzle's Reynolds number at the throat is given by [4]

$$\text{Re} = \frac{\rho a H}{\mu} \propto \frac{P_0 H}{T_0^\beta}, \text{ where } (1.2 < \beta < 1.5) \text{ and } a = \sqrt{\gamma R T}. \quad (7-2)$$

For the nozzle's viscous losses to scale favorably, the Reynolds number must remain constant or increase as the device is miniaturized [4]. Since small satellites require lower thrust and cannot operate at high enough plenum pressures, the operational Reynolds number for micro-nozzles may decrease to values as low as 100, and as heat is added, the flow experiences a further decrease in Reynolds number. Micro-thrusters with low throat Reynolds number (~100) do not experience any gains from an expansion nozzle [96]. The low plenum-pressure operation condition is chosen to scale the thrust and for the additional benefit of reduced propellant storage pressure, therefore easing the propellant tank mass and valve leakage requirements [4].

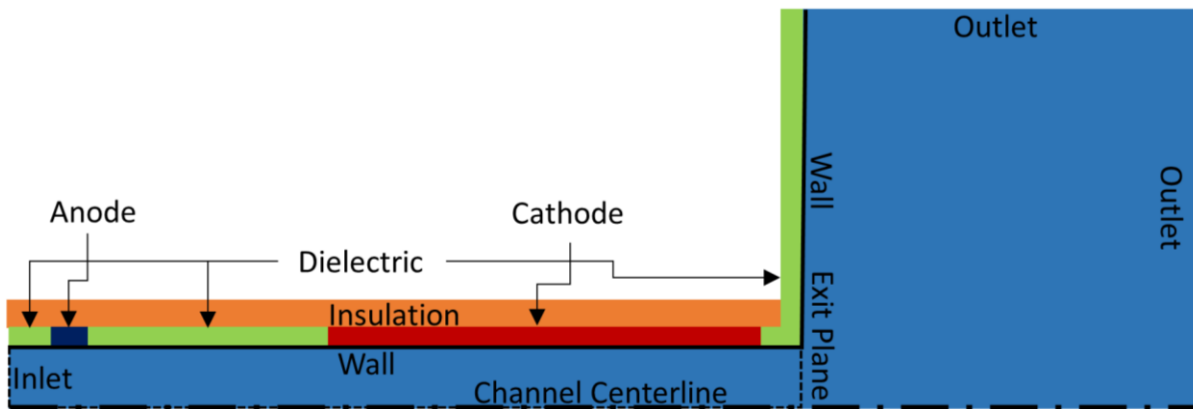


Figure 7-2. Domain region of the RGEJ numerically simulated.

Figure 7-2 shows the domain region numerically simulated (light blue). The IGM module models only the region inside the channel, ( $0 \text{ mm} < x < 20 \text{ mm}$ ), since the charged particle number densities are negligible at the exit plane. The mesh inside the channel has  $401 \times 31$  nodes. For the cases tested, the anode is between ( $1 \text{ mm} < x < 2 \text{ mm}$ ) and the cathode ( $8 \text{ mm} < x < 19 \text{ mm}$ ). The RGM module models the channel region and the plume. The plume has  $201 \times 201$  nodes and is  $10 \times 10$  (mm). All cells are rectangular and have constant  $\Delta x$  and  $\Delta y$ . It is only necessary to solve one-half of the domain due to symmetry.

### Cold gas thruster and constant thermal heating source thrusters' results and comparison

In order to understand the effect of gas heating in the RGEJ, results for adiabatic wall condition cases with different constant volumetric thermal heating source values,  $q''' = 1.0, 2.0, 3.0,$  and  $4.0$  ( $\text{MW}/\text{m}^3$ ), were obtained and compared with a cold gas thruster of the same design. The cold gas thruster simulation with ( $q''' = 0.0 \text{ MW}/\text{m}^3$ ) is called the *base case*.

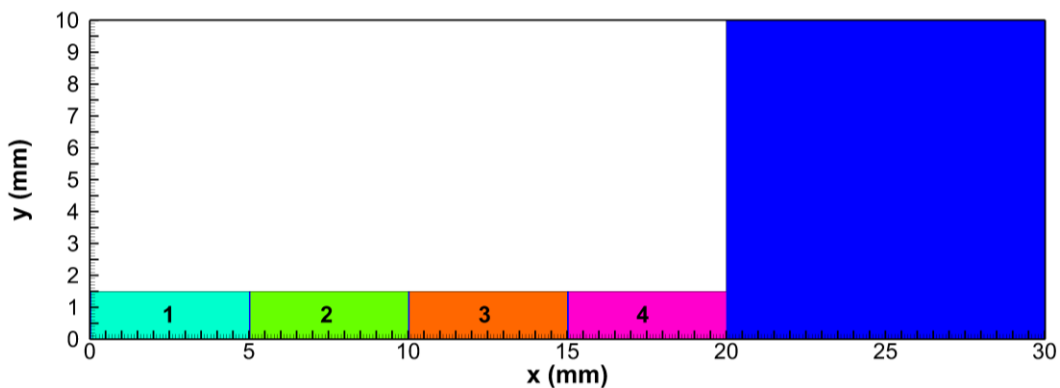


Figure 7-3. Regions of applied  $q'''$ . Only half of the domain is shown. The value of  $q'''$  is constant over the given region. The four regions in the domain where  $q'''$  was applied are shown and labeled 1-4.

The performance parameters in this study are calculated at the exit plane of the thruster using the following set of equations.

$$\begin{aligned}
 \dot{Q} &= 2 \int_0^{H/2} \int_0^L (q''') W dx dy, \\
 \dot{m} &= 2 \int_0^{H/2} (\rho u) W dy, \\
 F_{\text{Thrust}} &= 2 \int_0^{H/2} (\rho u^2 + P) W dy, \\
 F_{\tau_{\text{Wall}}} &= 2 \int_0^L (\tau_{\text{Wall}}) W dx, \text{ where } \tau_{\text{Wall}} = -\mu \left. \frac{\partial u}{\partial y} \right|_{y=H/2}, \\
 I_{sp} &= \frac{F_{\text{Thrust}}}{\dot{m} g_0}, \text{ where } g_0 = 9.81 \text{ (m/s}^2\text{) and } W = 1 \text{ (cm)}, \\
 I_{sp} \text{ Inc.} &= \frac{(I_{sp} - I_{sp, \text{ base case}})}{I_{sp, \text{ base case}}} \cdot 100, \\
 M_{\text{Exit}} &= \frac{|\vec{V}_{\text{Exit}}|}{\sqrt{\gamma R T_{\text{Exit}}}} \approx \frac{u_{\text{Exit}}}{\sqrt{\gamma R T_{\text{Exit}}}}, \\
 Kn_{\text{Exit}} &= \frac{16\mu}{(5\rho\sqrt{2\pi RT})H} \Bigg|_{\text{Exit}},
 \end{aligned} \tag{7-3}$$

The following table shows the performance parameters of the different cases studied using a constant  $q'''$  over the four different regions shown in [Figure 7-3](#). The integrated value of  $q'''$  over the volume is called the total thermal heating source ( $\dot{Q}$ ). Four different  $\dot{Q}$  were tested. These values are 150, 300, 450 and 600 (mW). The mass flow rate, given in SCCM, is calculated by the program and depends on the pressure difference between the inlet and outlet.

Table 7-1. Values of total thermal heating source ( $\dot{Q}$ ), mass flow rate ( $\dot{m}$ ), thrust ( $F_{Thrust}$ ), shear force ( $F_{\tau_{Wall}}$ ), specific impulse ( $I_{sp}$ ), specific impulse increase ( $I_{sp} \text{ Inc.}$ ) compared to the *base case*, exit plane Mach number ( $M_{Exit}$ ) at the centerline, and exit Knudsen number ( $Kn_{Exit}$ ) at the centerline are displayed. The unit (SCCM) means cubic centimeter per minute at STP<sup>b</sup>.

Case	Region of Applied $\dot{Q}$ as shown in Figure 7-3	$\dot{Q}$ (mW)	$\dot{m}$ (SCCM)	$F_{Thrust}$ (mN)	$F_{\tau_{Wall}}$ (mN)	$I_{sp}$ <sup>a</sup> (s)	$I_{sp} \text{ Inc.}$ (%)	$M_{Exit}$ -	$Kn_{Exit}$ -
<i>Base case</i>	None	0	180.3	2.288	1.955	44.11	-	1.192	0.046
<i>Case Q1-150</i>	1	150	149.9	2.069	2.112	48.00	8.82	1.138	0.063
<i>Case Q1-300</i>	1	300	120.3	1.841	2.298	53.21	20.64	1.056	0.089
<i>Case Q1-450</i>	1	450	91.0	1.600	2.516	61.15	38.65	0.924	0.133
<i>Case Q1-600</i>	1	600	62.1	1.370	2.746	76.65	73.79	0.722	0.208
<i>Case Q2-150</i>	2	150	154.6	2.145	2.046	48.24	9.38	1.143	0.061
<i>Case Q2-300</i>	2	300	129.4	1.991	2.167	53.50	21.29	1.074	0.085
<i>Case Q2-450</i>	2	450	103.7	1.816	2.323	60.89	38.05	0.969	0.121
<i>Case Q2-600</i>	2	600	69.2	1.563	2.566	78.45	77.87	0.750	0.203
<i>Case Q3-150</i>	3	150	161.6	2.243	1.966	48.28	9.45	1.152	0.059
<i>Case Q3-300</i>	3	300	143.5	2.189	1.998	53.06	20.30	1.102	0.077
<i>Case Q3-450</i>	3	450	125.8	2.125	2.050	58.74	33.18	1.039	0.100
<i>Case Q3-600</i>	3	600	107.8	2.047	2.124	66.03	49.71	0.954	0.131
<i>Case Q4-150</i>	4	150	169.5	2.360	1.885	48.41	9.76	1.119	0.056
<i>Case Q4-300</i>	4	300	158.9	2.421	1.830	52.96	20.06	1.071	0.068
<i>Case Q4-450</i>	4	450	148.7	2.472	1.789	57.80	31.05	1.030	0.082
<i>Case Q4-600</i>	4	600	138.5	2.512	1.756	63.04	42.93	0.991	0.098

<sup>a</sup> The values shown were obtained using adiabatic conditions, not taking into account the heat loss through the walls due to conduction and radiation.

<sup>b</sup> STP means standard temperature (273.15 K) and pressure (100000 Pa).

Adding thermal energy to the gas increases the  $I_{sp}$  for all cases. A decrease in the mass flow rate requirement occurs for all cases as  $\dot{Q}$  is increased. In the cases where the thermal heating source is applied away from the exit plane, with regions of applied  $\dot{Q}$  labeled 1, 2, or 3, the thrust also decreases due to an increase in the overall shear stress at the wall. Only in the cases where the heat source is placed near the exit

plane, at region 4, there is a gradual increase in thrust with increasing  $\dot{Q}$ . These set of behaviors for each region where  $\dot{Q}$  was applied can be observed in the following figure.

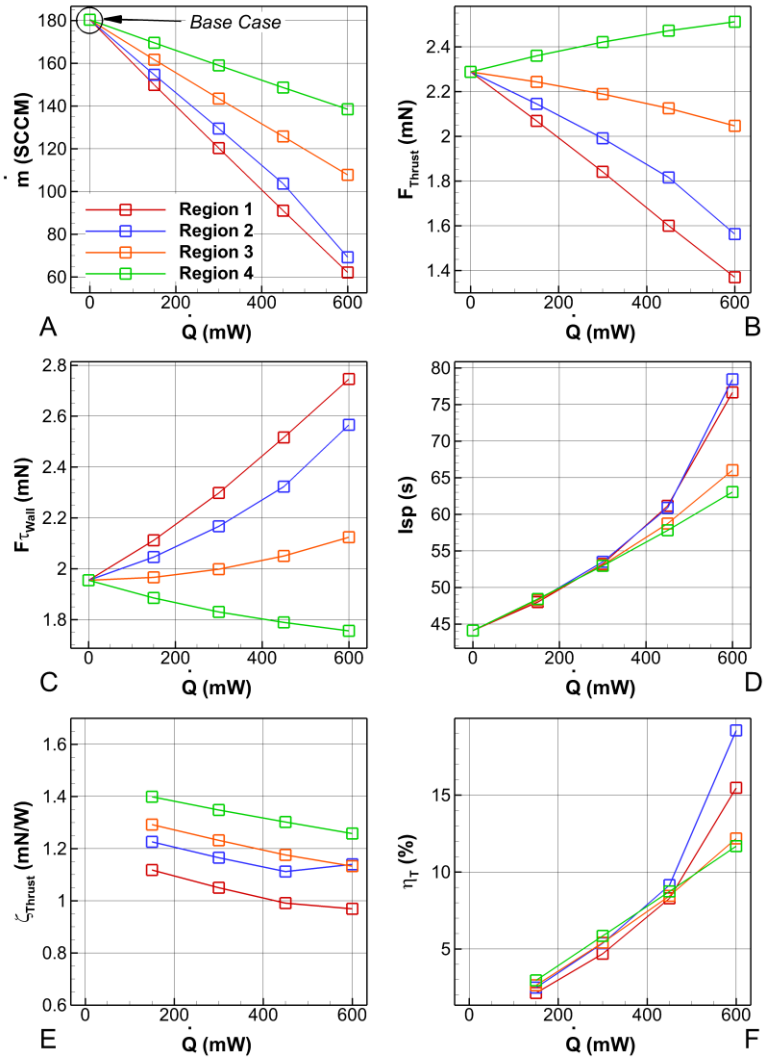


Figure 7-4. Graphical representation of different parameters. A) Mass flow rate, B) thrust, C) shear stress at the wall, D) specific impulse, E) thrust effectiveness and F) thruster total efficiency vs. total thermal heating source for each different region in Figure 7-3 using values from Table 7-1.

In Figure 7-4 (A-D), when the heat source is located near the exit plane, in region 4, we observe a linear decrease of mass flow rate requirement with a negative slope of 69.5 (SCCM/W), and a near linear increase in thrust with positive slope of 0.37 (mN/W).

This behavior in the thrust is due to an inversely proportional decrease in the shear force at the wall. When the heat source is located closer to the inlet, in region 2, we observe a decrease in the mass flow rate requirement with a slope of 182.0 (SCCM/W), and a decrease in thrust with a slope of 1.19 (mN/W). The  $I_{sp}$  for all cases increases linearly while  $\dot{Q}$  is less than or equal to 300 (mW), independently of the location where  $\dot{Q}$  is applied. For greater values of  $\dot{Q}$ , with  $\dot{Q}$  applied in regions 1 and 2, the  $I_{sp}$  increases with a quadratic trend and the thruster is no longer choked ( $M < 1$ ), for cases with  $\dot{Q}$  applied in regions 3 and 4 the linear positive trend is maintained. For the cases with  $\dot{Q}$  equal to 600 (mW), the  $I_{sp}$  increases the closer  $\dot{Q}$  is applied to the inlet, with the exception of case Q1-600, with  $\dot{Q}$  applied in region 1, due to the interaction between the applied  $\dot{Q}$  and the inlet boundary condition. Case Q1-600 characteristics are most likely due to numerical effects.

In Figure 7-4 (E, F), the thrust effectiveness and total efficiency were calculated using the following equations

$$R_W = \left( \frac{W_{new}}{W} \right) = \left( \frac{\dot{m}_{Base\ Case}}{\dot{m}_{Case}} \right), \text{ where } W=1 \text{ cm}, \quad (7-4)$$

$$\zeta_{Thrust} = \frac{R_W (F_{Thrust})_{Case} - (F_{Thrust})_{Base\ Case}}{R_W (P_W)_{Case}},$$

$$\eta_T = \frac{\left( R_W (F_{Thrust})_{Case} - (F_{Thrust})_{Base\ Case} \right)^2}{2(\dot{m}_{Base\ Case})(R_W)(P_W)_{Case}}, \quad (7-5)$$

since the mass flow rate and thrust decrease for some cases with added  $\dot{Q}$ , a longer width ( $W_{new}$ ) is assumed for the given case to match the mass flow rate of the base

case. The *base case* thrust is subtracted from the thrust of the given case to take into account only the additional thrust at a given mass flow rate produced by adding thermal energy. For the cases shown in [Table 7-1](#),  $P_w$  is assumed to be equal to  $\dot{Q}$ .

In [Figure 7-4 \(E\)](#), the thrust effectiveness decreases linearly for the cases with  $\dot{Q}$  applied in either region 3 or 4. For the cases with  $\dot{Q}$  applied in region 1 or 2, the slope of the thrust effectiveness is negative and linear while the exit Mach number is ( $> 0.9$ ), but for the cases with the highest  $\dot{Q}$ , with ( $M < 0.9$ ), the slope of the thrust effectiveness does not follow the same negative, linear trend. For the cases with the highest  $\dot{Q}$  for all four regions, the value of the thrust effectiveness seems to correlate with the values of the exit temperature, which is the highest ( $\sim 632$  K) for *Case Q2-600*. The shift in the slope trend of the thrust effectiveness for cases with the highest  $\dot{Q}$  applied in regions 1 or 2, indicates that for a thruster operating with low Mach numbers ( $M < 0.75$ ) throughout the domain, the thrust effectiveness increases primarily with increasing exit temperature. In [Figure 7-4 \(F\)](#), the total efficiency of the thruster increases with increasing  $\dot{Q}$ , and similarly to the thrust effectiveness, for the cases with the highest  $\dot{Q}$  and low exit Mach numbers ( $M < 0.75$ ), it depends strongly on the exit temperature. The relatively low values of total efficiency are due to the under-expansion of the flow since the exit pressure ( $\sim 30$  Pa) is higher than the external ambient pressure ( $\sim 0.05$  Pa) and only a fraction of the thermal energy is converted to kinetic energy. This is typical of non-optimized micro electro-thermal thrusters.

The following figure shows two comparisons: between the *base case and case Q2-600*, and between the *base case and case Q4-600*.

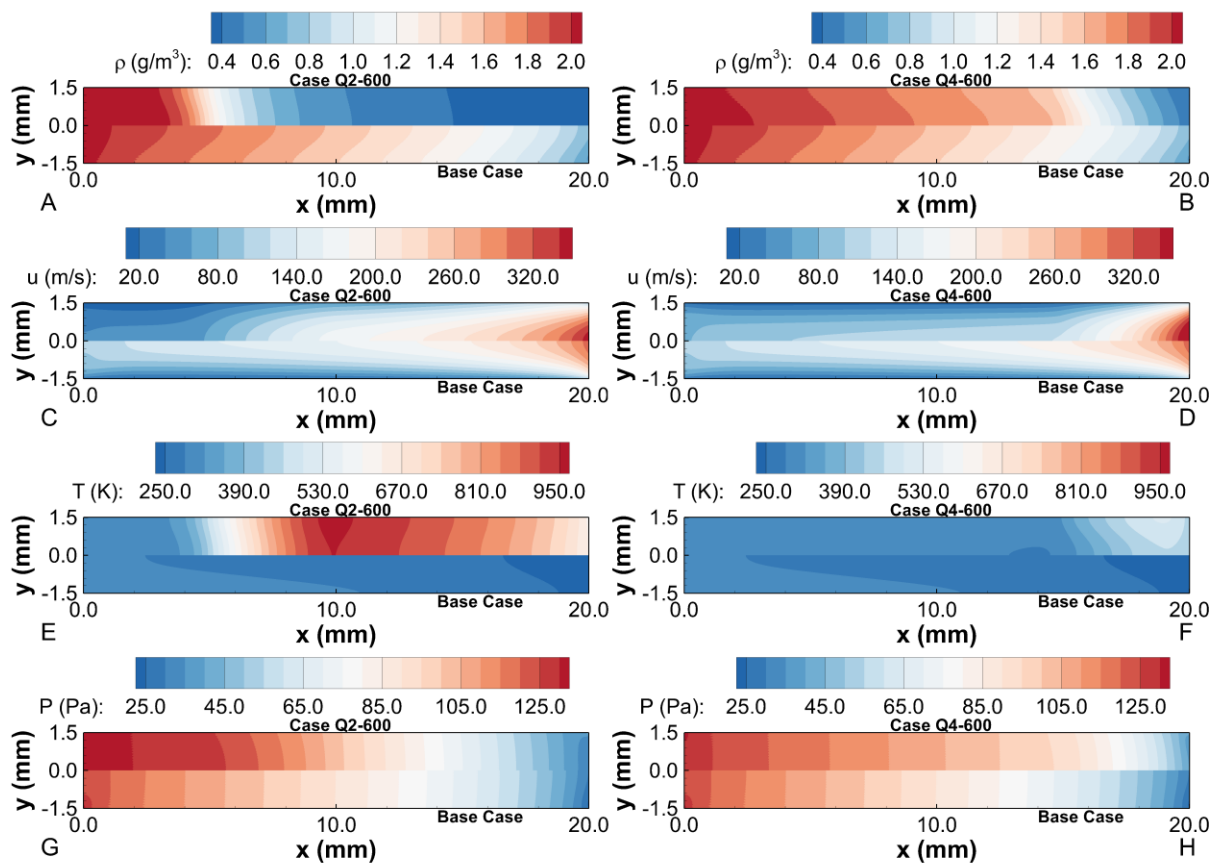


Figure 7-5. Comparisons between “*base case and case Q2-600*”, and “*base case and case Q4-600*.” A, B) Density, C, D) x - component of velocity, E, F) temperature, and G, H) pressure.

The two comparisons between the *base case and case Q2-600*, and between the *base case and case Q4-600*, shown in [Figure 7-5](#) (A-H), revealed that adding thermal energy to the flow increases the temperature of the gas around the region where  $\dot{Q}$  is added, and downstream of this region. An inversely proportional decrease in density happens where the temperature is increased in the domain and a distortion in the profile of pressure occurs in comparison to the *base case* in both cases, *case Q2-600* and *case Q4-600*. The x-component of velocity (or tangential velocity) displays a zone of

lower values than the *base case* before the thermal energy is added for both cases; followed by an acceleration zone after the thermal energy is added.

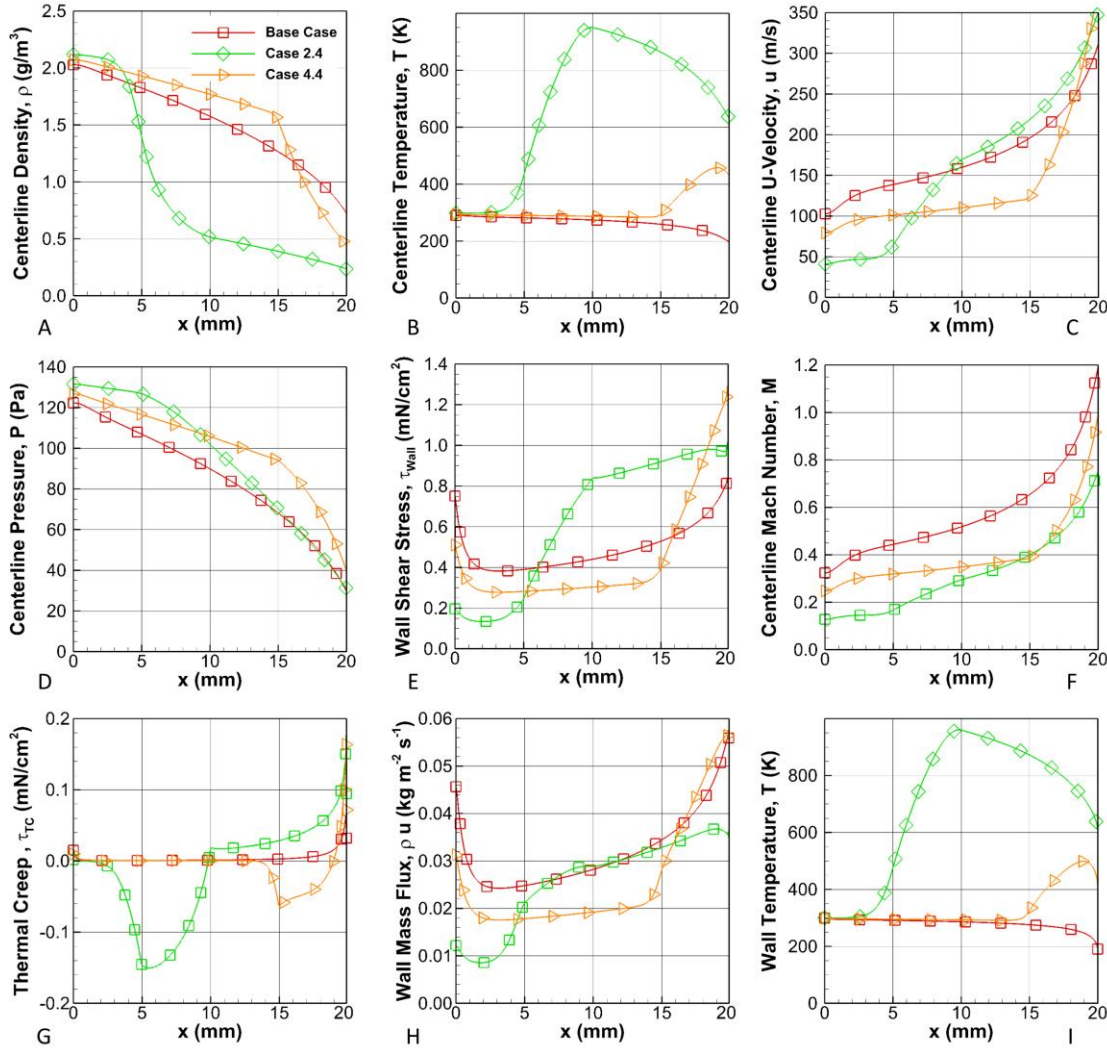


Figure 7-6. Comparison of *base case*, *case Q2-600*, and *case Q4-600*. A) Density, B) temperature, C) x - component of velocity, and D) pressure at the centerline. E) shear stress at the wall, F) Mach number at the centerline, G) thermal creep component of the shear stress at the wall, H) mass flux at the wall, and I) temperature at the wall.

Figure 7-6 shows a comparison of the *base case*, *case Q2-600*, and *case Q4-600* at two different cross-sections: the wall and the centerline. If the *thermal creep* term is neglected in the slip flow boundary condition (for simplicity of the analysis), the shear

stress is proportional to  $\rho$ ,  $u$ , and  $T^{0.5}$  at the wall. Since the mass flow rate requirement is smaller for cases with added thermal energy than for the *base case*, the mass flux ( $\rho u$ ) is smaller in most of the domain along the wall for cases with added  $\dot{Q}$  as shown in [Figure 7-6\(H\)](#). Alternatively, the shear stress, shown in [Figure 7-6\(E\)](#), increases with wall temperature, shown in [Figure 7-6\(I\)](#). These two competing contributions, ( $\rho u$ ) and  $T$ , cause the shear stress to decrease before the region where  $\dot{Q}$  is added and increase right after. The *thermal creep*, see [Figure 7-6\(G\)](#), plays a minor role that increases this effect since molecules creep from cold towards hot regions [97]. The thermal creep contribution to the shear stress is negative while  $T$  is increasing and positive while  $T$  is decreasing along the tangential direction at the wall. The shear force in case Q2-600 at the wall increased by about ~30% when compared to the *base case*. For case Q4-600, the shear force is ~10% lower than the *base case*. For both cases, the shear force causes an inversely proportional change in the thrust of similar percentage. The total shear force experienced by the fluid and the thrust produced by the device depends on the fraction of the wall area that is exposed to the higher temperatures. This observation shows that if maximizing the thrust in the device was the most desirable objective, the  $\dot{Q}$  should be applied closer to the exit plane to minimize viscous losses.

For case Q2-600, the most drastic change in comparison to the *base case* due to the addition of thermal energy occurs in its density and temperature, shown in [Figure 7-6 \(A,B\)](#). At the exit plane,  $T$  increases by a factor of (~3) and  $\rho$  decreases inversely proportional. The increase in  $T$  at the exit plane, as observed in [Figure 7-6\(B\)](#), increases the speed of sound. The Mach number at the exit plane, [Figure 7-6 \(F\)](#), decreases from 1.0 for the *base case* to 0.75 for case Q2-600, despite  $u$  increasing by 13%, as shown

in Figure 7-6(C). The addition of thermal energy has caused the flow to change from choked flow ( $M_{Throat} \sim 1$ ) to subsonic ( $M_{Throat} < 1$ ), meaning that viscous losses play an important role in this particular pressure regime for this channel design and prevent the exit tangential velocity from increasing with ( $T^{0.5}$ ) in a directly proportional manner. The pressure profile, Figure 7-6 (D), has a gradual slope until heat is added at ( $x = 6$  mm) and decreases with a steeper slope from this point on. Exit plane  $P$  is virtually unaffected, only 4% higher. At the exit plane,  $P$  and  $u$  change only a small amount in comparison to ( $\rho$ ) for case Q2-600. Given that  $\dot{m} \sim (\rho u)_{exit}$ ,  $F_{Thrust} \sim (\rho u^2 + P)_{exit}$  and  $I_{sp} \sim (u + P/(\rho u))_{exit}$ , the mass flow rate and thrust decrease as  $\rho$  decreases. The  $I_{sp}$  increases due to the  $(P/(\rho u))_{exit}$  term increase, since  $(P/(\rho u))_{exit} \propto (1/\rho)_{exit}$  if  $P_{exit}$  remains unchanged when compared to the *base case*, which in these cases it does, and the change in and  $u_{exit}$  is small when compared with  $\rho_{exit}$ .

For case Q4-600, at the exit plane  $T$  increases by a factor of ( $\sim 2$ ),  $\rho$  decreases by 40%,  $P$  and  $u$  increase by 33% and 23%, respectively, in comparison to the *base case*. Although the increase in  $P$  and  $u$  are beneficial to increase the  $I_{sp}$ , the  $I_{sp}$  percent increase for this case is not as significant as for case Q2-600. The decrease in  $\rho$  at the exit plane plays the most important role in increasing the  $I_{sp}$  and it is inversely proportional to the increase in  $T$ .

The *base case* has an exit Reynolds number of  $\sim 33$ , proving our initial assumption that an expansion nozzle would be counterproductive to increase the specific impulse since ( $Re < 100$ ). All other cases have smaller exit Reynolds number due to heat addition. Increasing the tangential momentum accommodation coefficient in the slip flow boundary conditions from 0.89 to 1.0 increased the  $I_{sp}$  for case Q2-450 by

4%. The *thermal creep* (transpiration) effects can affect the variation of pressure caused by tangential temperature gradients [97]. The *thermal creep* was only significant for cases with very high temperatures ( $\sim 900$  K), such as case Q2-600, where the shear stress is affected the most in the region between ( $5 \text{ mm} < x < 10 \text{ mm}$ ) by to the *thermal creep*, as shown in Figure 7-6(G). The higher-order slip flow boundary condition presented by Xue and Fan [98] as described in Zhang et al. [99] were tested for cases with low temperature, e.g. case Q2-450, and compared with cases using equation (4-82) and no effect in the  $I_{sp}$  was detected, indicating that the first-order approximation equation used in this study, equation (4-82), is sufficient to model the flow.

The  $Kn$  at the centerline for the *base case* is  $1.9 \times 10^{-2}$  at the inlet and  $4.5 \times 10^{-2}$  at the exit plane, while for case Q2-600 the  $Kn$  is  $1.8 \times 10^{-2}$  at the inlet, and as high as  $2.0 \times 10^{-1}$  at the exit plane. The  $Kn_{exit}$  for case Q2-600 is the highest of all cases and higher than the typical recommended range of values for slip flow regime ( $0.001 < Kn < 0.1$ ). Maurer et al. [100] estimated the upper limit of the slip flow regime as  $Kn = 0.3 \pm 0.1$  [45], where  $Kn$  is based on the channel height as in this dissertation. For RGEJ, only the cases with ( $Kn < 0.1$  or  $Kn \sim 0.1$ ) will be presented and studied.

Based on these results, region 2 was picked as the best location to apply the thermal heating source in order to increase the  $I_{sp}$ . The closer  $\dot{Q}$  is applied to the inlet, the higher the  $T_{exit}$ , see case Q2-600 vs. case Q4-600 in Figure 7-6(B, I), which proportionally relates to the  $I_{sp}$ . Region 1 was not picked due to its interaction with the inlet boundary condition. The decrease in thrust experience by the cases with  $\dot{Q}$  applied in region 2 could be counteracted by using a greater number of slots or a wider slot in the device if a given thrust is necessary.

## RGEJ thruster performance

The following table shows the performance parameters of several cases with plasma-aided technology at different voltages with geometry, mesh, and boundary conditions as defined in [Figure 7-2](#).

Table 7-2. Values of: voltage (V), mass flow rate ( $\dot{m}$ ), thrust ( $F_{Thrust}$ ), shear force ( $F_{\tau_{Wall}}$ ), specific impulse ( $I_{sp}$ ), specific impulse percent increase ( $I_{sp}$  Inc.), current ( $I$ ), total thermal heating source ( $\dot{Q}$ ), total electrical power ( $P_W$ ), and fraction of the total electrical power converted into thermal heating source ( $\dot{Q}/P_W$ ).

Case	V	$\dot{m}$	$F_{Thrust}$	$F_{\tau_{Wall}}$	$I_{sp}$ <sup>a</sup>	$I_{sp}$ Inc.	$I$	$\dot{Q}$	$P_W$	$\dot{Q}/P_W$
	V	SCCM	mN	mN	s	%	mA	mW	mW	%
Base case	0	180.3	2.288	1.955	44.1	-	0.000	0	0	-
Case 450V	450	136.5	2.039	2.113	51.9	17.7	0.538	240	242	99.4
Case 550V	550	123.7	1.964	2.187	55.2	25.1	0.570	308	313	98.3
Case 650V	650	113.6	1.898	2.253	58.1	31.7	0.565	360	367	98.0
Case 750V	750	105.6	1.843	2.308	60.7	37.6	0.541	400	406	98.5

<sup>a</sup> The values shown were obtained using adiabatic conditions, not taking into account the heat loss through the walls due to conduction and radiation.

In general, the plots of  $\dot{m}$ ,  $F_{Thrust}$ ,  $F_{\tau_{Wall}}$ , and  $I_{sp}$  as functions of  $\dot{Q}$  follow similar trends as the previous cases in [Table 7-1](#) with constant thermal heating source applied in region 2. The current, thermal heating source and power vs. voltage are discussed in the section labeled as *RGEJ thruster discharge characteristics*.

In [Table 7-1](#), the  $\dot{Q}$  vs.  $I_{sp}$  have positive slopes, 31.5 (s/W), approximately linear for the range of  $\dot{Q}$  between 0-300 (mW) and independent of the location where  $\dot{Q}$  is applied. The plasma-aided cases of RGEJ, shown in [Table 7-2](#), have a significantly higher  $\dot{Q}$  vs.  $I_{sp}$  positive slope, 54.8 (s/W), which indicates that concentrating the total

value of  $\dot{Q}$  in a smaller region of the domain is beneficial to increase the  $I_{sp}$  for adiabatic cases. Case 750V has an  $I_{sp}$  of 60.7 (s), a 37.6% improvement over the *base case*. The  $I_{sp}$  of RGEJ, (60.7 s), operating at 750 (V) is 16% higher than the  $I_{sp}$  of a highly optimized argon propellant cold gas thruster, (52 s), and 35% higher than the  $I_{sp}$  of the argon propellant FMMR, (45 s) [4]. The increase in  $I_{sp}$  for case 750V over cold gas thrusters is achieved with only 406 (mW) per centimeter of width of the device and 98.5% of the total electrical power is converted to heating of the neutral gas. This percentage is higher than the range (81-95%) predicted by Houba and Roy [101] for a device operating at an assumed constant temperature (300 K) and pressure (0.6 Torr) using air as the working fluid. The remainder of the discharge power goes into the electrons, which lose energy in inelastic collisions due to the various ionization, attachment, and excitation reactions [101].

The thrust effectiveness of the device and total efficiency are shown in the following figure.

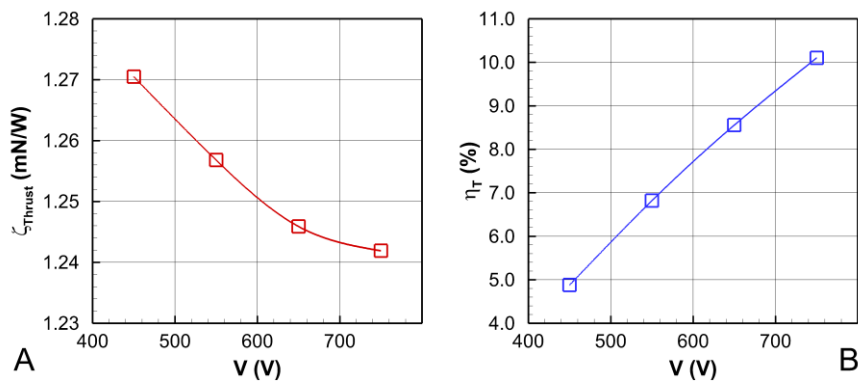


Figure 7-7. Parameters of the RGEJ thruster for the given voltage regime. A) Thrust effectiveness and B) total efficiency.

In [Figure 7-7\(A\)](#), the thrust effectiveness decreases by 2.25% with a parabolic trend over the range of voltages tested (450 - 750 V). For higher voltages, the thrust

effectiveness is expected to increase based on the trend observed in Figure 7-4(E) for  $q'''$  applied in region 2. In Figure 7-7(B), the efficiency of the RGEJ thruster increases linearly with increasing voltage at a rate of 17.4 (%/kV) and it doubles over the range of voltages tested. The thrust effectiveness and total efficiency obtained for case 750V are 1240 ( $\mu\text{N}/\text{W}$ ) and 10%, respectively. For comparison, the MPT operating at 100 Torr plenum pressure and wall temperatures of 300 K has a mass flow rate of 0.14 mg/s, a thrust of 67.4  $\mu\text{N}$  for the cold gas thruster case, and a thrust of 100  $\mu\text{N}$  for the 750 (V) and 650 (mW) plasma-aided case which produces an  $I_{sp}$  of  $\sim 74$  (s) [10], [11]. These values make the MPT's thrust effectiveness and total efficiency equal to 50 ( $\mu\text{N}/\text{W}$ ) and 0.6%, respectively. The thrust effectiveness of the MPT is comparable to other electro-thermal thrusters such as the VAT with a thrust effectiveness of 10  $\mu\text{N}/\text{W}$  [15]. The thrust effectiveness of the RGEJ is two orders of magnitude higher than other competing technologies.

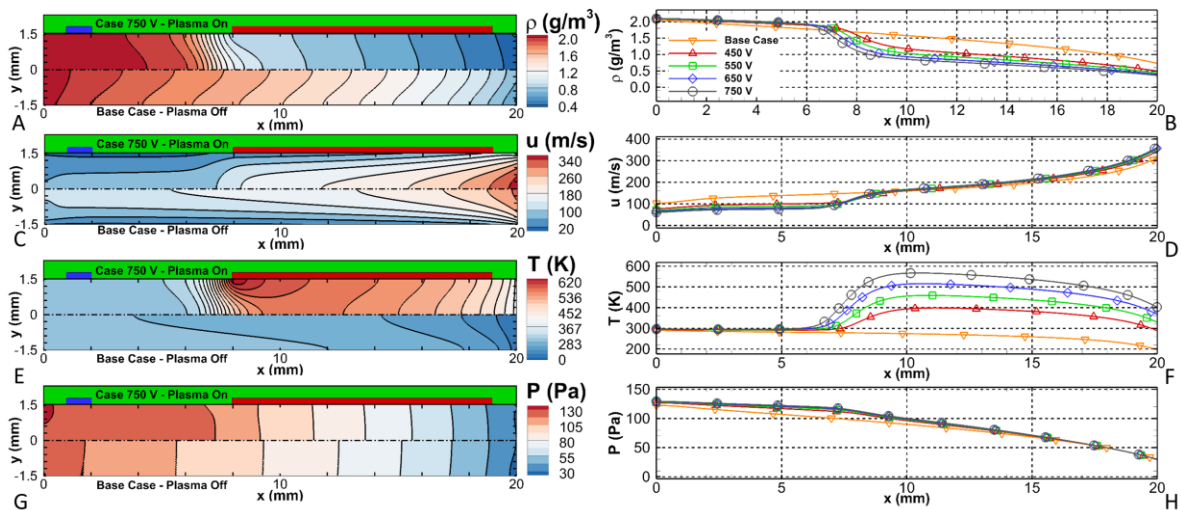


Figure 7-8. Left plots show a comparison of the rarefied gas results between the *base case* (on the bottom half) and *case 750V* (on the top half). Right plots show a comparison of the rarefied gas centerline results for the *base case* and all the plasma cases. A,B) Density, C,D) tangential velocity, E,F) temperature, and G,H) pressure. Top wall anode (blue) and the cathode (red).

Figure 7-8 shows a comparison of the results of the rarefied gas simulations. Figure 7-8(E) shows how the plasma locally heats the gas in case 750V to temperatures as high as (~640 K) near the corner of the cathode electrode where high electric field causes the volumetric electro-thermal heating source to increase sharply. The localized heating causes the gas density to decrease in the areas of high temperature, see Figure 7-8(A). By comparison, the *base case* has a temperature profile that decreases along the x-axis direction as we approach the exit plane due to the flow expansion and a similar density profile. In Figure 7-8(F), the exit temperature at the centerline is higher for the higher voltage cases with case 750V having a temperature of (~400 K), twice the value of the *base case* (~200 K). The speed of sound doubles for case 750V.

The pressure profile, see Figure 7-8(G, H), is affected by the addition of thermal energy to the flow. The *base case* shows a near linear decrease in pressure for ( $x < 11$  mm) with  $(-\partial P/\partial x) \sim 3.5$  (Pa/mm), followed by a parabolic decrease. Four important effects are encountered in micro-flows: *rarefaction*, *compressibility*, *viscous heating*, and *thermal creep* [97]. Out of those, *compressibility* and *rarefaction* are competing effects. The curvature in the pressure distribution found in channels with compressible flows is due to *compressibility* effects, the higher the Mach number the greater this effect becomes, the curvature increases as the inlet to outlet pressure ratio is increased [45]. *Rarefaction* decreases the curvature in the pressure distribution, which becomes increasingly linear as the free-molecular flow regime is approached with increasing *Kn* numbers [97]. In the pressure profile in Figure 7-8(H), *rarefaction* is dominant in the *base case* for ( $x < 11$  mm,  $Kn = 0.03$ ) and the *compressibility* effects become increasingly important in the rest of the domain due to increasing Mach number. For all

the plasma-aided cases, case 450V-750V, the pressure profile is very similar independent of voltage (thermal energy input), but the pressure profile has two distinct linear regions, one before and one after the area where thermal energy is deposited. The effect of *rarefaction* dominates for ( $x < 16$  mm,  $Kn = 0.077$ ) due to the higher  $Kn$  numbers found in the plasma-aided cases in comparison to the *base case*. For case 750V, the two distinct linear regions have  $(-\partial P/\partial x) \sim 1.5$  (Pa/mm) for ( $x < 7$  mm) and 5.5 (Pa/mm) for ( $7 \text{ mm} < x < 16 \text{ mm}$ ), respectively. These two different regions are caused by the difference in temperature, which affects the shear stress at the wall in the same manner as the cases in [Table 7-1](#).

The tangential velocity plots, in [Figure 7-8\(C, D\)](#), show the effect of having two distinct  $(-\partial P/\partial x)$  regions in case 750V. The *base case* has a constant acceleration of the flow along the channel, but case 750V has approximately constant velocity before thermal energy is added due to the low  $(-\partial P/\partial x)$  for ( $x < 7$  mm) follow by an acceleration region where  $(-\partial P/\partial x)$  is higher. The acceleration region is similar to a shorter channel operating with the same inlet to outlet pressure ratio at a higher inlet temperature. This observation may be useful to modify the geometry of the thruster's design in the future for optimization purposes.

The addition of thermal energy increases the tangential velocity at the exit plane centerline from 311 (m/s) in the *base case* to 362 (m/s) in case 750V and decreases the density from 0.73 (g/m<sup>3</sup>) to 0.36 (g/m<sup>3</sup>), increasing the  $I_{sp}$  of the thruster. Due to low Reynolds numbers ( $< 30$ ) in all cases and dominant viscous terms, no shock discontinuities are found. As the Reynolds number decreases with increasing

temperature (thermal energy input), the viscous losses increase causing a degradation of the thrust, which could be counteracted by extending the width of the device.

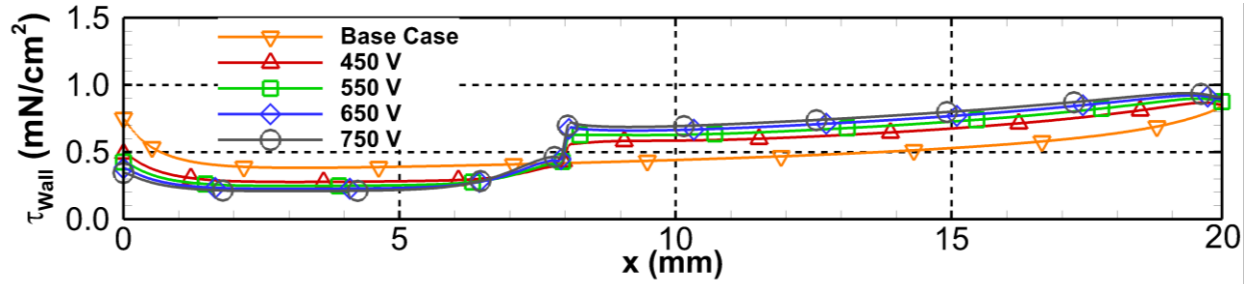


Figure 7-9. Shear stress at the wall for all cases in Table 7-2.

The *thermal creep*, a *rarefaction* effect, plays a significant role close to the cathode electrode corner at (~8 mm) where the magnitude of  $(\partial T/\partial x)$  is the highest, causing a sharp discontinuity in the profile of shear stress at the wall. In this location, the shear stress abruptly increases due to the *thermal creep*, but the *thermal creep* effect is negligible in the rest of the domain due to low  $(\partial T/\partial x)$  values.

In the cases presented, the *viscous heating* effect is not apparent since for pressure-driven compressible flows the expansion cooling negates it [97].

Figure 7-10 show a comparison of the results of the ionized gas simulations for the given DC voltages. The applied voltage was varied from 450 to 750 V, this range is within the operating conditions of the validation cases.

In Figure 7-10, (A, C, E,G, I, K) display a comparison of the contours and (B, D, F, H, J, L) display a comparison of the centerline cross-section, respectively, for the electrons number density, positive ions number density, the three types of metastable atoms number densities and electron energy density.

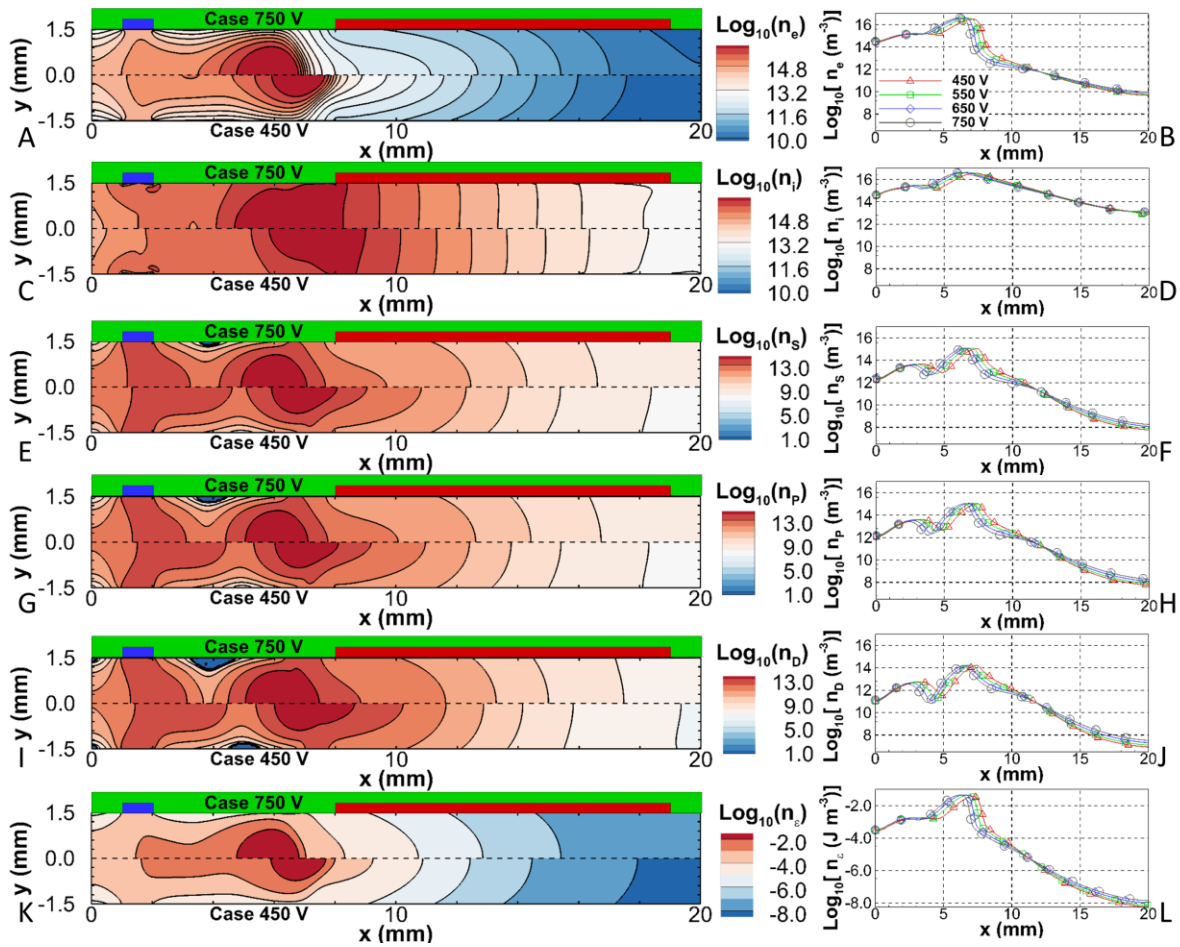


Figure 7-10. Comparison of plasma discharge results for case 450V and case 750V (on the left), and comparison of plasma-discharge centerline results for all cases (on the right). A, B) Electron number density in  $\text{m}^{-3}$ , C, D) ion number density in  $\text{m}^{-3}$ , E, F, G, H, I, J) three types of metastable atom number densities in  $\text{m}^{-3}$ , and K, L) electron energy density in  $\text{J m}^{-3}$ . The top wall is shown to illustrate the position of the anode electrode (blue) and the cathode electrode (red).

For case 750V the maximum values reach  $4.03 \times 10^{16} \text{ (m}^{-3}\text{)}$ ,  $4.23 \times 10^{16} \text{ (m}^{-3}\text{)}$ ,  $1.18 \times 10^{15} \text{ (m}^{-3}\text{)}$ ,  $1.09 \times 10^{15} \text{ (m}^{-3}\text{)}$ ,  $1.55 \times 10^{14} \text{ (m}^{-3}\text{)}$ , and  $0.045 \text{ (J/m}^3\text{)}$ , respectively. The metastable atoms number densities are approximately one to two orders of magnitude lower than the charged particles and their contribution to ionization is very small for the given pressure operation regime. For case 450V, the maximum number density values are very similar as in case 750V, but the peak values shift towards the inlet.

The electron temperature ( $T_e$ ), calculated using the electron energy and number densities, is ( $\sim 4$  eV) in the plasma column for all cases. In the cathode fall, where electron number density decreases to very small values ( $< 10^{13} \text{ m}^{-3}$ ) by comparison to the peak value ( $\sim 10^{16} \text{ m}^{-3}$ ), the ( $T_e$ ) is over-predicted and can increase exponentially in this region of vanishing electron densities due to a numerical artefact of the fluid model [10]. This behavior of ( $T_e$ ) does not affect the accuracy of the simulations for the other variables since the electron energy content is negligible in this part of the domain [10].

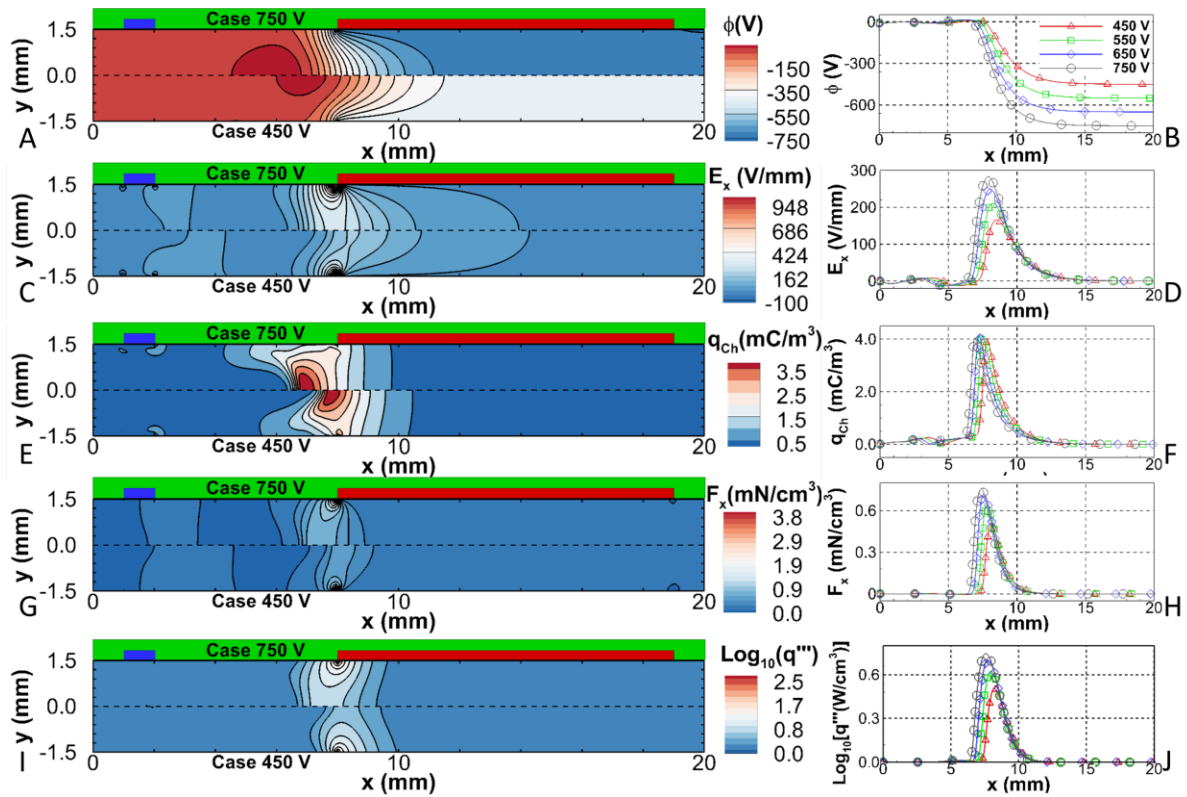


Figure 7-11. Comparison of plasma discharge results for case 450V and case 750V (on the left), and comparison of plasma-discharge centerline results for all cases (on the right). A, B) Electric potential in V, C, D) tangential component of the electric field in V/mm, E, F) charge separation in mC/m<sup>3</sup>, K, L) tangential component of the volumetric plasma-induced electrostatic force in mN/m<sup>3</sup>, and I, J) the electro-thermal volumetric heating source in W/m<sup>3</sup>. The top wall is shown to illustrate the position of the anode electrode (blue) and the cathode electrode (red).

In [Figure 7-11](#), (I, J) show the volumetric electro-thermal heating source ( $q'''$ ), concentrated in the cathode fall, reaching a maximum value of  $\sim 4 \times 10^2$  (W/cm<sup>3</sup>) near the corner of the cathode for case 750V. Although this value looks large, it is concentrated in a small region of the domain and the integrated value of the total electro-thermal heating source ( $\dot{Q}$ ) is  $\mathcal{O}(100)$  mW.

In [Figure 7-11](#) (G, H), the induced volumetric plasma-induced electrostatic force is shown, which proportionally increases with the applied voltage, but its magnitude in the tangential direction is too insignificant to contribute to the thrust of the device.

An interesting finding in this comparison of cases at different voltages is that the cathode fall region is increased with increasing voltage while compressing the region of the plasma column. When case 450V and case 750V are compared in [Figure 7-10](#) (A, C, E, G, I, K) and [Figure 7-11](#) (A, E), we can observe a shift towards the inlet of the charged particle number densities, electric potential peaks, and charge separation. This phenomenon is observed also in the corresponding centerline cross-section plots across the range of voltages tested.

In [Figure 7-10](#) (B, D), the peak values of the number densities of charged particles remain relatively constant,  $\sim 4 \times 10^{16}$  (m<sup>-3</sup>) for cases with voltages of 550 to 750 V. The peak value for case 450V is  $\sim 3 \times 10^{16}$  (m<sup>-3</sup>). For constant gas pressure and temperature cases, the number density of charged particles would drastically increase with increasing voltage, but for the plasma cases studied, the discharge seems to be self-limiting. For the cases shown in [Table 7-2](#), at a given applied voltage between 550 and 650 V, the current reaches a maximum and decreases with increasing voltage from this point on, instead of increasing along with the applied voltage. The behavior of the

current is examined in the next section. This phenomenon is caused by the decrease in the number density of neutrals as the gas temperature increases due to the localized heating. The normal ion flux ( $\Gamma_{i,y}$ ), the main contributor to the discharge current at the cathode, is higher for cases with higher voltages near the corner of the cathode electrode, with values ranging from  $2.9 \times 10^{20}$  to  $2.29 \times 10^{20}$  ( $\text{m}^{-2} \text{s}^{-1}$ ) for the given voltage range between 450 and 750 V. Conversely,  $\Gamma_{i,y}$  is lower for the cases with higher voltages over most of the remainder of the cathode ( $8.45 \text{ mm} < x < 13 \text{ mm}$ ) and negligible for ( $x > 13 \text{ mm}$ ). This means that cases with higher voltages have a higher current density near the corner of the cathode electrode, but operate at a lower discharge current since most of the area of the cathode electrode is exposed to lower values of  $\Gamma_{i,y}$ . The reduction of  $\Gamma_{i,y}$  over most of the cathode ( $8.45 \text{ mm} < x < 13 \text{ mm}$ ) is due to the effects of the ion mobility and diffusion.

The ion mobility ( $\mu_i$ ) increases with a decrease in neutral number density or with a decrease in electric field magnitude ( $|\mathbf{E}|$ ). For the range of voltages studied, the electric field magnitude remains surprisingly similar for ( $8.45 \text{ mm} < x < 13 \text{ mm}$ ), therefore, the ion mobility increases at the wall with increasing applied voltage due to the decrease in neutral number density, which is due to the increase in gas temperature. The ion diffusion ( $D_i = k_B T_i \mu_i / e$ ) is further increased by the increase in ion temperature, which is assumed to be the temperature of the gas due to rapid thermalization of the ions with other heavy particles. Since the ion diffusion is more sensitive to the effects of gas heating than the mobility, the diffusion term of the ion flux causes the normal ion flux ( $\Gamma_{i,y}$ ) and the ion number density ( $n_i$ ) to decrease over the given area of the

cathode ( $8.45 \text{ mm} < x < 13 \text{ mm}$ ) for cases with higher voltages. This behavior causes the discharge to be current self-limiting and prevents the plasma from covering a greater area of the cathode electrode as the discharge voltage increases.

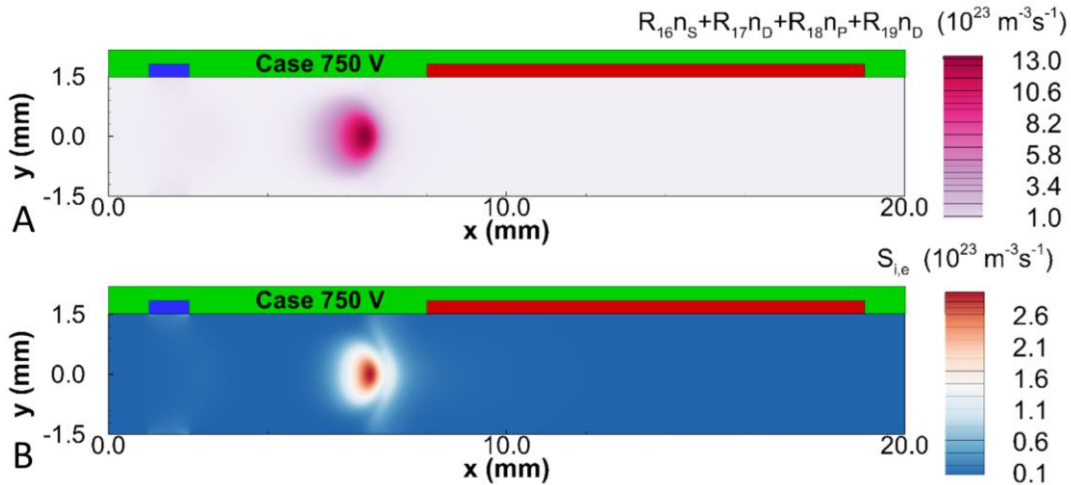


Figure 7-12. Case 750V. A) Sum of the photon-emitting reaction sources, and B) the ionization source for ions and electrons in their respective continuity equation, where ( $S_i = S_e$ ).

In [Figure 7-12 \(A\)](#), the sum of the photon-emitting reaction sources is shown for case 750V. This value gives the number density of all three types of metastable atoms per time destroyed in processes that generate photons. Therefore, it is the production source term for photons and it reveals that most photons are produced in the center of the domain before the cathode fall in the same region where the peak values for metastable atoms occur. [Figure 7-12 \(A\)](#) provides a qualitative comparison between the numerical code results in this dissertation and the experimental results obtained for the RFET [14] working at low pressures (1.5 Torr), where the discharge is brightest at the center of the domain.

In [Figure 7-12 \(B\)](#), most of the ionization happens close to edge of the plasma column before reaching the cathode fall and it is concentrated around the centerline,

similar to the RFET [14] when it is working at low pressures (1.5 Torr). The ions flow from this region of high electric potential, but a low electric field, to the walls where they recombined. In contrast, the electrons flow from the cathode to the rest of the walls, most of them flow into the anode and the rest into the dielectric sections of the walls to balance the ion current. The number of ions leaving the thruster through the exit plane is negligible; therefore their contribution to the thrust is neglected. Some power is always lost through inelastic collisions to solid walls and the outflow, but the heating of the walls due to neutralization is not taken into account since there will always be some amount of thermal heating loss through conduction and radiation. Our assumption of adiabatic walls is just an approximation to simplify the numerical simulation of a well-insulated thruster.

### **RGEJ thruster discharge characteristics**

The performance plasma-discharge characteristics of RGEJ are presented in this section. The discharge current ( $I$ ) is obtained by integrating the species current over the length of the electrode, and the plasma force effectiveness ( $\zeta_{\bar{F}_x}$ ) is obtained using the tangential component of the plasma induced electrostatic force ( $\bar{F}_x$ ) and the total electrical power ( $P_w$ ) [101]

$$I = 2e \int_{L_{\text{Electrode}}} \left( \sum_k \Gamma_k \cdot \hat{n} \right) W dx, \quad (7-6)$$

$$P_w = VI, \quad (7-7)$$

$$\bar{F}_x = 2 \int_0^{H/2} \int_0^L (F_x) W dx dy, \quad (7-8)$$

$$\zeta_{F_x} = \bar{F}_x / P_w \quad (7-9)$$

where the tangential volumetric plasma-induced electrostatic force ( $F_x$ ) is obtained from equation (4-69) and  $W = 1$  cm.

The following figure shows the performance plasma-discharge characteristics of the RGEJ as functions of voltage.

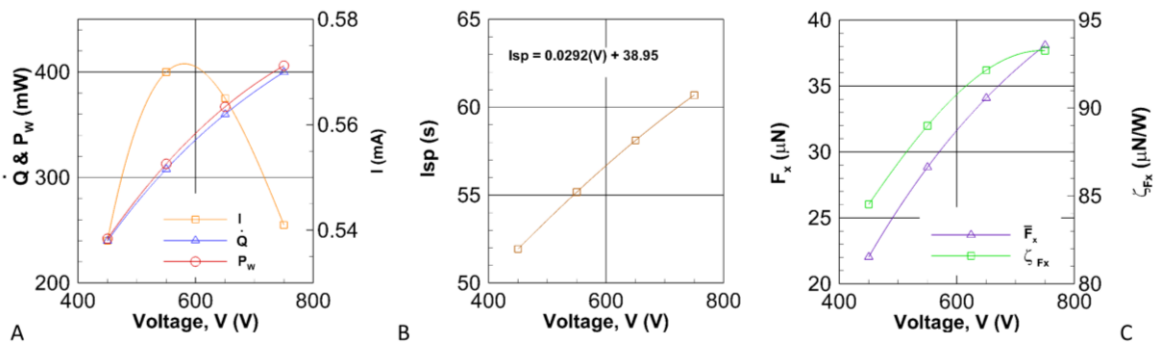


Figure 7-13. Parameters of the RGEJ thruster for the given voltage regime. A) Total thermal heating source, total electrical power and discharge current as functions of the applied voltage, B) specific impulse vs. voltage, and C) tangential component of the plasma induced electrostatic force and its effectiveness as functions of the applied voltage.

In [Figure 7-13\(A\)](#), the power consumed by the thruster varies from 242 to 406 (mW) over the range of voltages studied following a near linear trend, increasing with voltage. The current-voltage distribution shows a peak at ~ 550 (V), the current decreases for higher voltages. Deconinck et al. [10] showed that current decreases in a thruster with constant gas wall temperatures when the wall temperature is increased at the cathode. This phenomenon is due to the decrease in ion flux at the cathode caused

by the increase in gas temperature with increasing voltage as explained previously in the section labeled as *RGEJ thruster performance*. This decrease in current may be beneficial to decrease erosion of the cathode electrode permitting the thruster to operate at higher voltage and power. From 450 to 550 (V), the positive differential resistivity in the I-V characteristics indicates that the thruster operates in the abnormal glow regime, for higher voltages the thruster is transitioning to the normal glow regime, where only a portion of the cathode is covered by the plasma.

The  $I_{sp}$  increases linearly with increasing voltage with a slope of 0.0292 (s/V). For the voltage regime tested, the  $I_{sp}$  has not saturated, meaning that it could be further improved by increasing the voltage. The tangential component of the plasma induced electrostatic force ( $\bar{F}_x$ ) and the total thermal heating source ( $\dot{Q}$ ) increase almost linearly with increasing voltage. Although the direct contribution of the force to the total thrust is negligible, the plasma force term ( $F_x/\rho$ ) near the cathode corner is about a tenth of the pressure gradient term  $\left(-\frac{1}{\rho} \frac{\partial P}{\partial x}\right)$  in the Navier-Stokes equations.  $F_x$  and  $F_y$  locally affect the flow by creating a low-pressure region that pulls to flow towards the wall upstream of the corner of the cathode and accelerates the flow right after, in the tangential direction. The highest plasma force produced in the tangential direction ( $\bar{F}_x$ ) is 38 ( $\mu\text{N}/\text{cm}$ ), by comparison, the plasma force produced by Houba and Roy [101] is 5 ( $\mu\text{N}/\text{cm}$ ) at 600 (V) and 0.6 (Torr) using air as the working fluid. The effectiveness of the plasma force increases with increasing voltage approaching a saturation point.

## Thermal analysis

A simple thermal analysis of the thruster was performed by taking the temperature distribution at the channel walls and exit walls for *case 750V* to calculate the hypothetical heat loss through conduction and radiation. The analysis is performed with governing, boundary equations, and numerically modeled described in sections labeled *Heat Transfer Governing Equations* and *Decoupled Heat Transfer Codes*, respectively.

The heat loss via conduction is a minimum for thruster's slots that are stacked next to each other, similarly to FMRR. In the following conduction analysis, the heat loss via conduction is investigated for a single thruster's slot.

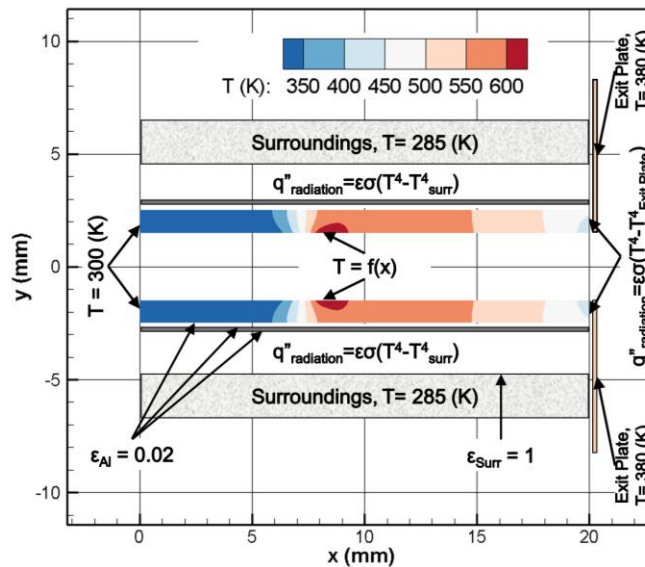


Figure 7-14. Conduction heat loss analysis for *Case 750V* assuming 1 cm of width, with the temperature distribution given along the wall as  $T=f(x)$ .

In [Figure 7-14](#), the conduction analysis of the thruster is performed using a (401×101) mesh, assuming 1.0 mm thick, insulating walls made of silica aerogel with a thermal conductivity of 4.2 (mW/m-K) for pressures (< 10 Torr). The thruster is covered

with an aluminum layer and an additional aluminum thin layer separates the thruster from the surroundings. For a well-insulated satellite, a MEMS thruster system external average temperature is 285 K [102]. The exit plate is the external wall of the small satellite. At steady state operation conditions, the rarefied gas module predicts an average temperature of 380 K for the exit plate surface close to the thruster's exit plane. A thin gap separates the thruster walls from the exit plate to prevent heat loss via conduction through that side of the channel walls. Neglecting the thermal resistivity of the electrode and dielectric materials due to their thinness, and neglecting any heat loss due to radiation through the exit plate, due to their assumed low emissivity, the heat loss through conduction of the internal walls at  $T=f(x)$  is 0.23 (mW) per centimeter of width of the thruster.

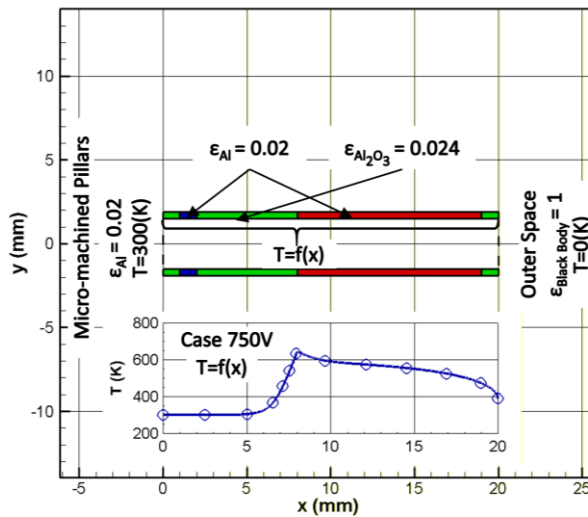


Figure 7-15. Radiation heat loss analysis for *Case 750V* assuming 1 cm of width, with the temperature distribution of given along the wall as  $T=f(x)$ .

In [Figure 7-15](#), the radiation analysis was performed using 400 plates in each internal wall, assuming each is a diffuse-grey surface. The inlet plane is considered a diffuse-grey surface with the emissivity of the electrodes since the plenum chamber will

contain micro-machined pillars or a porous metal material to heat the propellant. The radiation analysis has shown that if micro-machined pillars or a porous metal material is not used in the inlet, then a significant amount of thermal energy would scape the walls into the plenum, which would heat the gas in a non-localize manner. The background radiation temperature of outer space is assumed to be 0.0 K. The emissivities of the dielectric and electrodes were assumed to be  $\varepsilon_{Al_2O_3} = 0.24$  (aluminum oxide) and  $\varepsilon_{Al} = 0.02$  (aluminum), respectively [103]. The heat loss due to radiation is 30.1 (mW). The radiation heat loss depends strongly on the emissivity of the internal walls.

The adiabatic assumption in the cases presented is intended to provide an upper limit for the thruster's performance for the given operational parameters. The overall heat loss of a thruster working in outer space is 30.34 (mW), which is 7.5% of the input power in *Case 750V*, depending on the internal temperature of the small satellite, the insulation layer of the thruster, and the emissivity of the internal walls. In laboratory conditions, with an environment temperature of 300 K, the heat loss through conduction would be negligible in a well-insulated thruster and the heat loss through radiation would be 23.9 (mW), which is 5.9% of the input power, making the assumption of adiabatic walls a reasonable approximation for a comparisons with experiments. It is important to indicate that 1.5% of the total power in *Case 750V* is not transferred to the gas and it is mostly lost to the walls in the form of heat (98.5% of the total power is transferred to the gas). This loss is expected to decrease the discrepancy between the adiabatic assumption cases and future experiment results even further.

## CHAPTER 8 SUMMARY

### Summary of the Results

The RGEJ device shows encouraging results. For a single channel with a width of 1 cm operating at the highest voltage tested of 750 V, the RGEJ thruster requires a current of 0.541 mA and a total electrical power of 406 mW to heat the flow to temperatures as high as ~640 K. Under the given operation conditions, the RGEJ produces a thrust of 1.843 mN at a mass flow rate of 105.6 SCCM (3.095 mg/s), which produces a specific impulse ( $I_{sp}$ ) of 60.7 s. This  $I_{sp}$  is an improvement of 37.6% over a cold gas thrusters with the same geometry and working parameters, and it is an improvement of 16% and 35% over optimized argon propellant cold gas thrusters and argon propellant FMMR, respectively. Based on the  $I_{sp}$  vs. voltage characteristics, the thruster could operate at an even higher voltage to further increase the  $I_{sp}$ .

The thrust effectiveness and total efficiency obtained for the highest voltage tested are 1240 ( $\mu\text{N/W}$ ) and 10%, respectively. For comparison, the MPT operating at 100 Torr plenum pressure and wall temperatures of 300 K has a mass flow rate of 0.14 mg/s, a thrust of 67.4  $\mu\text{N}$  for the cold gas thruster case, and a thrust of 100  $\mu\text{N}$  for the 750 V and 650 mW plasma-aided case which produces an  $I_{sp}$  of ~74 s [10], [11]. These values make the MPT's thrust effectiveness and total efficiency equal to 50 ( $\mu\text{N/W}$ ) and 0.6%, respectively. The Vacuum Arc Thruster (VAT) has a thrust effectiveness of 10  $\mu\text{N/W}$  [15]. The thrust effectiveness of the RGEJ is two orders of magnitude higher than these similar plasma-aided technologies.

For the configuration of electrodes studied and range of voltages, the majority of the energy is converted into gas heating (~98%). This percentage is higher than the

range (81-95%) predicted by Houba and Roy [101] for a device operating at an assumed constant temperature (300 K) and pressure (0.6 Torr) using air as the working fluid. The plasma force plays a negligible role in the injection of momentum and the RGEJ operates as an electro-thermal thruster (heating the gas) instead of operating as an electrostatic thruster (accelerating the flow by ion collisions).

High heat loss is typical in MEMS-scale micro-thrusters [4]. For example, FMMR required twice (200% of) the power used to heat the gas to operate due to heat losses. In contrast, a simple thermal analysis estimated that the proposed RGEJ thruster would require 7.5% more input power to maintain the same performance due to heat loss in outer space, this number could be decreased by reducing heat loss through conduction and radiation by stacking many thruster's slots and using a dielectric material with lower emissivity.

The peak values of the number densities of charged particles remain relatively constant ( $\sim 4 \times 10^{16} \text{ m}^{-3}$ ) for cases with voltages of 550 to 750 V. For constant gas pressure and temperature cases, the number density of charged particles would drastically increase with increasing voltage, but for the plasma cases studied, the discharge is self-limiting due to the increase in gas temperature as the applied voltage is increased. The current-voltage distribution shows a peak at  $\sim 550 \text{ V}$  and the current decreases in cases with higher voltages. From 450 to 550 (V), the positive differential resistivity in the I-V characteristics indicates that the thruster operates in the abnormal glow regime, for higher voltages the thruster is transitioning to the normal glow regime, where only a portion of the cathode is covered by the plasma. This decrease in current may be beneficial to decrease erosion of the cathode electrode due to sputtering,

permitting the thruster to operate at higher voltage and power. The sputtering rate at the front corner of the cathode was calculated to be  $3.68 \times 10^{-8}$  cm/s for copper electrodes. The cathode corner region experiencing peak ion current density will be eroded 1 mm every 755 hours of continuous thruster operation. This sputtering rate can be decreased by using stronger materials in the corner of the cathode (e.g. tungsten).

The RGEJ material compatibility between the propellant and the surface when operating with argon is not optimum because argon causes high sputtering, but if RGEJ can operate with water propellant, the long aluminum cathode electrodes could be silver plated to help mitigate the formation of hydrogen peroxide, serving as a catalyst to decompose it. Due to the low plenum pressure and the long slot design, RGEJ is expected to have very low or negligible valve leakage problems and no passage clogging complications that could result in a single-point failure. The system reliability and durability has to be determined, but the only real concern would be the electrode erosion due to sputtering, which is the most damaging in the front corner of the cathode electrode. Due to the RGEJ design simplicity, with no moving parts, other reliability and durability problems are avoided. The RGEJ can even operate as a cold gas thruster. The RGEJ produces thrust in the  $\mathcal{O}$ (mN) necessary for slew maneuvers at very low power. The minimum impulse bit of the RGEJ should be less ( $\sim 1/2$ ) than for the Moog cold gas thruster (model 58x125A [19]) with a minimum impulse bit of 100  $\mu$ N-s, since the minimum impulse bit depends on the thrust (Moog:  $F_{\text{Thrust}} = 4.4$  mN) and the valve's maximum open/close response time.

If liquid or solid propellant is used, the weight and storage density of the propulsion system could be greatly reduced due to a reduction in the tank mass [4]. The

storage density of the propellant is important to minimize the volume required for propellant tanks. The integration complexity of the system is similar to FMMR [4], consisting of a propellant tank, drain/fill valve, filter assemblies, control valve, and the thruster itself. The RGEJ design can be developed using simple MEMS fabrication techniques and common materials, which results in low-cost batch fabrication. The efficiency of the RGEJ is low (10%), but higher than other electro-thermal thrusters using plasma-aided technology (e.g. MPT).

The working principle of the RGEJ has been tested and the device has shown promising results that indicate its potential for real-world applications as a micro-propulsion thruster for small satellites. Further investigation is needed to optimize and improve the thruster.

### **The Numerical Model**

Loosely coupling the finite element based rarefied gas module and the finite difference based ionized gas module in the MIG framework resulted in a stable approach to solve internal, slip flow problems with glow discharges. These type of problems are highly unstable since the plasma and gas interact strongly with each other, but their time scales are widely different by  $\mathcal{O}(10^{-5} \text{ s})$ . The approach used in this study circumnavigates this problem by increasing the voltage in small increments and by having several convergence criteria as explained in the introduction of [Chapter 5](#). Using finite difference to solve the ionized gas is faster than using finite volume for rectangular geometries. While using the finite element based rarefied gas module will allow the analysis of more complex geometries in the future. The MIG numerical platform is computationally cost-effective and it was able to solve each individual case

in a single processor under a period of a month using a mesh with 52801 nodes in the RGM to model the channel and the plume and a mesh with 12431 nodes in the IGM to model the channel.

### **Future Directions to Continue Improving RGEJ**

Argon was selected as the working fluid because it is the noble gas of choice for benchmarking plasma numerical codes due to the few reactions necessary to model the glow discharge at low pressure. However, thermal thruster developers prefer to use gases with a lower molecular weight and a higher gas constant. Our goal is to develop a phase-change thruster concept that uses liquid or solid propellant, instead of argon, to avoid heavy storage tank and valve leakage problems. The low minimum required operating pressure is selected by design to eventually develop this class of thruster. In future simulations, a different gas with better-suited properties for the RGEJ thruster should be used and the geometry of the thruster should be optimized.

A suitable chemistry model should be used to simulate the thruster using the new propellants, which inevitably will require a greater number of species equations. As part of the proposed future work, the parallelization of the ionized gas module would be a necessity in order to perform these new simulations. The numerical model could be improved by coupling a thermal analysis module with the existing rarefied and ionized gas modules; it could also be improved by building and testing a prototype of the thruster for validation purposes.

## LIST OF REFERENCES

- [1] P. Romero et al., "Optimal station keeping for geostationary satellites with electric propulsion systems under eclipse constraints," *Mathematics in Industry*, vol. 12, p. 260, 2008.
- [2] D. M. Goebel and I. Katz, *Fundamentals of Electric Propulsion: Ion and Hall Thrusters*, Hoboken, NJ: John Wiley & Sons, 2008.
- [3] D. J. Barnhart, T. Vladimirova and M. N. Sweeting, "Very-Small-Satellite Design for Distributed Space Missions," *Journal of Spacecrafts and Rockets*, vol. 44, no. 6, pp. 1294-1306, 2007.
- [4] M. M. Micci and A. D. Ketsdever, *Micropropulsion for Small Spacecraft*, Reston, VA: AIAA, 2000.
- [5] M. Leomanni, A. Garulli, A. Giannitrapani and F. Scortecci, "Propulsion options for very low Earth orbit microsattellites," *Acta Astronautica*, vol. 133, pp. 444-454, 2017.
- [6] W. Marshall and C. Boshuizen, "Planet Labs' remote sensing system," in *Proceedings of the 27th AIAA/USU Conference on Small Satellites*, Logan, U.S.A., 2013.
- [7] A. Ketsdever, A. Green, E. P. Muntz and S. Vargo, "Fabrication and Testing of the Free Molecule Micro-Reistojet: Initial Results," in *36th Joint Propulsion Conference & Exhibit*, Huntsville, AL, 2000.
- [8] Soni, "Characterization of Plasma Actuator Based Microthruster Concepts for High Altitude Aircrafts and Cubsats," University of Florida, Gainesville, FL, 2014.
- [9] S. Roy, "Method and Apparatus of Small Satellite Propulsion". US Patent US20120204618, 6 December 2012.
- [10] T. Deconinck, S. Mahadevan and L. L. Raja, "Computational simulation of coupled nonequilibrium discharge and compressible flow phenomena in a microplasma thruster," *Journal of Applied Physics*, vol. 106, p. 063305, 2009.
- [11] T. D. Deconinck, "Simulation Studies of Direct-Current Microdischarges for Electric Propulsion," Ph.D. Dissertation, Austin, Tx: The University of Texas at Austin, (2008).

- [12] A. Greig, C. Charles and R. Boswell, "Simulation of main plasma parameters of a cylindrical asymmetric capacitively coupled plasma micro-thruster using computational fluid dynamics," *Frontiers in Physics*, vol. 2, no. 80, pp. 1-9, 2015.
- [13] T. Takahashi, Y. Takao, K. Eriguchi and K. Ono, "Numerical and experimental study of microwave-excited microplasma and micronozzle flow for a microplasma thruster," *Physics of Plasmas*, vol. 16, no. 8, pp. 1-14, 2009.
- [14] C. Charles and R. Boswell, "Measurement and modelling of a radiofrequency micro-thruster," *Plasma Sources Science and Technology*, vol. 21, no. 2, pp. 1-4, 2012.
- [15] J. Mueller, R. Hofer and J. Ziemer, "Survey of propulsion technologies applicable to cubesats," in *57th JANNAF Propulsion Meeting*, Pasadena, CA, 2010.
- [16] J. Mueller, "Thruster Options for Microspacecraft: A Review and Evaluation of Existing Hardware and Emerging technologies.," in *Proceedings of the 33rd AIAA/ASME/SAE/ASEE Joint Propulsion Conference*, Seattle, WA, 1997.
- [17] S. W. Janson, H. Helvajian, W. W. Hansen and J. Lodmell, "Microthrusters for Nanosatellites," in *The Second International Conference on Integrated Micro Nanotechnology for Space Applications*, Pasadena, CA, 1999.
- [18] D. B. Scharfe and A. Ketsdever, "A Review of High Thrust, High Delta-V Options for Microsatellite Missions," in *45th AIAA Joint Propulsion Conference & Exhibit*, Denver, CO, 2009.
- [19] J. Mueller, J. K. Ziemer, R. R. Hofer, R. E. Wirz and T. O'Donnell, "A Survey of Micro-Thrust Propulsion Options for Microspacecraft and Formation Flying Missions," in *In: 5th Annual CubeSat Developers Workshop*, San Luis Obispo, CA, 2008.
- [20] J. M. Parker, D. Thunnissen, J. Blandino and G. Ganapathi, "The Preliminary Design and Status of a Hydrazine MilliNewton Thruster Development," in *35th AIAA/ASME/SAE/ASEE Joint Propulsion Conference*, Los Angeles, CA, 1999.
- [21] A. London, A. Epstein and J. Kerrebrock, "A High Pressure Bipropellant Micro-Rocket Engine," in *36th AIAA/ASME/SAE/ASEE Joint Propulsion Conference*, Huntsville, AL, 2000.
- [22] B. Marcu, G. Prueger, A. Epstein and S. Jacobson, "The Commoditization of Space Propulsion: Modular Propulsion Based on MEMS Technology," in *41st AIAA/ASME/SAE/ASEE Joint Propulsion Conference*, Tucson, AZ, 2005.

- [23] A. D. Ketsdever, R. H. Lee and T. C. Lilly, "Performance testing of a microfabricated propulsion system for nanosatellites applications," *Journal of Micromechanics and Microengineering*, vol. 15, no. 12, pp. 2254-2263, 2005.
- [24] R. Lee, A. Bauer, M. Killingsworth, T. Lilly, J. Duncan and A. Ketsdever, "Performance Characterization of a Free Molecule Micro-Resistojet Utilizing Water Propellant," in *43th AIAA/ASME/SAE/ASEE Joint Propulsion Conference*, Cincinnati, OH, 2007.
- [25] F. Rysanek, J. Hartmann, J. Schein and R. Binder, "MicroVacuum Arc Thruster Design for a CubeSat Class Satellite," in *16th Annual AIAA/ISU Conference on Small Satellites*, Logan, UT, 2002.
- [26] J. Schein, M. Krishnan, R. Shotwell and J. Ziemer, "Vacuum Arc Thruster for Optical Communications Missions," in *39th AIAA/ASME/SAE/ASEE Joint Propulsion Conference*, Huntsville, AL, 2003.
- [27] R. Burton, J. G. Eden, L. Raja, S. J. Park, J. Laystrom-Woodard and M. de Chadenedes, "Thrust and Efficiency Performance of the Microcavity Discharge Thruster," University of Illinois at Urbana-Champaign, Arlington, VA: Air Force Office of Scientific Research, 2011.
- [28] R. Wirz, M. Gale, J. Mueller and C. Marrese, "Miniature Ion Thrusters for Precision Formation Flying," in *40th AIAA/ASME/SAE/ASEE Joint Propulsion Conference & Exhibit*, Ft. Lauderdale, FL, 2004.
- [29] D. Feili, B. Lotz, S. Bonnet, B. Meyer, H. Loeb and H. Puetman, " $\mu$ NRIT-2.5 A New Optimized Microthruster of Giessen University," in *31st International Electric Propulsion Conference*, University of Michigan, MI, 2009.
- [30] V. Khayms and M. Martinez-Sanchez, "Fifty-Wall Hall Thruster for Microsatellites," in *Micropropulsion for Small Spacecraft (Progress in Astronautics and Aeronautics)*, vol. 187, Reston, VA, AIAA, 2000, p. Chap. 9.
- [31] K. Polzin, Y. Raites, J. Gayoso and N. Fisch, "Comparisons in Performance of Electromagnet and Permanent Magnet Cylindrical Hall Thrusters," in *46th AIAA/ASME/SAE/ASEE Joint Propulsion Conference & Exhibit*, Nashville, TN, 2010.
- [32] K. Polzin, T. Markusic, B. Stanojev, A. Dehoyos, Y. Raites, A. Smirnov and N. Fisch, "Performance of a Low-Power Cylindrical Hall Thruster," *Journal of Propulsion and Power*, vol. 23, no. 4, pp. 886-888, 2007.

- [33] A. Smirnov, Y. Raitses and N. Fisch, "Performance Studies of Miniaturized Cylindrical and Annular Hall Thrusters," in *38th AIAA/ASME/SAE/ASEE Joint Propulsion Conference*, Indianapolis, IN, 2002.
- [34] N. Demmons, V. Hruby, D. Spence, T. Roy, E. Ehrbar and J. Zwahlen, "ST7-DRS Mission Colloid Thruster Development," in *44th AIAA/ASME/SAE/ASEE Joint Propulsion Conference*, Hartford, CT, 2008.
- [35] V. e. a. Hruby, "ST7-DRS Colloid Thruster System Development and Performance Summary," in *44th AIAA/ASME/SAE/ASEE Joint Propulsion Conference*, Hartford, CT, 2008.
- [36] D. Simon, B. Land and J. Emhoff, "Experimental Evaluation fo a Micro Liquid Pulsed Plasma Thruster Concept," in *42nd AIAA/ASME/SAE/ASEE Joint Propulsion Conference & Exhibit*, Sacramento, CA, 2006.
- [37] F. F. Chen, *Introduction to Plasma Physics and Controlled Fusion*, Second Edition, New York: Plenum Press., 1984.
- [38] I. Langmuir, "Oscillations in Ionized Gases," *National Academy of Science*, vol. 14, no. 8, pp. 627-637, 1928.
- [39] M. Mitchner and C. H. Kruger, *Partially Ionized Gases*, New York: Wiley, 1973.
- [40] A. von Engel, *Ionized Gases*, Pittsford, NY: American Institute of Physics, 1997.
- [41] M. A. Lieberman and A. J. Lichtenberg, *Principles of Plasma Discharge and Materials Processing*, New York: John Wiley & Sons, 1994.
- [42] M. J. Druyvesteyn and F. M. Penning, "The mechanism of electrical discharges in gases of low pressure," *Reviews of Modern Physics*, vol. 12, no. 2, pp. 87-174, 1940.
- [43] Y. P. Raizer, *Gas Discharge Physics*, New York: Springer, 1991.
- [44] J. R. Roth, *Industrial Plasma Engineering, Volume 1: Principles*, Bristol, United Kingdom: Institute of Physics Publishing, 1995.
- [45] M. A. Laughton and D. D. Warne, *Electrical Engineer's Reference Book 16th ed.*, Oxford: Newnes, 2002.
- [46] A. Zumbilev, "Carbonitriding of Materials in Low Temperature Plasma," in *Heat Treatment -Conventional and Novel Applications*, InTech, 2012, p. 420.

- [47] R. K. Marcus, *Glow Discharge Spectroscopies*, New York: Plenum Press, 1993.
- [48] M. J. Madou, *Fundamentals of Microfabrication: the Science of Miniaturization*, 2nd Edition, New York: CRC Press, 2002.
- [49] H. Conrads and M. Schmidt, "Plasma generation and plasma sources," *Plasma Sources Science and Technology*, vol. 9, no. 4, p. 441, 2000.
- [50] A. A. Fridman, *Plasma Chemistry*, Cambridge University Press, 2008.
- [51] A. M. Howatson, *An Introduction to Gas Discharges*, 2nd edn., Oxford: Pergamon Press, 1976.
- [52] R. Mason and P. Melanie, "Sputtering in a glow discharge ion source - pressure dependence: theory and experiment," *Journal of Physics D: Applied Physics*, vol. 27, no. 11, pp. 2363-2371, 1994.
- [53] V. E. Golant, A. P. Zhilinsky and I. E. Sakharov, *Fundamentals of Plasma Physics*, New York: John Wiley & Sons, 1980.
- [54] T. Houba, "Parallel 3-D Numerical Simulation of Dielectric Barrier Discharge Plasma Actuators," University of Florida, Gainesville, FL, 2016.
- [55] A. Blanco and S. Roy, "Rarefied gas electro jet (RGEJ) micro-thruster for space propulsion," *Journal of Physics D: Applied Physics*, vol. 50, no. 455201, pp. 1-15, 2017.
- [56] N. Balcon, "Atmospheric pressure Radio Frequency discharges, diagnostic and numerical modeling," University of Toulouse, Toulouse, France, 2007.
- [57] G. J. M. Hagelaar and L. C. Pitchford, "Solving the Boltzmann equation to obtain electron transport coefficients and rate coefficients for fluid model," *Plasma Sources Science and Technology*, vol. 14, pp. 722-733, 2005.
- [58] J. C. Maxwell, "A dynamical theory of the electromagnetic field," *Philosophical Transactions of the Royal Society*, vol. 155, pp. 459-512, 1865.
- [59] E. A. Rafatov, D. Akbar and S. Bilikmen, "Physics Letters A," *Modelling of non-uniform DC driven glow discharge in argon gas*, vol. 367, pp. 114-119, 2007.
- [60] R. Kee, G. Dixon-Lewis, J. Warnatz, M. Coltrin and J. Miller, "A fortran computer code package for the evaluation of gas-phase multicomponent transport properties," Sandia, 1995.

- [61] G. M. Petrov and C. M. Ferreira, "Numerical modeling of the constriction of the dc positive column in rare gases," *Physical Review E*, vol. 59, no. 3, 1998.
- [62] S. F. Biagi, "Biagi-v7.1 (Magboltz version 7.1)," June 2004. [Online]. Available: [www.lxcat.net](http://www.lxcat.net). [Accessed 30 January 2015].
- [63] G. J. M. Hagelaar, F. J. de Hoog and G. M. W. Kroesen, "Boundary conditions in fluid models of gas discharges," *Physical Review E*, vol. 62, no. 1, pp. 1452-1454, 2000.
- [64] S. T. Surzhikov and J. S. Shang, "Two-component plasma model for two-dimensional glow discharge in magnetic field," *Journal of Computational Physics*, vol. 199, pp. 437-464, 2004.
- [65] D. J. Griffiths, *Introduction to Electrodynamics*, Third Edition, Upper Saddle River, NJ: Prentice Hall, 1999.
- [66] H. Sitaraman and L. L. Raja, "Simulation studies of RF excited micro-cavity discharge for micro-propulsion applications," *Journal of Physics D: Applied Physics*, vol. 45, no. 18, pp. 1-11, 2012.
- [67] J. P. Boeuf, L. C. Pitchford and K. H. Schoenbach, "Predicted properties of microhollow cathode discharges in xenon," *Applied Physics Letters*, vol. 86, no. 7, pp. 1-3, 2005.
- [68] R. Raju, "Hydrodynamic Model for Investigation of Gas Flows Through Micro-Geometries and Nanopores," M.S. Dissertation, Mechanical Engineer Dept., Flint, MI: Kettering University, (2003).
- [69] H. Hanley, "The Viscosity and Thermal Conductivity Coefficients of Dilute Argon, Krypton, and Xenon," *J. Phys. Chem. Ref. Data*, vol. 2, pp. 619-642, (1973).
- [70] R. J. Goldston and P. H. Rutherford, *Introduction to Plasma Physics*, Bristol and Philadelphia: Plasma Physics Lab., Princeton University, Intitute of Physics Publishing, (1995), p. 150.
- [71] A. R. Choudhuri, *The Physics of Fluids and Plasmas: an Introduction for Astrophysicists*, Cambridge, United Kingdom: Cambridge University, Cambridge University Press., (1998), p. 19.
- [72] J. C. Maxwell, "On Stresses in Rarefied Gases Arising from Inequalities of Temperature," *Philosophical Transactions of the Royal Society Part1*, vol. 170, pp. 231-256, (1879).

- [73] v. M. Smoluchowski, "Ueber wärmeleitung in verdünnten gasen," *Annalen der Physik und Chemi*, vol. 64, pp. 101-130, (1898).
- [74] A. Agrawal and S. V. Prabhu, "Survey on measurement of tangential momentum accommodation coefficient," *Journal of Vacuum Science and Technology A*, vol. 26, no. 4, pp. 634-645, 2008.
- [75] W. M. Trott et al., "Experimental Measurement of Thermal Accommodation Coefficients for Microscale Gas-Phase Heat Transfer," *AIAA*, no. 2007-4049, 2007.
- [76] M. F. Modest, *Radiative Heat Transfer 2nd Ed.*, Amsterdam: Academic Press, 1993.
- [77] F. P. Incropera, D. P. Dewitt, T. L. Bergman and A. S. Lavine, *Fundamentals of Heat and Mass Transfer 6th Ed.*, Hoboken, NJ: John Wiley & Sons, 2007.
- [78] D. Balagangadhar and S. Roy, "Design Sensitivity Analysis and Optimization of Steady Fluid-Thermal Systems," *Computer Methods in Applied Mechanics and Engineering*, vol. 190, pp. 5465-5479, (2001).
- [79] S. Roy, "Combining Galerkin Matrix Perturbation with Taylor Weak Statement Algorithms," *Computer Method in Applied Mechanics and Engineering*, vol. 184, pp. 87-98, (2000).
- [80] S. Roy and B. P. Pandey, "Development of a Finite Element-Based Hall-Thruster Model," *Journal of Propulsion and Power*, vol. 19, pp. 964-971, 2003.
- [81] S. Roy, R. Raju, H. Chuang, B. Cruden and M. Meyyappan, "Modeling gas flow through microchannels and nanopores," *Journal of Applied Physics*, vol. 93, pp. 4870-4879, (2003).
- [82] S. Roy and D. Gaintonde, "Force interaction of high pressure glow discharge with fluid flow for active separation control," *Physics of Plasmas*, vol. 13, no. 023503, 2006.
- [83] H. Kumar and S. Roy, "Multidimensional hydrodynamic plasma-wall model for collisional plasma discharges with and without magnetic field effects," *Physics of Plasmas*, vol. 12, no. 093508, 2005.
- [84] D. Scharfetter and H. Gummel, "Large-Signal Analysis of a Silicon Read Diode Oscillator," *IEEE Trans. Elec. Dev.*, vol. 16, pp. 64-77, (1969).

- [85] Y. Saad and H. S. Martin, "GMRES: A Generalized Minimal Residual Algorithm for Solving Nonsymmetric Linear Systems," *SIAM J. Sci. Stat. Comput.*, vol. 7, no. 3, pp. 856-869, 1986.
- [86] J. Oden and E. R. A. Oliveira, *Lectures on Finite Element Methods in Continuum Mechanics, (A Collection of Lectures)*, Huntsville: University of Alabama in Huntsville Press, 1976.
- [87] A. J. Baker, *Finite Element Computational Fluid Mechanics*, New York: Hemisphere Publishing Corporation, 1983.
- [88] C. Wang, *Numerical Modeling of Microscale Plasma Actuators*, Gainesville: University of Florida, 2009.
- [89] A. J. Baker and D. W. Pepper, *Finite Elements 1-2-3*, McGraw Hill, 1991.
- [90] J. Donea and A. Huerta, *Finite Element Methods for Flow Problems*, Chichester, England: John Wiley & Sons, 2003.
- [91] The MathWorks, Inc., *MATLAB*, Natick, Massachusetts, United States, 2017.
- [92] V. A. Godyak, R. B. Pijak and B. M. Alexandrovich, "Electrical Characteristics of Parallel-Plate RF Discharges in Argon," *IEEE Transactions on Plasma Science*, vol. 19, pp. 660-676, 1991.
- [93] A. J. Chorin, "A numerical method for solving incompressible viscous flow problems," *Journal of Computational Physics*, vol. 2, pp. 12-26, 1967.
- [94] C. S. Chen, S. M. Lee and J. D. Sheu, "Numerical Analysis of Gas flow in Microchannels," *Numerical Heat Transfer, Part A*, vol. 33, pp. 749-762, 1998.
- [95] K. C. Pong, C. Ho, J. Liu and Y. Tai, "Non Linear Pressure Distribution in Uniform Microchannels," *ASME-PUBLICATIONS-FED*, vol. 197, p. 51, 1994.
- [96] A. D. Ketsdever, M. T. Clabough, S. F. Gimelshein and A. A. Alexeenko, "Experimental and numerical determination of micropropulsion device efficiencies at low Reynolds number," *AIAA Journal*, vol. 43, no. 1, pp. 633-641, 2005.
- [97] G. E. Karniadakis, A. Beskok and N. Aluru, *Microflows and Nanoflows: Fundamentals and Simulation. Vol. 29*, Springer Science & Business Media, 2006.

- [98] H. Xue and Q. Fan, "A high order modification on the analytic solution of microchannel gaseous flows.," in *In: Proceeding of ASME fluids engineering division summer meeting*, Boston, USA, 2000.
- [99] W. M. Zhang, G. Meng and X. Wei, "A review on slip models for gas microflows," *Microfluids and nanofluidics*, vol. 13, no. 6, pp. 845-882, 2012.
- [100] J. Maurer, P. Tabeling, P. Joseph and H. Willaime, "Second-order slip laws in microchannels for helium and nitrogen," *Physics of Fluids*, vol. 15, no. 9, pp. 2613-2621, 2003.
- [101] T. Houba and S. Roy, "Numerical study of low pressure air plasma in an actuated channel," *Journal of Applied Physics*, vol. 118, no. 23, pp. 1-9, 2015.
- [102] S. Kang and H. Oh, "On-Orbit Thermal Design and Validation of 1 U Standardized CubeSat of STEP Cube Lab," *International Journal of Aerospace Engineering*, vol. 2016, pp. 1-17, 2016.
- [103] J. Henninger, "Solar Absorptance and Thermal Emittance of Some Common Spacecraft Thermal-Control Coatings," National Aeronautics and Space Administration, Washington DC, 1984.
- [104] T. Trudel, S. Bilen and M. Micci, "Design and Performance testing of a 1-cm Miniature Radio Frequency Ion Thruster," in *31st International Electric Propulsion Conference*, University of Michigan, MI, 2009.

## BIOGRAPHICAL SKETCH

Ariel Blanco conducted his undergraduate studies at the University of Florida, where he graduated with a dual Bachelor degree in mechanical and aerospace engineering in December 2008 with the honors of Cum Laude. After graduation, Ariel Blanco decided to continue his education at the same university. He obtained a Master of Science degree in Aerospace Engineering in May 2010. During the last semester of his Master of Science degree, after careful consideration, he realized that he wanted to study electric propulsion in order to contribute to America's pursuit of space exploration and joined the Applied Physics research group (APRG) under the tutelage of Dr. Subrata Roy and started his doctoral research in the field of micro-electric propulsion. He received his Doctor of Philosophy degree from the University of Florida in the fall of 2017.